END OF THE PROJECT REPORT

In-situ optical monitoring of gas turbine blade coatings under operational extreme environments: 31 December, 2022

Principal Investigator (PI): Professor Dr. Seetha Raghavan
seetha.raghavan@ucf.edu, +1 407 823 1737

Co-Principal Investigator (Co-PI): Associate Professor Dr. Ranajay Ghosh
ranajay.ghosh@ucf.edu, +1 407 823 3402

University of Central Florida, 4000 Central Florida Blvd, Orlando, FL 32816, USA

Submitted to: Department of Energy, National Energy Technology Laboratory

Award Number: DE-FE0031282

Topic Area: Topic 5: Advanced Instrumentation

Project Duration: 10/01/2017 – 09/30/2022

DUNS Number: 1508056530000

Reporting Period End Date: 12/31/2022

Submitted by:
Seetha Raghavan, PI
Phone: 407 823 1737
Email: seetha.raghavan@ucf.edu

Signature: 

Contents

1 ACCOMPLISHMENTS **2**

2 PRODUCTS **97**

3 PARTICIPANTS & OTHER COLLABORATING ORGANIZATIONS **101**

4 IMPACT **102**

5 CHANGES/PROBLEMS **103**

6 SPECIAL REPORTING REQUIREMENTS **104**

7 BUDGETARY INFORMATION **104**

8 PROJECT OUTCOMES: **104**

1 ACCOMPLISHMENTS

a. What were the major goals and objectives of this project?

Project Tasks:
The following table summarizes the overall project tasks and completion status.

Tasks	Milestone Description	FY18	FY19	FY20	FY21	FY22
Task 1						
Project Management	*Completion of all tasks*					complete
Task 2						
Defining and Manufacturing of the Sensor Configuration	*Coating configurations selected*	complete				
2.1 Identify and Select Materials		complete				
2.2 Perform Simulation		complete				
Task 3						
Establishing Sensing Properties Characterizing Coating Response Luminescence Sensing	*Testing of temperatire measurements complete*			complete		
3.1 Correlate Materials Measurement Properties				complete		
3.2 Simulation Surface Defects Temperature Properties				complete		
Task 4						
Non-intrusive and well benchmarked measurements surface temperature and coating strain	*Validation of benchmark tests complete*					complete
4.1 Improve Temperature Measurement Capability						complete
4.2 Improve Strain Measurement Capability						complete
Task 5						
Lab scale instrumentation development	*Lab scale tests complete*			complete		
Task 6 - extension to increase TRL and capabilities						
Instrumentation adaptation to engine rig	*Lab scale tests complete*					
6.1 Manufacturing and deposition of luminescent coatings in an engine test rig	*Run a successful engine test*				complete	
6.2 Design and adaptation of Phosphor Thermometry for engine test rig					complete	
6.3 Data collection synchronization and data postprocessing						complete

Task list with order of performance and completion.

b. What was accomplished under these goals?

Task 1: Project Management

The PI and co-PI managed and directed the project in accordance with the Project Management Plan to meet all technical, schedule and budget objectives and requirements. This included the technical supervision of all the tasks presented below.

Task 2: Defining and Manufacturing of the Sensor Configuration

Temperature measurement accuracy is a main concern for the optimization of engine efficiency in turbomachinary. In particular, the precise determination of the temperature in the high pressure turbine is crucial to adjust the equivalence fuel/oxidizer ratio to reach maximum efficiency. Currently, state-of-the-art TBCs are not being used to their highest potential because of uncertainties in temperature measurements at high-temperature [121, 123]. Safety margins as high as 200°C are used to accommodate the significant temperature error values [207], highlighting that a better monitoring of temperature would lead to greater efficiency, a more accurate lifetime prediction, as well as a mitigated degradation enabled by reliable and controlled temperature measurements [191, 213]. To give a perspective, a 1% efficiency increase can save $20M over the full lifespan of operation of a 400 - 500 MW combined cycle plant [195]. Turbine components are designed to operate for extended periods, for example, a standard land-based gas turbine systems have generally a 30 - 40 years lifetime and hot path components are expected to survive up to 100,000 hours or 3,000 starts [145]. Safe and reliable operation of engines, with reduced downtime, is facilitated by a more accurate control of temperature in extreme environments as it prevents from operating turbine blades in fast damaging conditions [221]. The determination of temperature, in particular at the top coat / bond coat interface is critical to better monitor the lifetime of the coatings.

Temperature measurement techniques for TBCs

Implementing an *in-situ* temperature measurement method in a high pressure turbine is often impractical due to high pressure and temperature conditions. Table 1 presents the existing techniques that can be used to measure temperature on TBCs. Rotating blades running at high velocity, defined gas flow patterns and high operating temperatures limit the applicability of thermocouples. This is without considering the meticulous labor required for the installation of thermocouple probes, attaching them at the surface of the turbine blades, creating defect points, or affecting the manufacturing process to integrate thermocouples below the top coat [247, 219].

Table 1: Existing temperature measurement techniques and associated features for in-situ turbine blade coating monitoring.

Method	**Measured location**	**Range of temperature**	**Limits of the method**
Thermocouples	Point measurement	-250 to 2300°C	Intrusiveness Disrupting the flow [69] Chemical instability [100] Labor intensive
Thermal paint	Surface	150 to 1350°C	Low resolution [139, 113] Low maximum temperatures [125]
Infrared imaging	Surface	-50 to 2000°C	Sensitivity to stray light [239, 174] Sensitivity to emissivity variations induced by temperature or surface contamination [93, 3]
Phosphor thermometry	Surface or sub-surface	-250 to 1700°C	Weak signal at high temperatures [34, 110, 109, 149]

Among other options for TBC temperature measurements: thermal paints and thermal history sensors. These techniques have been applied in turbine environments, but are limited to off-line measurements. To reveal temperature conditions, thermal paints use the thermochromism of pigments and thermal history sensors use the luminescence of sol-gel phosphor materials that evolves rapidly, after initial exposition of the as-fabricated material to high temperature, through recrystallization, phase transition, oxidation or diffusion processes [70, 177, 112]. These two techniques can record the peak temperatures of the TBC surface and potentially determine defect zones through hot spots. Finally, optical methods are non-invasive and can potentially capture data under limited access in the hot section of gas turbines. Infrared imaging stands out as one of the most prevalent technique for temperature measurements on TBCs. It is based on the collection of the thermal radiation, emitted by the materials in the infrared range. The ideal blackbody radiation can be predicted using Planck's law, which formula for spectral irradiance is given by Equation 1.

$$E_\lambda = \frac{8\pi hc^2}{\lambda^5} \frac{1}{e^{hc/\lambda kT} - 1} \tag{1}$$

where h is Planck's constant, c is the speed of light, λ is the wavelength, k is Boltzmann's constant, and T is the temperature.

In practice, materials have wavelength and temperature-dependent emissivities that need to be considered when using thermal radiation based methods. The biggest advantage of this technique is its capability to perform non-contact real-time area temperature measurements with easy integration, but where precision is limited by the presence of noise from background emission of light from the operation of the turbine engines and where accuracy is heavily susceptible to emissivity variation [3, 119, 22]. Significant effort has been invested recently in developing TBCs that contain temperature sensors to use phosphor thermometry, a well-known technique that enables non-contact real-time measurements on TBCs, using temperature-dependent luminescence emitted from phosphors that produce a robust and reproducible signal, with measurement capabilities that can overcome difficulties faced by infrared measurements methods [41]. This technique has shown great potential for enhanced TBC temperature monitoring on operating engines [6, 68, 164, 238, 5]. It has the advantage of being versatile and its capabilities are still being extended for TBC characterization, in particular with the development of new material configurations with improved luminescence properties [24, 234]. Phosphor thermometry allows for high accuracy of the temperature measurements with highly sensitive phosphors. One of the biggest advantages of phosphor thermometry over the other techniques is its capability to measure temperatures under the surface of the coatings [74, 176], and closer to the interface between the top coat and the bond coat, which is the key location for the determination of TBC lifetime [89].

This research project focused on the use of phosphor thermometry and on the development of novel temperature measurement material sensor configurations, instrumentation and methods, applied to TBCs. Phosphor thermometry is believed to be extremely promising for improved temperature measurement effectiveness in real operating conditions of turbine engines, and for further extension of temperature monitoring capabilities. Specifically, using the luminescence decay method to measure temperatures for sensor TBCs. The decay in the luminescence intensity typically follows an exponential decay model, given by $I(t) = I_0 e^{(-\tau/t)}$ (Figure 1(a)). When phosphors are excited with a pulse of light, the width of the pulse is preferably much shorter than the decay time of the luminescence. The time dependent intensity, $I(t)$, is measured following the excitation pulse, and the decay time,

τ, is calculated from the slope of a plot of $log\ I(t)$ vs t where $I(t)$ is the time dependent intensity measured and t is the time [91]. The decay time τ is sensitive to the temperature of phosphor. The decay in intensity then can be related to the temperature of the coating (Figure 1(b)). The slope of the intensity decay dictates the temperature sensitivity of the luminescence of the material used. For example, YSZ : Dy is the combination of host : dopant, respectively, used for the data shown in Figure 1(b). An initial calibration of the lifetime decay at various temperatures for any combination will enable the retrace of the temperature value.

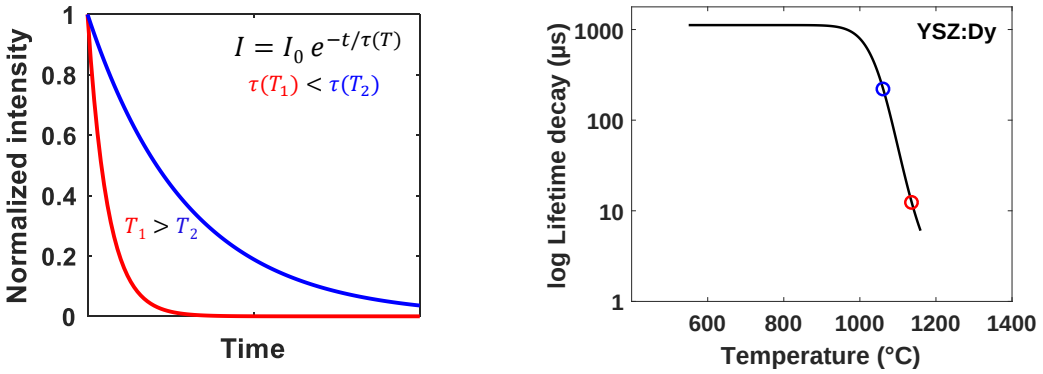

(a) (b)

Figure 1: Under pulsed laser excitation, (a) typical luminescence intensity with respect to time, (b) typical lifetime decay with respect to temperature [72].

Materials of interest for phosphor thermometry

Phosphor thermometry is a technique that utilizes temperature dependent luminescence properties of atoms that are excited with a pulse of laser. Various materials such as rare-earth or transition metals are capable of such usable luminescence. These elements can be used as dopants in a suitable host to leverage their luminescence property for noninvasive temperature measurements. The choice of the host in which these elements are doped (e.g. cation diffusion) strongly affects the luminescence as well as potentially their mechanical properties. Analyzing the properties of some promising doped configurations and developing predictive methods for optimal configuration selection were clear objectives in Task 2. The goal was to characterize and to obtain an improvement of the accuracy of the temperature dependent luminescence, leading to a possible reduced uncertainty and to investigate any effects on the mechanical properties of a selected configuration. The selection process for the materials to be used accounted for the relevant parameters that influence luminescent efficiency. The effect of the dopant on the overall mechanical and thermal properties of the configuration was also considered.

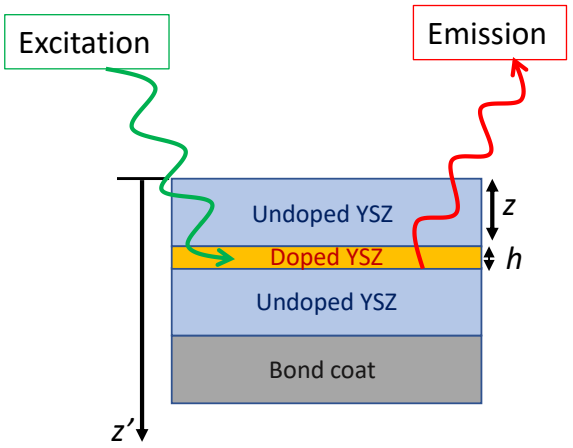

Figure 2: Configuration of TBC including a doped layer for phosphor thermometry

The schematic of a configuration of a TBC with an embedded doped layer is presented in Figure 2. The doped layer consists of host and rare-earth dopant material. It has two geometrical parameters to uniquely design the configuration for the purpose of interest, namely, the position of the doped layer, z and the thickness of the doped layer, h. The dopant concentration c can also be varied in order to obtain different sensing capabilities. z' represents the depth axis in the thickness direction, where $z' = 0$ represents the surface of the coating. A large number of rare-earth doped material configurations were considered as potential sensors for phosphor thermometry applied to TBCs. Europium and Dysprosium stand out for their intense luminescence that is conserved at high temperatures. The concentration of dopant is generally lower than 3 wt.% to enable high luminescence and avoid any phase change and conserve the thermomechanical or optical properties of the undoped material. The main material configurations (rare-earth dopant + host is noted Host:RE) that were tested previously in literature for TBC applications are presented below.

Rare-earth doped Yttrium aluminum garnet ($Y_3Al_5O_{12}$:RE)

Yttrium Aluminum garnet, also referred as YAG: This matrix has the advantage of possessing a very low oxygen diffusivity (10^{-25} m^2/s for bulk YAG), a low thermal conductivity at high temperature (3.2 W/m·K at 1000°C) [217] and a good phase stability up to its melting point (1970°C) [87]. However, the limited thermodynamic compatibility with the other phases present in standard TBCs [88] and its low coefficient of thermal expansion (6 - 8·10^{-6} /°C) [173, 187], combined with a low fracture toughness ($\approx$ 1.8 MPa·$\sqrt{m}$) [87] reduces its application scope in TBCs. In terms of luminescence properties, when used in combination with rare-earth dopants, it exhibits excellent high temperature measurement capabilities, up to at least 1400°C [209, 151]. YAG:Dy has been extensively used, including in turbine environments [213, 69, 122, 65, 108, 102, 56], YAG:Eu has similarly shown high temperature capabilities [183, 50, 71]. YAG:Tm has been studied as it provides ultraviolet luminescence that is advantageous in presence of thermal radiation [56] and its quenching temperature is as high as 1100°C which makes it suitable for TBC surface applications [122, 120].

Rare-earth doped Yttrium oxide (Y_2O_3:RE)

Yttrium oxide has been mainly combined with europium (Y_2O_3:Eu). Although it is known to display intense luminescence that is appropriate for Phosphor Thermometry on sensing TBCs [69, 6, 164, 122, 65, 183, 128], in particular for buried layers, this configuration is not ideal for real engine conditions as its luminescence signal is too low at temperatures exceeding 900°C, due to oxygen quenching [125]. Additionally, high pressure environments annihilates luminescence of Y_2O_3:Eu [23].

Rare-earth doped yttria stabilized zirconia (YSZ:RE)

The utilization of YSZ as the host material for rare-earth luminescence dopants is an attractive option for embedded sensing layers because of the layer compatibility with the rest of the TBC system which allows for reduced intrusiveness of the sensor. Rare-earth doped YSZ configurations for sensing TBCs have been thoroughly investigated [202, 32] due to its easy integration and suitability to high temperature luminescence applications. YSZ:Eu has been largely studied because of its intense luminescence that can be used for integration of a sensing layer in the depth of the TBC, and because it exhibits high sensitivity to temperature from 500 to 850°C [242, 213, 69, 71, 203, 10, 67]. YSZ:Dy has been also considered as it displays the highest temperature capability among rare-earth doped YSZ (about 1000°C), using the lifetime decay method [242, 213, 93, 209, 71, 33]. Other rare-earth dopants have been tested in a YSZ host for TBC applications using Phosphor Thermometry, namely, YSZ:Sm [179, 204], YSZ:Gd [213] and YSZ:Er [202, 204]. It can be noted that YSZ:Tb was found to be unusable due to the rapid oxidation of Tb [31]. Another attractive feature concerning YSZ:Eu and YSZ:Dy is that both phosphors possess a sensitivity that remains unchanged after thermal aging or at different dopant concentrations [43].

Manufacturing of TBC coupons by air plasma spray coating technique
Initial work for the manufacturing of sensor TBCs was performed in Task 2, early in the project, at the Florida Institute of Technology and includes three different configurations of rare-earth doped YSZ TBC coupons that were prepared using air plasma spray (APS). These configurations are shown in Figure 3.

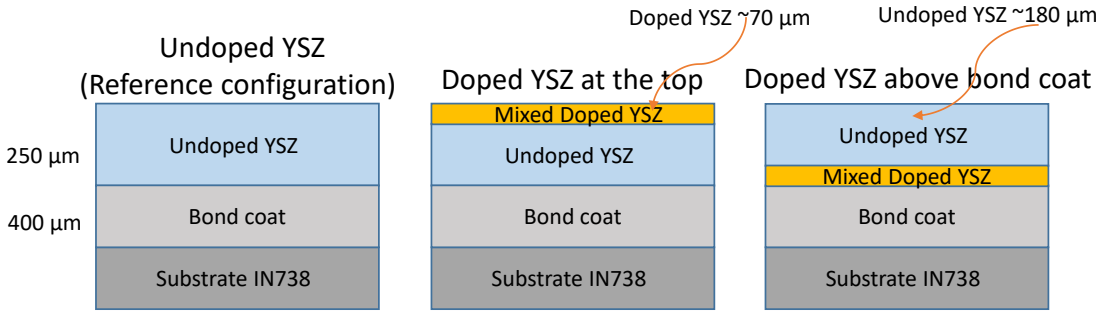

Figure 3: Schematic of the first coating configurations of TBC coupons prepared by APS.

Top coat starting powders used to manufacture this first set of samples include standard YSZ powder (ZRO-271, Praxair Surface Technologies) and YSZ:Eu 3 wt.% (Phosphor Technology Ltd.). The deposition of the doped YSZ powders turned out to be challenging due to the small particle size ($D_{50} < 1$ μm). Nanoparticles are usually preferred for the production of homogeneous doped powders, in a reasonable time scale, through cation diffusion during the solid state reaction. However, this particle size is problematic for air plasma spray deposition because standard deposition parameters are optimized for $D_{50} \approx$

30 - 50 μm. In addition, the doped powders were found to possess irregular particle shapes, which is an additional constraint for APS deposition. To ensure the flowability of the mixture and a good deposition rate for the doped layers, doped nanoparticle powder and undoped microparticle powder were mixed so the high flowability industrial powder can act as a carrier for the doped material. The micrographs of both starting powders and the resulting mixture that was used for the deposition of luminescent layers are presented in Figure 4. The particle size obtained for mixture was estimated to be approximately: $D_{50} \approx 30$ μm, using the microscope scaling tool. The powders were observed with a voltage acceleration of 15 kV.

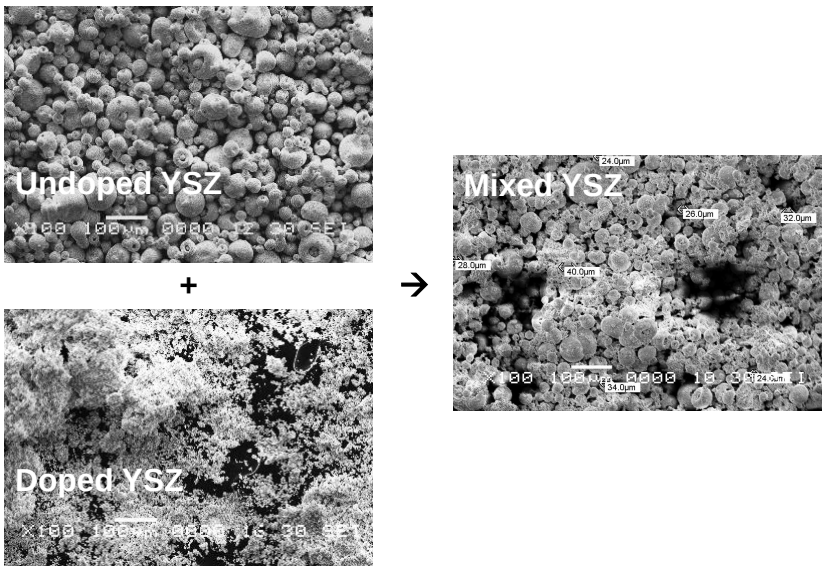

Figure 4: Micrographs of preprocessing powders mixed to enable the deposition of luminescent powders through air plasma spray.

During the deposition process, the feeding wheel speed was decreased to get a low but consistent deposition rate which drastically reduced the clogging probability of the APS system. The parameters used for the deposition of the layered configuration are given in Table 16. The rare-earth dopant concentrations in YSZ were chosen for optimal luminescence intensity, based on literature [88, 43, 178] and using the Johnson-Williams equation which results are presented in Figure 13.

Table 2: Parameters used for sample fabrication through air plasma spray.

	Bond coats	**Undoped top coats**	**Doped top coats**
Spray distance (cm)	10	7.5	7.5
Current (A)	802	902	902
Voltage (V)	43.3	43.7	43.7
Argon (SLM)	49.1	25.5	25.5
Helium (SLM)	20.3	20.8	20.8
Feeding wheel speed (rpm)	1.17	3.29	0.48

After the deposition of each layer, thickness measurements were performed using an eddy

current thickness gauge. The thicknesses are indicated in the sample matrix, given previously in Figure 29. Following the deposition of the TBCs on the superalloy disks, the studs that were used to mount the substrates on the APS deposition stage were removed and the specimens were cut into three pieces to provide:

- A circular segment for phosphor thermometry experiments
- A circular segment for scanning electron microscopy (SEM) characterization
- A 2.5 mm width rectangular cuboid piece for transmission X-ray diffraction experiments: this width was chosen as it is suitable for depth-resolved high-energy transmission X-ray diffraction measurements [232, 222].

The TBC coupons were then observed using SEM to determine more accurately the thicknesses of the layers. The SEM images of three TBC coupons are shown in Figure 5. The average thickness of the bond coats in TBC coupons was measured to be approximately 317 $\pm$ 29 μm. The total top coat thicknesses in the coupons were measured as 330 $\pm$ 22 μm, 247 $\pm$ 18 μm, and 346 $\pm$ 25 μm in the regular, doped layer at bottom, and doped layer at top configurations, respectively. In the TBCs with doped layers, the doped layer thicknesses were measured to be approximately 75 $\pm$ 11 μm. It can be noted from the SEM images that a mechanical interface can be observed in the configuration with the doped layer deposited at the top (named T in the caption). This is because there was a significant amount of delay in spraying the doped layer at the top, after spraying the standard YSZ layer. However, in the other configurations, no interface is observed under SEM.

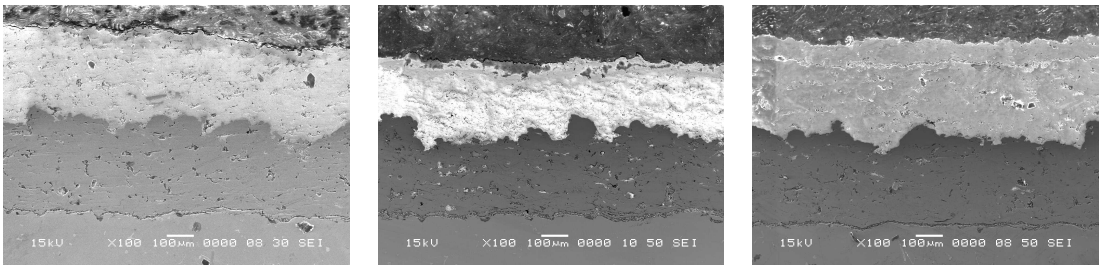

(a) Regular TBC (R) (b) Doped layer at bond coat (B) (c) Doped layer at top surface (T)

Figure 5: SEM micrograph of the TBCs of configurations (a) regular TBC, (b) Eu-doped layer at the bond coat, and (c) Eu-doped layer at the top.

This initial APS manufacturing work was improved and optimized throughout the project. Importantly, the main challenge preventing us from depositing rare-earth doped YSZ powder in this Task 2 was finally resolved using fumed silica in addition to pure rare-earth doped YSZ powder. This was done instead of using a mixture of rare-earth doped YSZ powder and standard sprayable powder. The fumed silica (CAB-O-SIL, Cabot) is a fluidizing agent that helped carry the powders through the powder feeder and which was vaporized in the plasma plume.

Task 3: Establishing Sensing Properties Characterizing Coating Response Luminescence Sensing

For this Task 3, multiple models were developed to both identify and optimize TBC configurations for improved sensing and to ensure suitable thermomechanical performance.

The typical material properties of industrial TBCs are presented in Table 3. The deposition method used for the top layer affects the resulting properties and therefore the performance of the coatings.

Table 3: Thermomechanical properties of standard materials composing TBCs.

	Top coat		**TGO**	**Bond coat**
Typical composition	*7-8wt.% YSZ (APS)*	*7-8wt.% YSZ (EB-PVD)*	Al_2O_3	*NiCrAlY*
Thermal conductivity λ at 1100°C (W/(m·K))	1-2 [48, 137, 143]	2-3 [167]	5-6 [137, 214]	34 [143]
Coefficient of thermal expansion α ($\times 10^{-6}$ K^{-1})	11-13 [137, 184, 243]	11-13 [146]	7-10 [146, 184]	13-16 [146, 184]
Elastic modulus E (GPa)	10-50 [180]	0-100	320-434 [25, 146, 184]	110-240 [25, 146, 184]
Toughness K (MPa·$\sqrt{m}$)	0.7-2.2 [184, 148]		2.8-3.2 [184, 173]	>20 [184]
Poisson's ratio ν	0.2 [243]		0.2-0.25 [25, 243]	0.3-0.33 [25, 243]
Oxygen diffusivity at 1000°C (m^2/s)	10^{-11} [137]		10^{-20} [137, 214]	-
Crystal microstructure Phase stable up to (°C)	t' 1200-1250 [167]		α 1750	β, γ 1050

It can be highlighted in Table 3 that the rapid formation of the TGO creates an additional protection against oxidation of the bond coat. However, further oxide growth eventually leads to the progressive degradation of TBCs as a result of the accumulation of strains due to expansion mismatch with the surrounding materials, particularly during thermal cycling. On the other hand, constant interactions between the layers control the durability of TBCs.

Modeling mechanics of the Thermally Grown Oxide (TGO) using Koch fractal

There have been many attempts to model the thermally grown oxide (TGO) utilizing various finite element analysis (FEA) [80, 192, 21]. The current consensus among the majority of papers studying TGO using FEA, seem to prefer a sine wave to model the interface of the TGO between the top coat and bond coat. After aging for a certain amount of time, a TGO does appear to be well represented by the sine wave interface. In the early stages of TGO growth, especially for TBCs applied through air plasma spray,the sine wave interface does not appear to be the best possible representation. This can be seen below in Figure 6. Using the sine wave we can vary the amplitude and frequency, which has given great insight into the TGO interface. Fractals are often used to describe surface roughness in mathematical terms. In particular, Koch fractal has been widely used to model fracture surfaces and interfaces [236, 147]. We utilized the Koch fractal to describe TGO interfaces. The Koch fractal closely mimics the interface of TGO to both bond coat and top coat.

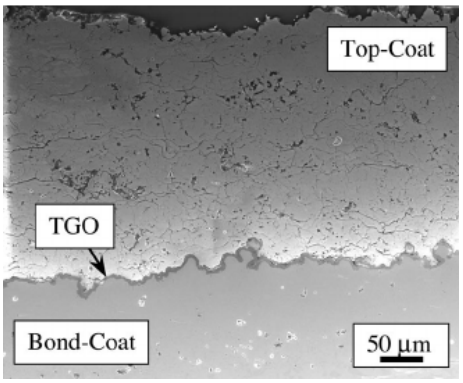

Figure 6: SEM image detailing the interfaces of top coat, TGO, and bond coat.

For the model that we developed, the geometry of the bond coat, top coat and TGO is shown in Figure 7 for different orders of the Koch fractal. The simulations were performed using the FE software Abaqus. The FE model was meshed with 4 noded linear plane strain elements (CPE4R). The FE mesh of a model of a 1st order Koch fractal is shown in Figure 8. The interfaces between bond coat and TGO, and top coat and TGO were defined using a surface-based cohesive zone model.

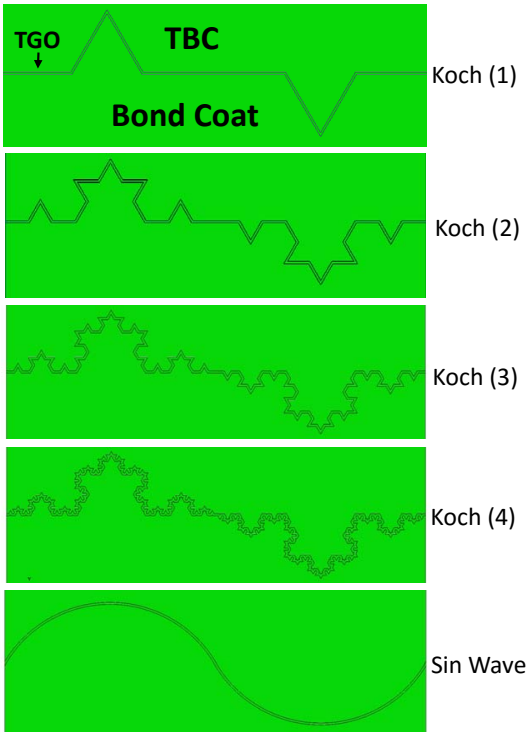

Figure 7: Geometries for TGOs modeled by Koch fractals of different order with TGO thickness of 1 µm [229].

Initial simulations were performed using linear elastic properties of bond coat, top coat and TGO (Table 4). The interface properties used in the bilinear cohesive zone model. The schematic of the traction separation law for the cohesive zone model is shown in Figure 9 for pure normal and shear modes. $K_{n,s}$ are initial stiffness of the interface under pure normal and shear modes. $(t_n,\ \delta_n)$ and $(t_s,\ \delta_s)$ are normal and shear traction (t) and separation (δ) at a point on interface, respectively. The damage initiation occurs when the

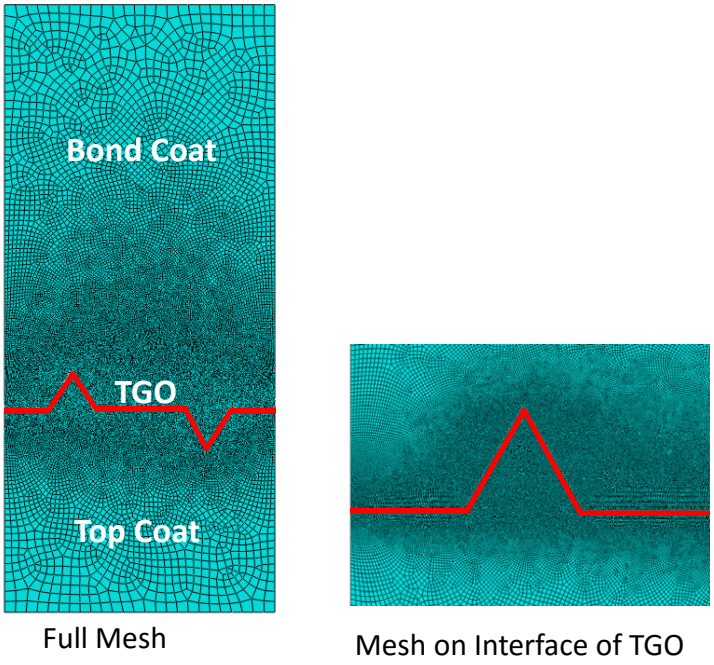

Figure 8: Finite element mesh of a TBC model with TGO described by Koch fractal.

traction reaches a critical value. The criterion for damage initiation under mixed mode loading is given by [27, 2]:

$$\left(\frac{\langle t_n \rangle}{t_n^0}\right)^2 + \left(\frac{t_s}{t_s^0}\right)^2 = 1 \tag{2}$$

where, t_n^0 and t_s^0 are the interface strengths under pure normal and shear modes, respectively. Following initiation, damage continues to grow until fracture, which is described in terms of fracture energies, given by:

$$\frac{G_n}{G_n^c} + \frac{G_s}{G_s^c} = 1 \tag{3}$$

where, G_n^c and G_s^c are fracture energy of the interface under pure normal and shear modes. The values of the model parameters are listed in Table 5. Both the interfaces, bond coat - TGO and TGO - top coat are assumed to have similar properties.

Materials	Young's modulus (E, GPa)	Poisson number (ν)
Bond coat	200	0.30
Top coat	48	0.10
TGO	400	0.23

Table 4: Properties of bond coat, TGO and top coat [193]

K_n (GPa/μm)	K_s (GPa/μm)	t_n^0 (MPa)	t_s^0 (MPa)	G_n^c (J/m^2)	G_s^c (J/m^2)
10	10	15	10	20	30

Table 5: Interface properties using cohesive zone model [2]

Initial simulations were performed to elucidate the load transfer and stress concentration around the TGO and interfaces. In these simulations the bottom surface of the model was

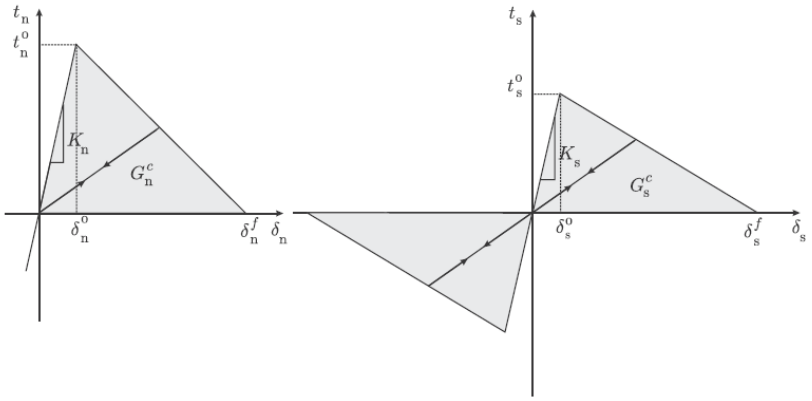

Figure 9: Schematic of bilinear traction separation laws under pure normal and shear modes for the cohesive zone model of interfaces [2].

fixed to prevent vertical displacement and a displacement equivalent to 5 % global strain was applied at the top surface. The resulting von Mises stress fields are shown in Figure 10. The normal stress in vertical direction in shown in Figure 11 and shear stresses in Figure 12 are obtained from FE models with Koch fractal of different orders.

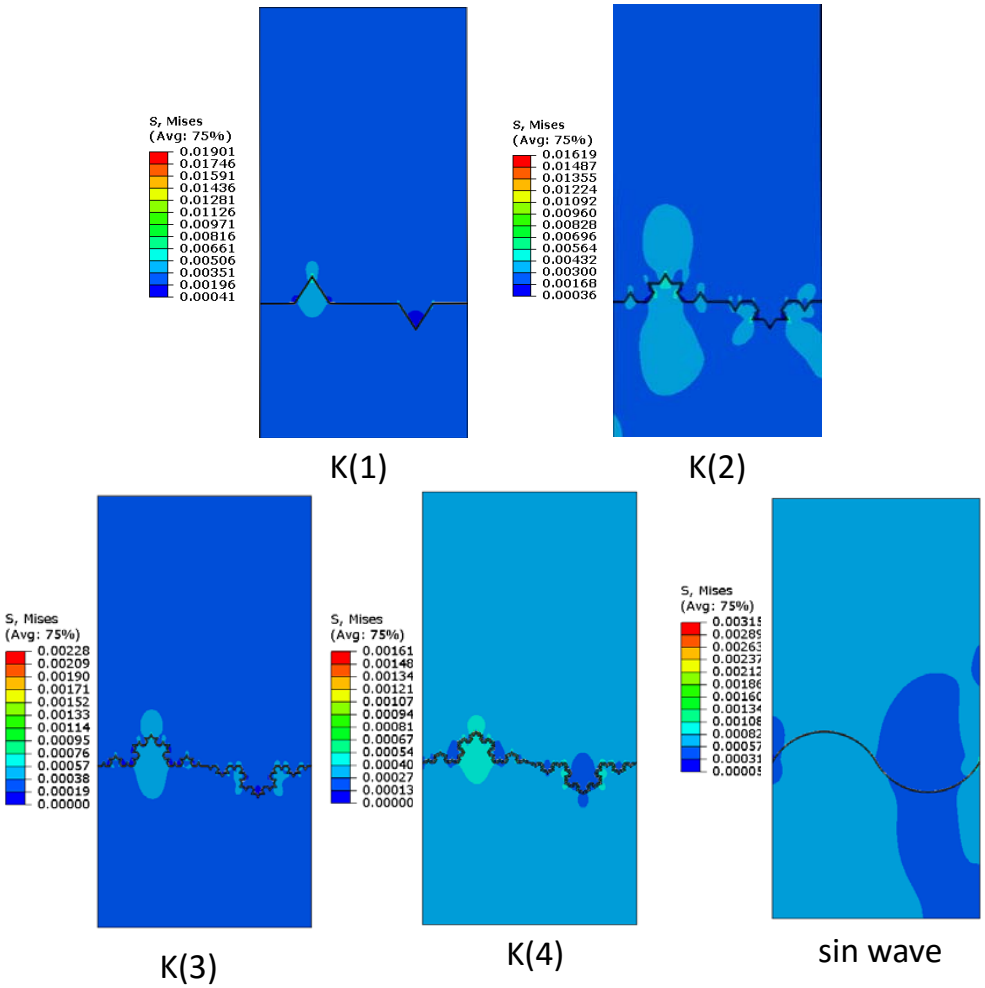

Figure 10: Von Mises stress in vertical direction of the TBC model with TGO described by different Koch fractals.

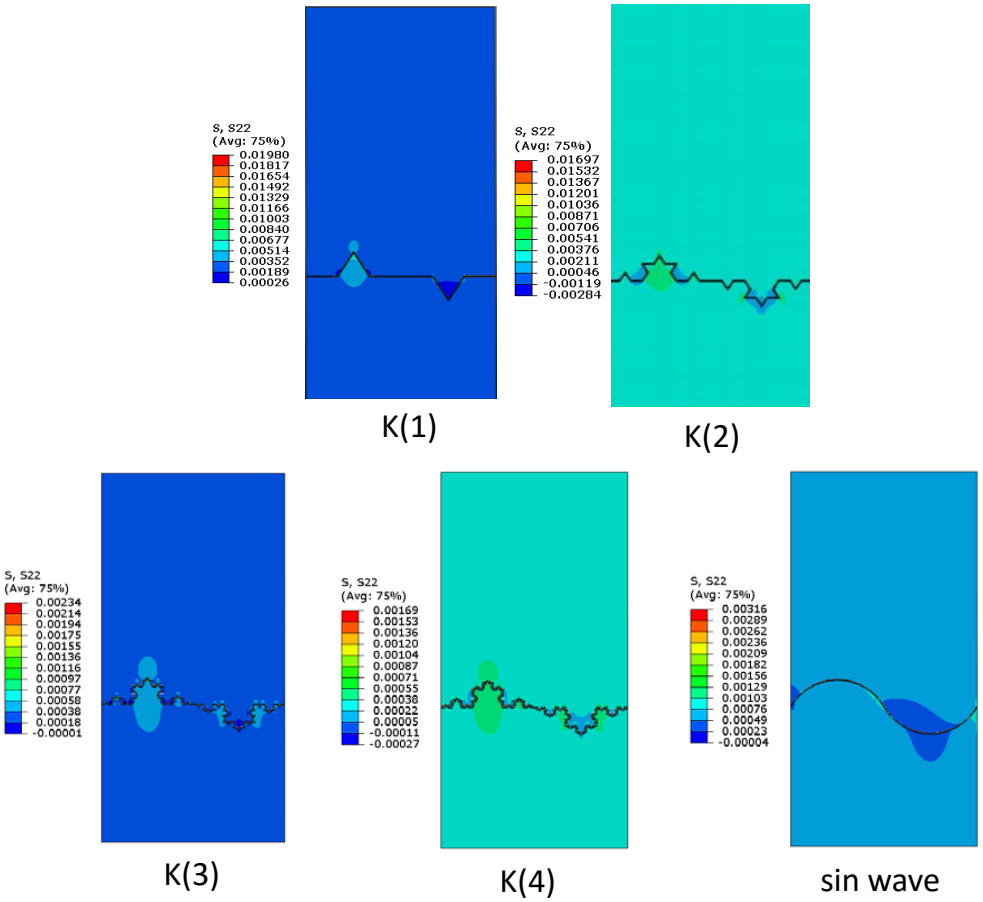

Figure 11: Normal stress in vertical direction of the TBC model with TGO described by different Koch fractals.

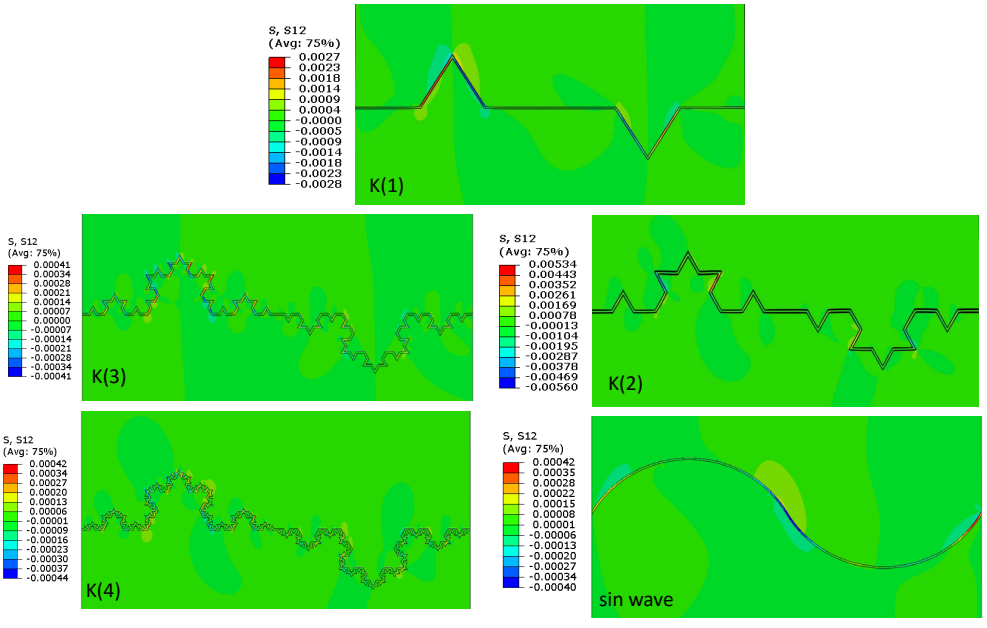

Figure 12: Shear stress in the TBC model with TGO described by different Koch fractals.

The results show that the magnitude of the maximum von Mises and normal stresses decrease in the models with increasing order of the Koch fractal [229]. Within a given model, increase in stress near the vertices of the fractal is observed resulting in a stress concentration. This could give insight into the effectiveness of a smooth versus rough interface between bond coat to top coat on the stress distribution throughout the thermal barrier coating. The results here are only for a thickness of the TGO of 1 μm.

After collecting these outcomes on stress interface generated at the TGO interfaces in TBCs, we focused more specifically on the development of models that account for sensor TBCs with multi-layers. These models are presented below.

Effect of rare-earth dopant concentration on output luminescence intensity

The luminescence intensity that can be produced by a luminescent material is largely dependent on the concentration of luminescent ions, called activator ions. As the concentration increases, if the activator ions are well dispersed into the ceramic host, for a determined area, a higher number of photons can be emitted. However, at higher concentrations or if the doping ions agglomerate, their interaction will cause vibrational deexcitation resulting in the lower probability of photons emission. This phenomenon is called concentration quenching. Some of the synthesis methods used for the production of luminescent materials for phosphor thermometry such as solid state reaction are likely to form dopant clusters. Agglomeration can result in both a reduced maximum concentration level to achieve optimal luminescence intensity as well as a fast decay component when measuring the time response of the luminescent material under a pulsed excitation. It is important to note that impurities (hydroxy group, organic compounds) that can be present in the luminescent coatings contribute highly to luminescence quenching. To overcome this issue, luminescent samples can be annealed at temperatures exceeding 800°C for at least 2 h to enhance luminescence [123, 125, 165].

The Johnson-Williams equation, presented in Equation 4, gives a good approximation of the effect of dopant concentration on the intensity of luminescence, assuming homogeneous distribution of activator ions in the host matrix [115, 116]. The maximum concentration of doping ions, for a particular combination of dopant and ceramic host, depends on the actual energy levels of the activator ion in the specific host [88]. The Johnson-Williams equation is defined as following:

$$I_c = \frac{c(1-c)^z}{c + \frac{\sigma}{\sigma'}(1-c)} \tag{4}$$

where c is the dopant concentration, z is the number of nearest dopant cation neighbors and $\frac{\sigma}{\sigma'}$ is the capture cross section of non-activators, accounting for the actual absorption cross-section of luminescent receptors in the material.

Figure 13 shows the results obtained by digitizing experimental results that demonstrate the effects of concentration on luminescence intensity, found in literature, to obtain the fitting parameters for the Johnson-Williams equation [88, 43, 90, 244]. It can be noted that the optimal concentration for maximum luminescence intensity is strongly dependent on the dopant used into a YSZ matrix.

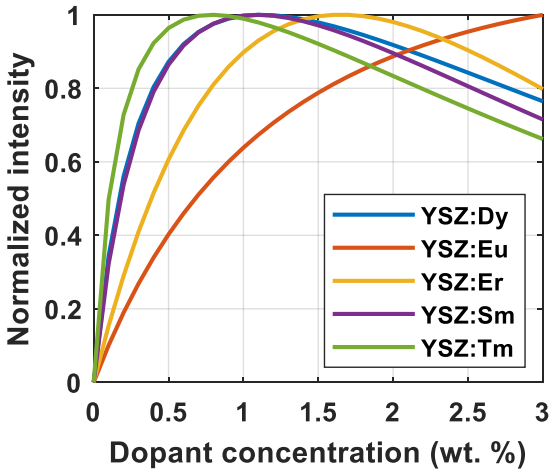

Figure 13: Predicted dependency of luminescence intensity in function of dopant concentration, and limited due to concentration quenching [72].

Rare-earth doped layer stability in ceramic coatings

The adaptation of phosphor thermometry to TBCs requires the manufacturing of embedded sensing layer configurations. One difficulty to consider in real conditions is the existing thermal gradient which can lead to significant measurement errors. A proposed solution is the application of a thin sensing layer, which minimizes the thermal gradient through the doped layer. However, the signal intensity is reduced proportionately. As a consequence, the thickness of the sensing layer needs to be adjusted to get a trade-off between temperature gradient and signal intensity. In this work, an intent to overcome this particular issue is discussed, later in the following chapters, where the exact location at which temperature measurement is performed could be estimated, through simulations, for any doped layer thickness, and in presence of a thermal gradient. Such claim promotes thick doped layer configurations as they obviously provide higher luminescence intensities.

Designing multilayer TBC configurations for precision temperature measurements using phosphor thermometry is only possible if the location of the sensing layer is known. Therefore, it is essential to determine up front if discrete rare-earth doped layers remain in place when embedded into a TBC configuration, to enable luminescence sensing. The possible diffusion of luminescent ions has been modeled in YSZ to evaluate the stability of the position of dopants when embedded in a TBC as a thin layer in a multilayered configuration. The simulation uses the 2^{nd} Fick's law for diffusion, presented in Equation 5.

$$\frac{\partial c_{RE}}{\partial t} = D_{RE}\frac{\partial^2 c_{RE}}{\partial x^2} \tag{5}$$

where c_{RE} is the normalized dopant concentration, $D_{RE} = 5.2 \cdot 10^{-8} \mu m^2/s$ is the grain boundary diffusivity of rare-earth ions in YSZ, x is the position into the coating, originating at the top surface and t is the time of operation of the TBC at 1200°C. The initial condition is defined in Equation 6 and the boundary condition assuming no external dopant source is defined in Equation 7.

$$c_{RE}(50 \leq x \leq 100) = 1 \tag{6}$$

$$\frac{\partial c_{RE}}{\partial t}(0, t) = 0 \tag{7}$$

The grain boundary diffusion was calculated using the diffusivity of Gadolinium (Gd) in cubic 8 mol.% YSZ at 1200°C in a Physical Vapor Deposition coating [19]. The grain boundary diffusion corresponds to a faster diffusion mode than bulk diffusivity and has been considered solely for this study to determine if the rare-earth diffusion in YSZ is negligible, and thus if multilayer configurations including discrete luminescent layers are viable. It is assumed that the diffusivity of other rare-earth elements remains identical to that of Gd and that the higher concentration of stabilizer, existing in the reference that was chosen in literature (Yttrium or rare-earth ions in zirconia), and leading to the prominence of the cubic phase, does not affect diffusion in YSZ. The bulk diffusivity of YSZ can be compared and supported by the value of cation diffusivity in standard 7-8 wt.% tetragonal YSZ found in literature [95].

The model configuration used for this simulation includes a 50 μm-thick layer of rare-earth doped YSZ, buried at 50 μm from the top surface into an undoped YSZ top coat. Figure 14 shows the results for the diffusion over the standard lifetime of a turbine blade TBC, indicating that the grain boundary diffusion penetration of dopant rare-earth ions throughout the surrounding ceramic top coat is negligible. As a consequence, it is possible to fabricate multilayer configurations including thin luminescent layers that remain in place over time.

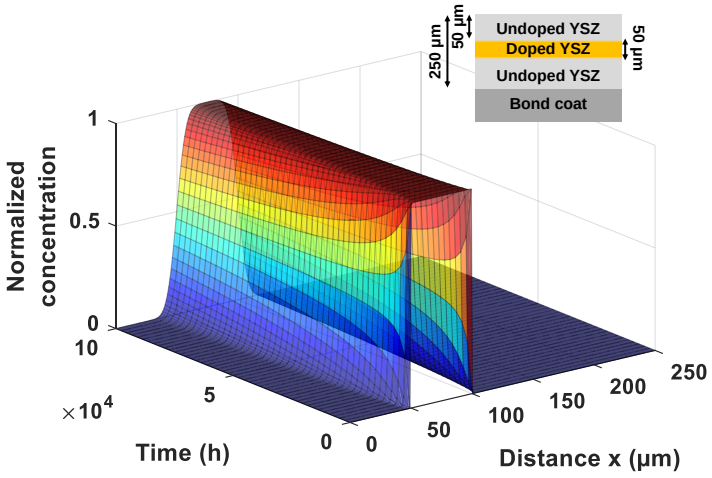

Figure 14: Predicted diffusion of rare-earth dopant through YSZ at 1200° C [72].

Luminescence intensity in rare-earth doped YSZ coatings

The challenge with modeling light propagation in TBCs, in order to understand its implications in phosphor thermometry, is to account for the significant amount of scattering that occurs in porous ceramic coatings. In addition, it is necessary to consider light absorption, as it travels through the coating. A model to account for this type of attenuation is the Kubelka-Munk model [132, 133]. This model is a 1D model that assumes isotropic

scattering of light and can model the distribution of light intensity in complex media. This model has been further extended for specific applications [196, 163, 162], and it has been applied in various fields including paint and papers [160], colorants and interference pigment mixtures [131], light trapping in plants and biological tissues [201, 245], and blood stain detection [114]. The model has been later implemented to describe excitation and emission intensity distributions within TBCs [176, 66].

Here, the light propagation behavior of the phosphor luminescence in TBC configurations was studied. To this goal, a 2×2-flux Kubelka-Munk model was constructed to predict the intensity of the luminescence at any point in the sensor coatings. The two TBC configurations considered in this study are the configuration **(C1)**, that contains a fully doped top coating, and the configuration **(C2)**, that contains an embedded doped layer in the top coat, as shown in Figure 15. The TBC configuration with an embedded doped layer has two geometrical parameters to uniquely describe the configuration for the purpose of interest, namely, the position of the doped layer and the thickness of the doped layer. In the modeling work achieved here, the total thickness of the top coat is maintained constant at 250 μm and the position is defined as the distance from the top surface of the TBC to the top surface of the doped layer. Three rare-earth doped materials, YSZ:Dy, YSZ:Er and YSZ:Sm were considered for this study. A detailed parametric study was performed by systematically varying the position and thickness of the doped layer.

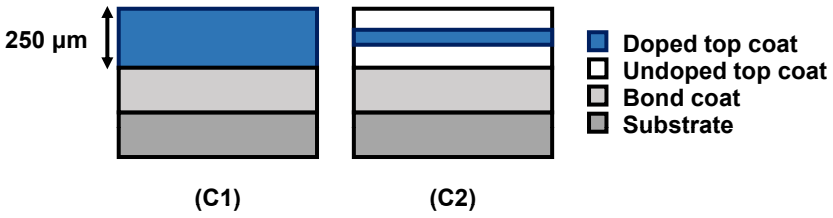

*Figure 15: Configurations of TBC including a doped layer for phosphor thermometry, (left) fully doped configuration **(C1)** and (right) embedded doped layer in the top coat **(C2)**.*

For a given excitation intensity input to the top surface of the TBC, the intensity of the emerging luminescence arising from the phosphorescent TBC depends on the absorption and scattering of the light into the coating. Therefore, the design of the TBC configuration strongly affects the intensity of the collectable signal. Figure 16 shows a schematic of the traveling incident laser light, and emitted luminescence in an example configuration that contains a doped layer inside the YSZ top coat. The position (x_1) of the top surface of the embedded doped layer of thickness $t = x_2 - x_1$ is measured from the TBC surface.

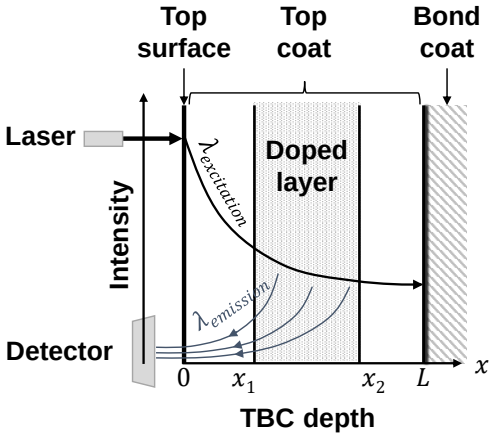

Figure 16: Mechanism of absorption of excitation (incident laser) and emission (luminescence) lights through the TBC.

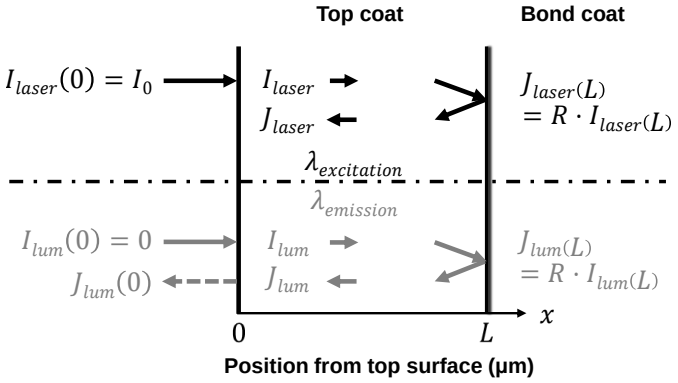

Figure 17: 1D 2×2-flux Kubelka-Munk boundary conditions to model phosphor luminescence in TBCs.

The classical two-flux Kubelka-Munk model accounts for the simultaneous absorption and scattering of laser and luminescence lights traveling in the depth of the material, along the x-axis, in two opposite directions. The notations are illustrated in Figure 17. At any point x, the incident laser light intensity traveling toward the bond coat is denoted by I_{laser} and that traveling back toward the TBC top surface is denoted by J_{laser}. Similarly, the intensities of the luminescence light traveling toward the bond coat and back to the top surface of the TBC are denoted by I_{lum} and J_{lum}, respectively.

The governing differential equation describing the intensities of the incident light traveling in and out (refer to Figure 17) can be formulated in a matrix form, as given by Equation 16.

$$\begin{Bmatrix} I'_{laser} \\ J'_{laser} \end{Bmatrix} = \begin{bmatrix} -(K_{laser} + S_{laser}) & S_{laser} \\ -S_{laser} & K_{laser} + S_{laser} \end{bmatrix} \begin{Bmatrix} I_{laser} \\ J_{laser} \end{Bmatrix} \tag{8}$$

where I'_{laser} and J'_{laser} denote differentiation of I_{laser} and J_{laser} with respect to x, respectively.

The luminescence is assumed to occur due to the incident lights I_{laser} and J_{laser} for a certain quantum efficiency (q) of the material. Therefore, the governing equation for the luminescence light can be defined as given in Equation 17.

$$\begin{Bmatrix} I'_{lum} \\ J'_{lum} \end{Bmatrix} = \begin{bmatrix} -(K_{lum}+S_{lum}) & S_{lum} \\ -S_{lum} & K_{lum}+S_{lum} \end{bmatrix} \begin{Bmatrix} I_{lum} \\ J_{lum} \end{Bmatrix} + \begin{bmatrix} \frac{qK_{laser}}{2} & \frac{qK_{laser}}{2} \\ -\frac{qK_{laser}}{2} & -\frac{qK_{laser}}{2} \end{bmatrix} \begin{Bmatrix} I_{laser} \\ J_{laser} \end{Bmatrix} \tag{9}$$

In the above equations, $K_* = 2k_*$, and $S_* = 2s_*$, where k_* and s_* are the respective absorption and scattering coefficients of the media, and q is the quantum efficiency. Equations 16 and 17 present the Kubelka-Munk model to describe the excitation (laser) and emission (luminescence) intensities at any position x into the TBC with I_* and J_* representing light traveling in the positive and negative x, respectively. The second term in Equation 17 accounts for the luminescence arising from the phosphors by the incident intensity. The intensity of the luminescence is governed by the quantum efficiency (q) which is taken as 0.5 in this study for all three materials [66]. To use the governing equation for discrete layers, the second term was modified in this model using the Heaviside step function such that the luminescence occurs only in the doped layer given by Equation 10.

$$\mathscr{H}(x-x_1)\mathscr{H}(x_2-x) \begin{bmatrix} \frac{qK_{laser}}{2} & \frac{qK_{laser}}{2} \\ -\frac{qK_{laser}}{2} & -\frac{qK_{laser}}{2} \end{bmatrix} \begin{Bmatrix} I_{laser} \\ J_{laser} \end{Bmatrix}, \tag{10}$$

where x_1 and x_2 are the positions of the doped layer (refer to Figure 16) and $\mathscr{H}(x)$ is the Heaviside step function.

The boundary conditions were implemented accounting for the intensity of the incident light ($I_{laser}(x=0) = 100\,a.u.$ and $I_{lum}(x=0) = 0$) and the reflection coefficient R at the bond coat (set at 0.15 as defined in [176]). The boundary conditions used to solve the governing differential equations are also depicted in Figure 17.

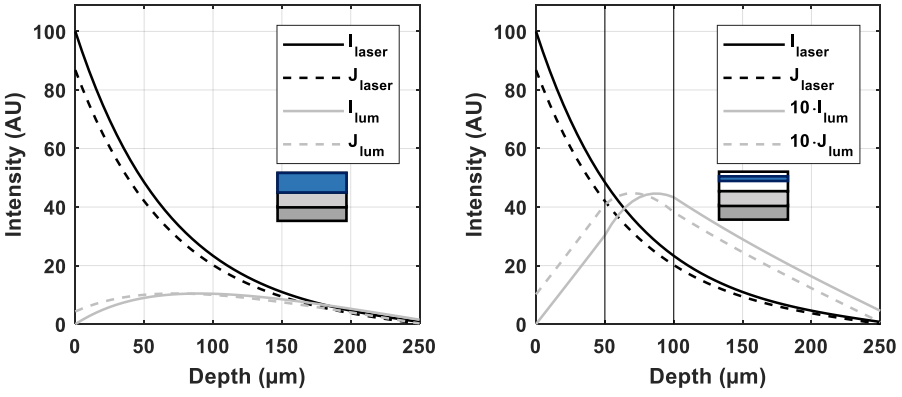

(a) (b)

*Figure 18: Distribution of excitation laser and luminescence intensities through the coating based on Kubelka-Munk model for YSZ:Dy for (a) fully doped top coat **(C1)** and (b) configuration **(C2)** with 50 μm doped layer positioned at 50 μm from the surface.*

The solutions of the Kubelka-Munk model described above to predict intensities at different positions of the top coat are shown in Figures 18(a) and 18(b), for the configurations **(C1)** and **(C2)**, respectively. These solutions correspond to the case where the TBC is doped with YSZ:Dy, wherein the configuration **(C1)**, the top coat is fully doped while in configuration **(C2)**, the doped layer of YSZ:Dy is embedded in an undoped YSZ top

coat (refer to Figure 15). The wavelengths of the incident (excitation) and luminescence light depend on the dopant that is used. The excitation and luminescence wavelengths associated with the dopants are listed in Table 6. The optical properties of YSZ:Dy have been reported in experimental data [176], when the dopant is added in a small amount (typically $\approx$ 1 - 3 wt.%), can be approximated by that of undoped YSZ. In the different literature references taken for experimental comparison, optical properties of YSZ given in literature [216] provide the best approximation. Therefore, the absorption and scattering coefficients for the specific wavelengths of interest in this study have been taken based on this reference and are listed in Table 6. Further, in the case of the configuration **(C2)**, all the results reported correspond to a TBC configuration where the doped layer has a thickness of 50 μm and is buried at 50 μm from the top surface. The collectable luminescence is the value of J_{lum} at $x = 0$. It can be observed that, for the selected quantum efficiency, the theoretical intensity of the collectable luminescence is 4.3 % of the incident intensity in the case of configuration **(C1)** and 1.0 % of the incident intensity in the case of configuration **(C2)**.

Table 6: Optical properties of YSZ from experimental data published in literature [216].

Material	λ **(nm)**	**scattering coefficient** s **(m^{-1})**	**absorption coefficient** k **(m^{-1})**
Excitation properties			
YSZ:Dy	355	50866	511
YSZ:Er / YSZ:Sm	532	33026	111
Emission properties			
YSZ:Dy	590	29585	95
YSZ:Er	545	32113	107
YSZ:Sm	619	28490	88

Table 7: Collectable intensity (% of incident light) for different TBC configurations with various doped layers.

Collectable intensity (% of incident light)	**YSZ:Dy**	**YSZ:Er**	**YSZ:Sm**
Fully doped TBC: $x_1 = 0$ μm, $x_2 = 250$ μm	4.3	1.4	1.5
Embedded doped layer: $x_1 = 50$ μm, $x_2 = 100$ μm	1.0	0.4	0.4

The effects of the position and the thickness of the doped layer in the configuration **(C2)** are shown in Figure 19(a). The figure shows the effect of varying the position of a YSZ:Dy doped layer that has a fixed thickness of 50 μm in the top coat of the TBC. The collectable intensity decreases from 2.9 % to 0.3 % when the 50 μm thick doped layer is moved from the top surface to a depth of 100 μm. The effect of varying the thickness of the doped layer when it is deposited at the top of the coating is depicted in Figure 19(b). For a doped layer that has no thickness, there will obviously be no luminescence intensity. It can be observed that the collectable intensity reaches a threshold (approximately 4.2 %) for thicknesses bigger than 150 μm. This implies that further increasing the thickness of the doped layer will not contribute to the collectable intensity as the luminescence does not reach the surface when emitted from further in-depth locations. The collectable intensities at the surface of the TBC configurations using different dopant layers are predicted by the model as listed in Table 7. Three materials, YSZ:Dy, YSZ:Er and YSZ:Sm have been chosen due to their promising properties for applications in phosphor thermometry [242, 202, 32]. The optical properties for the materials are listed in Table 6. The scattering and absorption coefficients of the incident light are found to strongly affect the collectable luminescence.

It can be seen that YSZ:Dy exhibits higher luminescence intensity in both **(C1)** and **(C2)** configurations due to the significantly higher scattering and absorption coefficients at the incident wavelength of 355 nm (Table 7).

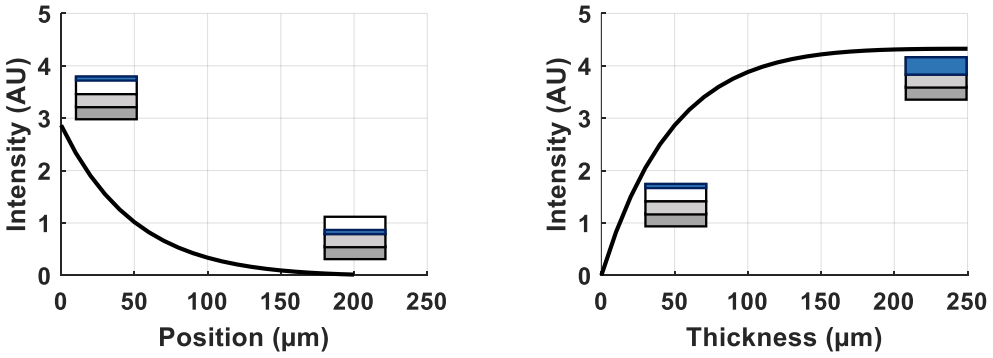

(a) (b)

Figure 19: Effects of (a) position of the doped layer of a constant thickness and (b) thickness of the doped layer when placed at the top on the collectable luminescence intensity predicted by the classical Kubelka-Munk model for YSZ:Dy.

Phosphor thermometry often applies to complex sensing configurations that possess multiple layers that can exhibit distinct optical properties. The Kubelka-Munk model was further adapted for double-layer configurations. In standard TBCs, this configuration exists after some thermal aging, considering that the well-known luminescence of the TGO can be used for luminescence sensing to evaluate temperature, up to 600°C [32], or to characterize stress in the TBC [194].

The modification applied to the Kubelka-Munk model for two distinct layers, labeled **1** (top coat) and **2** (TGO), of dissimilar absorption and scattering coefficients, as presented in Figure 20(a), is given in Equation 11. It can be noted that layer **3** (bond coat) is not considered for light travel but plays a role for interface reflectivity.

$$\begin{Bmatrix} I'_{1,lum} \\ J'_{1,lum} \\ I'_{2,lum} \\ J'_{2,lum} \end{Bmatrix} = \begin{bmatrix} -(K_1+S_1) & S_1 & 0 & 0 \\ -S_1 & K_1+S_1 & 0 & 0 \\ 0 & 0 & -(K_2+S_2) & S_2 \\ 0 & 0 & -S_2 & K_2+S_2 \end{bmatrix} \cdot \begin{Bmatrix} I_{1,lum} \\ J_{1,lum} \\ I_{2,lum} \\ J_{2,lum} \end{Bmatrix} + \begin{bmatrix} 0 & 0 & 0 & 0 \\ 0 & 0 & 0 & 0 \\ 0 & 0 & \frac{q \cdot K_2}{2} & \frac{q \cdot K_2}{2} \\ 0 & 0 & -\frac{q \cdot K_2}{2} & -\frac{q \cdot K_2}{2} \end{bmatrix} \cdot \begin{Bmatrix} I_{1,laser} \\ J_{1,laser} \\ I_{2,laser} \\ J_{2,laser} \end{Bmatrix} \tag{11}$$

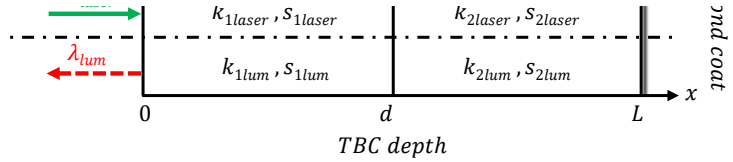

(a) Definition of the layer configuration and optical properties

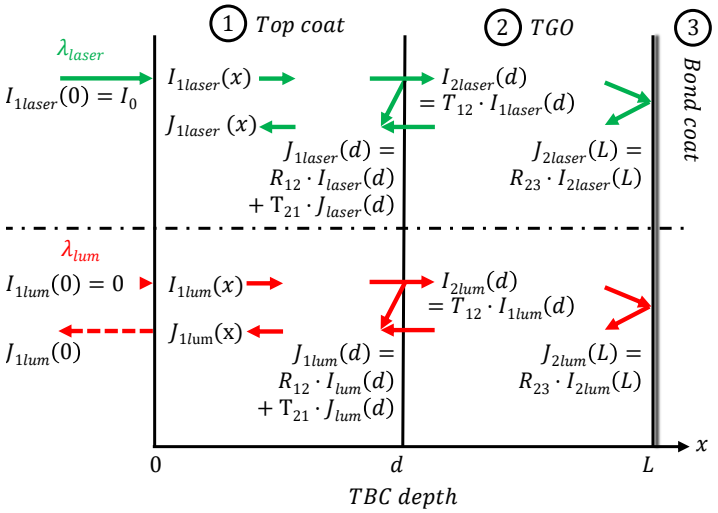

(b) Boundary conditions

Figure 20: Modification of the Kubelka-Munk model for double-layer configuration applications in TBC, in which the TGO is luminescent and the top coat is not.

Regarding the boundary conditions, the percent reflectivity and transmissivity are given by R_{ij} and T_{ij}, where $_{ij}$ represents the layer interaction $i \rightarrow j$. For the numerical study, the optical properties of alumina were taken from literature [171, 49]. The reflectivity at the bond coat was chosen arbitrarily to be 50 %. The quantum efficiency was assumed to be 0.5. The resulting distribution of luminescence intensity, traveling into the TBC, which is for this study comprised of a 200 μm top coat and a 10 μm oxide layer is presented in Figure 21. This model enabled luminescence prediction for the determination of the feasibility of multilayer sensor coatings for phosphor thermometry.

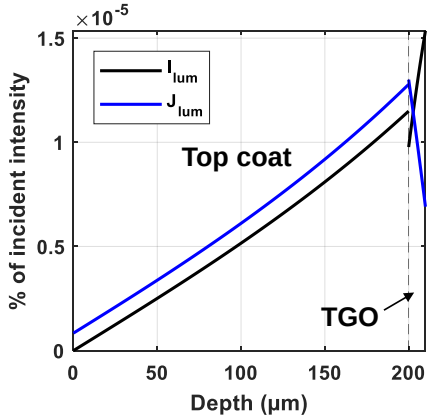

Figure 21: Luminescence intensity produced in TGO is attenuated as it travels back to the top surface. Laser intensity is not shown on this graph.

Location of temperature-dependent luminescence

The previous model was finally extended to account for the time decay behavior of the emerging phosphor luminescence to understand the effectiveness of the TBC configurations applied to phosphor thermometry. The model was applied to multilayered doped TBC configurations to understand the effects of the geometry of the embedded doped layer on the temperature measurement using the lifetime decay method. Three rare-earth doped materials, YSZ:Dy, YSZ:Er and YSZ:Sm were chosen for this study and the in-depth position and the thickness of the added doped layer was incrementally varied to evaluate their influence in the resulting temperature measurement.

While the prediction of the value of luminescence intensity remains critical to ensure the feasibility of data collection at high-temperatures, as the lifetime decay method offers the advantage of higher sensitivity and precision in temperature measurement [106], modeling the decay behavior of the emerging luminescence is of key importance for phosphor thermometry by the decay method. Following an excitation pulse of laser, the decrease of luminescence intensity with time is typically described, for the dopants used in this study, using an exponential function: $I(t) = I_0 e^{-t/\tau(T)}$ in which $\tau(T)$ represents the decay constant that is temperature dependent. Starting from a temperature threshold called quenching temperature, the energy of the phonons is high enough to allow for deexcitation through vibrations between energy levels. The rate of non-radiative emissions is then highly sensitive to temperature which is directly reflected on the rate of emitted photons. To model a realistic TBC environment, a linear temperature distribution with a gradient of 1 K/μm was assumed through the coating thickness. This was used to determine the spatial distribution of $\tau(x)$ [14]. The decay constant and temperature across the depth of the TBC are shown in Figure 22. It has been reported in literature that thermal conductivity of the doped layer is very close to that of the host material (within 5 %), therefore, the temperature distribution in both the configurations **(C1)** and **(C2)** was assumed to possess identical thermal properties as those of the undoped material. However, a model considering the temperature dependence and effects of addition of dopants on the thermal conductivity may be included to obtain more accurate temperature distribution across the TBC.

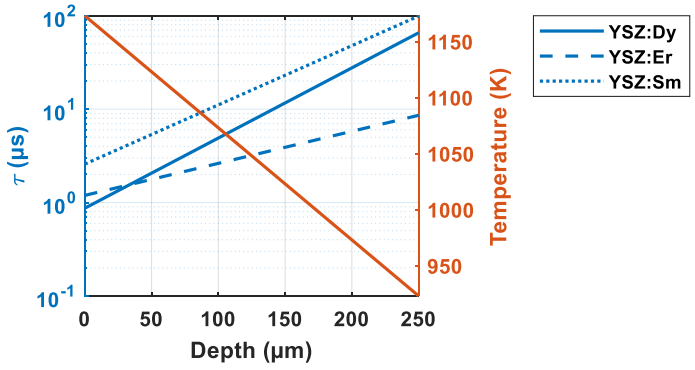

Figure 22: Variation of $\tau(x)$ with TBC in-depth location due to the temperature gradient. Data has been fitted from experimental data published in literature: YSZ:Dy [242], YSZ:Er and YSZ:Sm [202].

The measurement obtained by phosphor thermometry, when there is such a gradient of temperature acting on the TBC is consequently representative of a temperature that can be found at a subsurface location. Indeed, the luminescence arising from a point at higher

temperature will have smaller decay constant than that of the luminescence arising from a point at lower temperature, as represented in Figure 23 ($\tau_1 < \tau_2 < \tau_3$). Thus, the collectable luminescence at the TBC surface is the result of distinct signals coming from in-depth locations into the doped coating with different decay constants. The exponential decay of the luminescence arising from different positions of the TBC was integrated with the Kubelka-Munk model to predict the decay of the collectable luminescence.

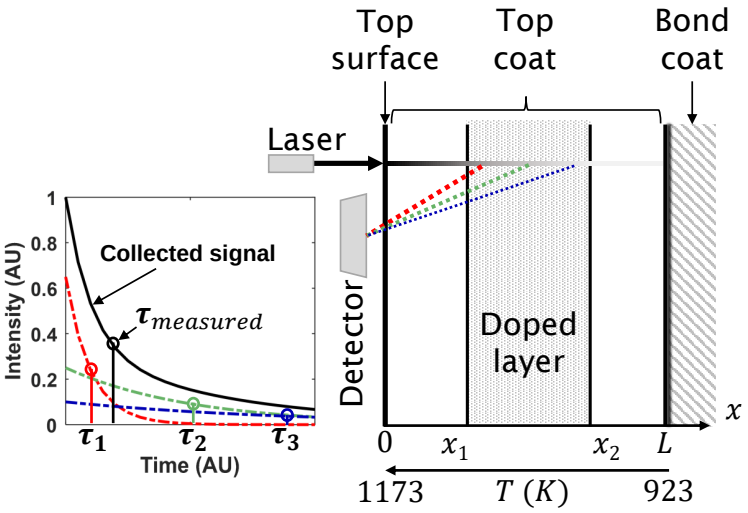

Figure 23: Decay of phosphor luminescence intensity arising from different positions of the TBC with temperature gradation across the coating.

To account for the variation of the decay time of the luminescence at each location in the TBC, the governing equation were modified (refer to Equation 17), so that it includes the luminescence decay contribution, as given in Equation 12.

$$\begin{Bmatrix} I'_{lum} \\ J'_{lum} \end{Bmatrix} = \begin{bmatrix} -(K_{lum}+S_{lum}) & S_{lum} \\ -S_{lum} & K_{lum}+S_{lum} \end{bmatrix} \begin{Bmatrix} I_{lum} \\ J_{lum} \end{Bmatrix} + \phi(x,t) \begin{bmatrix} \frac{qK_{laser}}{2} & \frac{qK_{laser}}{2} \\ -\frac{qK_{laser}}{2} & -\frac{qK_{laser}}{2} \end{bmatrix} \begin{Bmatrix} I_{laser} \\ J_{laser} \end{Bmatrix} \tag{12}$$

where, $\phi(x,t) = e^{-t/\tau(x)}$. In this exponential decay relation, t is the real time and $\tau(x)$ is the decay constant of the luminescence arising from different positions x. The decay constant $\tau(x)$ depends on the position due to the existing temperature gradient across the TBC. This decay form can be justified by the quasi-monoexponential decay behavior of the luminescence of the dopants considered in this study [175, 138, 188].

The time-dependent luminescence coming from different positions of the TBC with the fully doped layer configuration **(C1)** and the TBC with an embedded thin doped layer configuration **(C2)** is shown in Figure 24, and up to 4 μs. As it can be observed from the figure, the part of the luminescence coming from the area close to the top surface emerges with a higher intensity but decays rapidly. On the other hand, the luminescence coming from a more buried position into the TBC has a smaller intensity, but decays slower. The decay of the collectable luminescence ($J_{lum}(x=0)$) can be then fitted using a single-exponential model: $J_0(t) = J_0(t=0)e^{-t/\tau_{eq}}$.

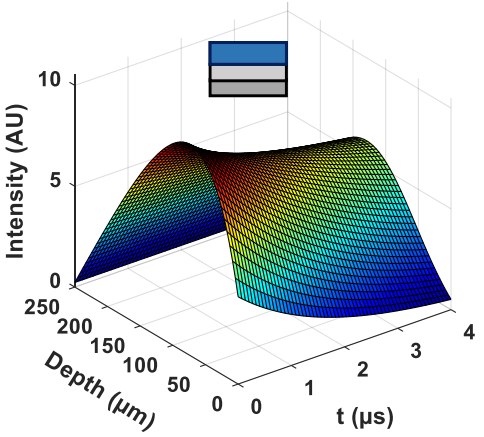

(a) **(C1)**

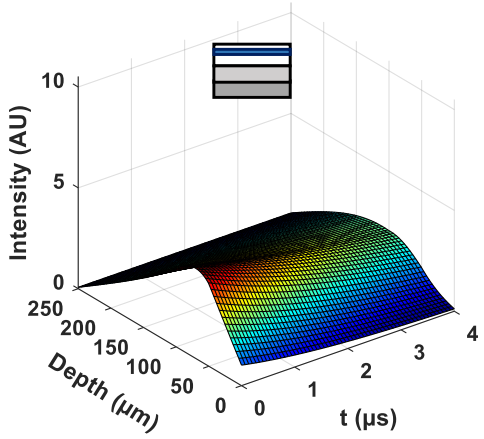

(b) **(C2)**

*Figure 24: Time dependent luminescence at different positions in the TBC obtained from the modified Kubelka-Munk model for (a) fully doped TBC **(C1)** and (b) TBC with a 50 μm doped layer at a depth of 50 μm **(C2)** of YSZ:Dy.*

The decay of the collectable luminescence from the two TBC configurations **(C1)** and **(C2)** are shown in Figures 25(a) and 25(b), respectively. The results that are presented are based on the simulations using YSZ:Dy as the doped material. The luminescence decay that is expected to be generated at both edges of the doped layer are also shown in the figure. In the case of the fully doped TBC configuration **(C1)**, the edges correspond to the surface of the TBC and the bond coat.

It can be noted that the equivalent decay constant of the collectable luminescence has a value in between those of the luminescence from the edges of the doped layer which means that the collectable signal indicates a temperature in a specific location into the doped layer.

The decay constant of the collectable luminescence for the configuration **(C1)** was found to be 1.67 μs, while those of the luminescence arising from the TBC surface and from the top coat - bond coat interface were found to be 0.87 μs and 65.69 μs, respectively. In the configuration **(C2)**, the decay constant of the collectable luminescence is 2.89 μs and that of the luminescence arising from both edges of the doped layer are 2.06 μs and

4.90 μs, respectively. The equivalent decay constant can be experimentally measured and can be used for the validation of this model. The decay constant (τ_{eq}) of the collectable luminescence is further correlated to a particular position, named here equivalent position. This position represents the sub-surface location from which the luminescence decay is similar to that of the collectable luminescence. In other words, it represents the location that is measured using phosphor thermometry.

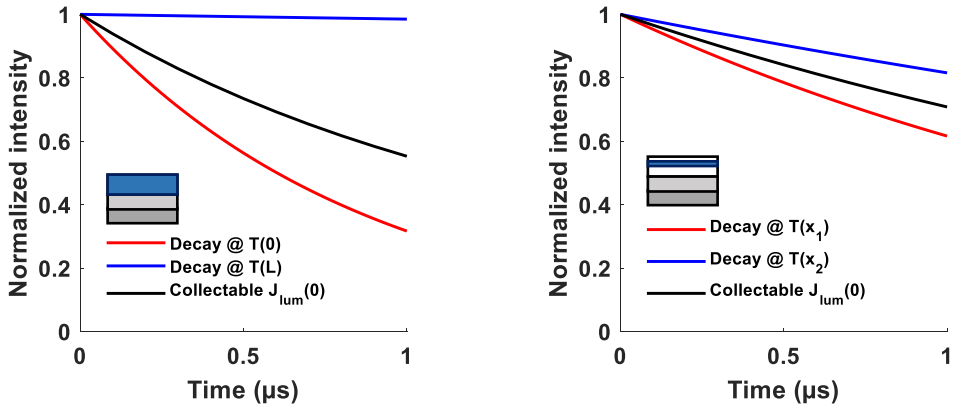

(a) **(C1)** (b) **(C2)**

Figure 25: Decay of the luminescence from different positions in (a) fully doped TBC and (b) TBC with a 50 μm doped layer at a depth of 50 μm of YSZ:Dy.

In order to compare the application of different materials, the modified model was applied to the TBC configurations with three doped materials, YSZ:Dy, YSZ:Er and YSZ:Sm. These rare-earth dopants were chosen for this study since these were demonstrated configurations for phosphor thermometry applications and are applicable to a fairly high temperature of around 900°C. The collectable intensity and equivalent position are presented together in Figure 26 for all the possible positions and thicknesses of the doped layer in the top coat of the TBC. Each map was prepared from the simulation results using the modified Kubelka-Munk model for 325 different geometries by systematically varying the position from $x = 0$ μm to $x = 250$ μm and the thickness from $h = 250 - x$ μm with a step size of $x = 10$ μm. For the YSZ:Dy system, the equivalent position is found to be 38 μm for the configuration containing a fully doped top layer **(C1)**. This means that when sending an excitation pulse to a Dy-doped top coat of thickness 250 μm, the phosphor thermometry instrument gets a signal indicating the temperature at approximately 38 μm from the top surface. For YSZ:Er and YSZ:Sm, the equivalent positions are 53 μm and 47 μm, respectively. Consequently, it is shown that the equivalent position can be controlled by tailoring the TBC configuration. For example, using a YSZ:Dy doped layer in the configuration **(C2)**, the equivalent position results to be 70 μm while it can be moved to 119 μm by positioning the same 50 μm thick doped layer at a depth of 100 μm. However, while displacing the doped layer from an initial depth of 50 μm to 100 μm, the collectable luminescence at the TBC surface is reduced from 1.00 % to 0.34 % of the incident laser intensity, for the given quantum efficiency. The presented maps help to understand the simultaneous effects of modifying the geometry on the final collectable intensity and equivalent position (or estimated sub-surface location), using phosphor thermometry.

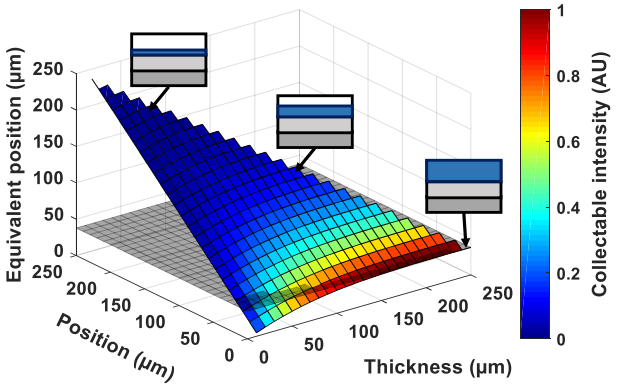

(a) **YSZ:Dy**

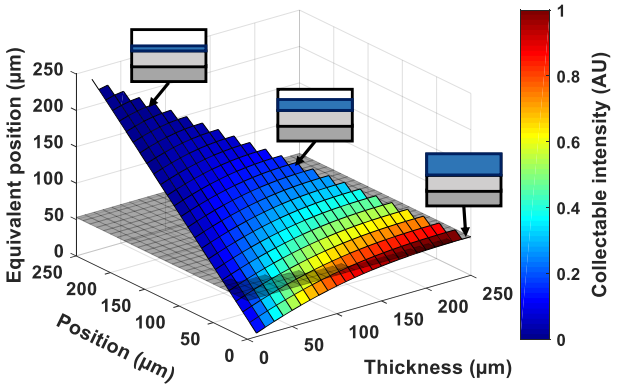

(b) **YSZ:Er**

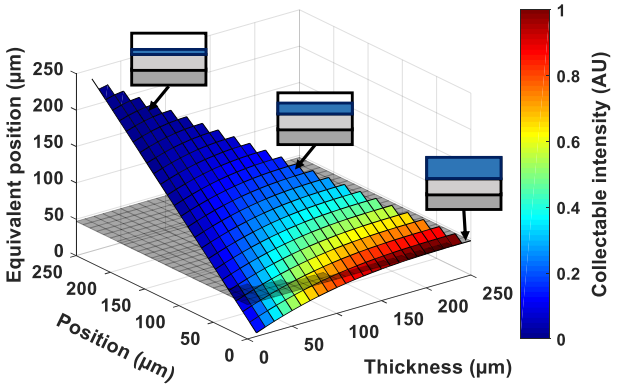

(c) **YSZ:Sm**

Figure 26: Equivalent position (sub-surface location) of temperature measurement and collectable intensity results for varying geometries of the TBC configuration.

The results of equivalent decay constants, obtained after fitting the convoluted signal, for two layered configurations of the TBCs, and made with different doped materials, are presented in Figure 27. Figure 27(a) shows the comparison of equivalent positions and decay constants of the collectable luminescence of the TBC configuration that contains a fully doped top layer **(C1)** and those for the configuration with a 50 μm thick doped layer at a depth of 50 μm **(C2)** are shown in Figure 27(b). It can be noted that, for the fully doped configuration **(C1)**, YSZ:Er provides the temperature representative of the most in-depth position into the coating - 53 μm among the three dopants. However,

in the configuration with a 50 μm doped layer at a depth of 50 μm, the temperature is obtained from nearly similar depth in the coating. The equivalent depth being 70 μm, 72 μm, and 71 μm for the Dy, Er, and Sm dopants, respectively. The equivalent decay constant of the luminescence using Sm is the highest being 5.1 μs and that using Dy and Er are determined to be 1.7 μs and 1.8 μs, respectively, in fully doped configuration. This is due to the inherent longer decay time of the dopant Sm than the other two dopants in this temperature range (refer Figure 22). This feature is conserved in the multilayered configuration also, in which the YSZ:Sm exhibits the higest decay constant. Within the multi-layered TBC configuration, YSZ:Er can provide better temporal resolution due to its smaller decay constant while probing similar in-depth position like the other two materials.

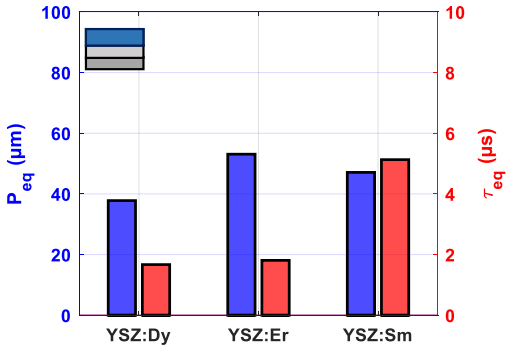

(a) **(C1)**

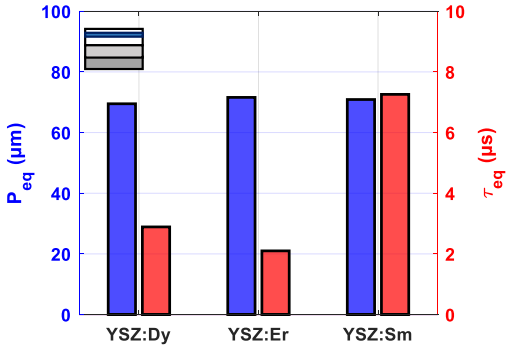

(b) **(C2)**

Figure 27: Intensity and equivalent decay constants of collectable luminescence from the TBC configurations with different materials (a) fully doped top coat ***(C1)*** *and (b) a 50 µm thick doped layer at a depth of 50 µm. The error bar represent the error in fitting the collectable luminescence to determine the equivalent position and decay constant.*

Modeling sensitivity to thermal parameters

The modeling work for light propagation, up to this point, demonstrated the feasibility of predicting, for a known TBC layer configuration, the luminescence intensity that can be collected as well as the sub-surface location that is measured by phosphor thermometry, using the lifetime decay method. However, the results obtained in the previous parts are necessarily associated with the boundary conditions that were selected for the numerical study. In particular, the TBC surface temperature and the gradient were fixed, so the temperature at any point in depth into the coating was known, which is generally not the case in experimental conditions. To determine of the previous models can be used as a supportive tool for real temperature measurements, it is crucial to evaluate the sensitivity of the model to thermal parameters, namely the temperature at the surface of the TBC

and the thermal gradient acting through the TBC. This sensitivity study was important to complete in order to justify the potential applicability of models to predict accurately sub-surface locations that correspond to temperature measurement depths using phosphor thermometry.

For this study, the intensity and decay behavior were modeled in 250 μm-thick luminescent coatings. YSZ:Dy, YSZ:Er and YSZ:Sm fully doped TBCs were used, as in the previous results, for comparison. The extended Kubelka-Munk model was used with the same optical properties as in the previous simulations, given in Table 6. Multiple simulations were run with varying the boundary conditions so that the top surface temperature (T_0) ranges from 973 to 1473 K and the thermal gradient ranges from 0.2 to 1 K/μm. The resulting convoluted luminescence decay, emerging from multiple sub-surface locations exposed at different temperature conditions, are fitted over the time range 0 - 1 μs, using a single-exponential decay model. The obtained decay constant was converted to the corresponding temperature using the known time-response of the phosphor (refer to Figure 22). This ultimately allows to determine the sub-surface location that is being measured by phosphor thermometry. Results are presented in Figure 28 and show the high sensitivity of the measured sub-surface location P_{eq} in YSZ:Dy to the surface temperature and the thermal gradient, at temperatures exceeding 1300 K, which is anyways unpractical using the decay method as the luminescence of the phosphor is quenched. For YSZ:Dy, with a surface temperature that is inferior to 1300 K and for YSZ:Er and YSZ:Sm, for any surface temperature or any gradient, the sub-surface location that is expected to be measured with phosphor thermometry remains almost constant. This is an essential piece of information that can be used to extend the capabilities of the existing methods for temperature characterization in TBCs. The insensitivity of the equivalent position to thermal parameters potentially allows for direct measurements using thick luminescent sensors, revealing sub-surface temperature and internal thermal gradients.

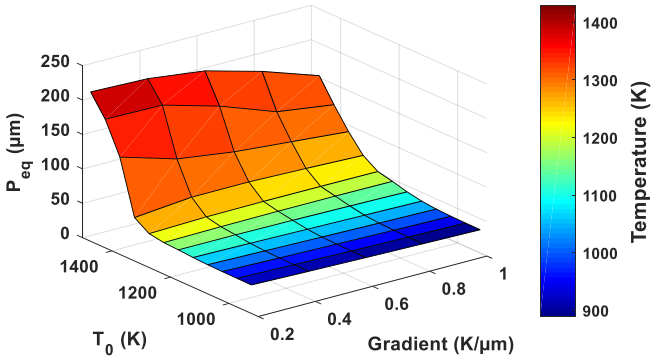

(a) **YSZ:Dy**

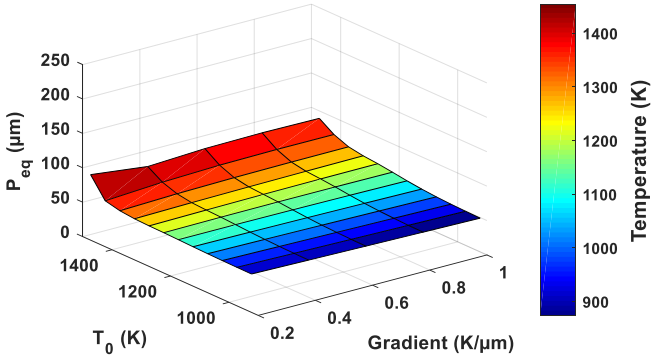

(b) **YSZ:Er**

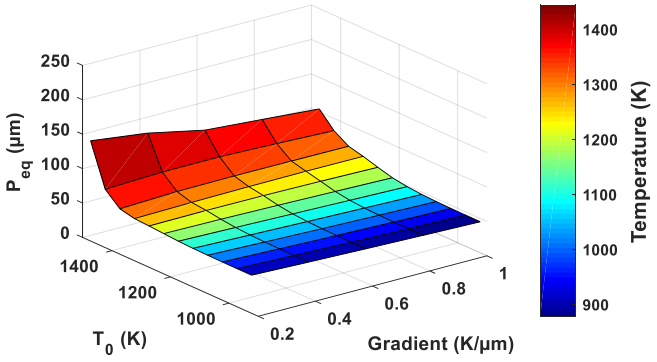

(c) **YSZ:Sm**

Figure 28: Sensitivity of the equivalent position (sub-surface location) of temperature measurement to the gradient of temperature applied through the coating and the surface temperature.

Task 4: Non-intrusive and Well-Benchmarked Measurements: Temperature and Strain Measurements

In Task 4, we developed tools for improved characterization on sensor coatings. We identified two critical gaps: 1- there is no existing data in literature quantifying strains in sensor coatings, and 2- temperature data is not the only information that can be leveraged from sensor coating: coating integrity and coating degradation monitoring is achievable through spectroscopic measurements.

Pioneering strain characterization in sensor coatings

Thermal barrier coatings (TBCs) are widely used to protect metallic high themomechanical load bearing components from extreme temperatures and oxidation in gas turbine engines. These coatings have greatly improved the performance of gas turbine systems as they allow for an increased operating temperature which results in higher cycle efficiencies. TBCs consist of a multilayer structure deposited on superalloy gas turbine blades and composed of a metallic bond coat for adhesion and a ceramic top coat (TC) for thermal protection [37]. The bond coat (BC) material, either deposited as an overlay of MCrAlY (M=Ni or Co) or a diffusion layer of PtAl improves adherence, fatigue resistance, is hot corrosion and oxidation resistant. The bond coat acts as an Al reservoir for the formation of a low growth rate oxidation barrier, or thermally grown oxide, formed via interdiffusion at the interface between the bond coat and the top coat [85, 104]. The state-of-the-art material used for the top coat is porous yttria-stabilized zirconia (YSZ), which exhibits low thermal conductivity (1-2 W/m·K), high coefficient of thermal expansion (9-11·10^{-6} K^{-1}) [237, 181], high strain compliance, high fracture toughness [36] and retains the metastable tetragonal crystal phase between room temperature and up to 1200°C [170, 45, 38]. A concentration of yttria of 7-8 wt.% was found to provide TBCs with the highest resistance to spallation and thermal stability [212]. Further optimization of engine performance using standard YSZ has more recently investigated the use of luminescent rare-earth ions with the perspective of enabling in-situ or ex-situ sensing capabilities, for temperature sensing [77, 7, 54, 68, 111, 93, 33, 74, 78], health monitoring [73, 41, 61, 55, 53, 141, 44, 79] or thermal history sensors [70, 177, 112, 11, 42]. These novel coating configurations intend to provide sensing capabilities with minimal intrusiveness in standard YSZ, usually conserving the amount of zirconia-stabilizing ions to maintain phase stability [213, 224], and therefore preserving nominal coating performance [76, 97]. On a separate aspect, previous studies have shown potential benefits of the substitution of yttria by larger ionic radius rare-earth dopants which have contributed to an additional decrease of thermal conductivity of the ceramic layer [118]. In this work, the depth-resolved in-situ strains contained in novel luminescent rare-earth doped YSZ coatings were studied to determine the effects of dopant addition to TBCs thus predicting the applicability of such sensor TBC configurations to a broader extent and at an industry level.

In addition to experimental efforts on the strain and stress measurements, numerous analytical and numerical studies have been conducted to model the depth-resolved strain and stress in thermal barrier coatings. One area of interest is modeling the as-deposited residual strain in the TBCs, which is generated during the deposition of high temperature splats on the lower temperature substrate, layer by layer in the deposition process [233, 246]. For this purpose, an analytical model was developed for bilayer and multilayer coatings based on the thermal misfit strain between the hot deposited layer and cooler, preheated substrate [40, 220, 246]. This misfit strain leads to induced force and moment between the layers which create the residual stress. Models use the assumption of straight interface between the layers [233, 227, 136], which neglects the local stress concentrations due to the interface roughness. Also, developing finite element analy-

sis (FEA) models is another approach to investigate the residual strain/stress in TBCs [233, 166, 185, 227, 136, 208, 189]. In some cases, the geometry of coating layers was captured from real sample SEM images [166, 185]. The most common way of modeling the interface roughness in FEA models is using an undulation shape like a sinusoidal or semicircle periodic wave [208, 189, 249, 192, 15, 18, 21, 13, 51].

Another area of interest is modeling the thermal stress in thermal barrier coatings under thermal loading like thermal cycles or thermal shock [189, 249, 192, 18, 21, 51]. This thermal stress appears due to the mismatch between the coefficient of thermal expansion (coefficient of thermal expansion mismatch) of different layers or materials nonlinearities including creep behavior. The purpose of thermal cycle loading is to simulate the operation conditions in gas turbines. In these models, more complex phenomena were investigated including creep, especially in the metallic substrate [189, 249, 192, 18, 21], thermally grown oxide (TGO) layer growth between the top coat and bond coat [15, 192, 18, 21, 25, 51, 13], and crack development and delamination between the layers [18, 21, 51]. In addition to FEA approach, analytical models were developed to investigate thermal stress in TBCs [63, 16, 117, 64]. In these models, the undulation interface and the TGO growth were also included. Through all of these mentioned studies, the generated residual and thermal strain/stress in the top coat was found to be one of the most important factors in the failure of thermal barrier coating systems.

Sample fabrication for synchrotron testing

The coatings fabricated in this study were made via air plasma spray which is one of the most prevalent application method for the deposition of TBCs on turbine blades, and is used in particular to equip engines running for extended cycles and prolonged heat exposure. These conditions are typically found in power generation gas turbines. Air plasma spray allows for the fast deposition of the coating via the projection through a plasma plume of partially melted particles onto a substrate. The coating forms from the piling of splats which results in a high scattering, porous microstructure that is favorable for low thermal conductivity, resistance to thermal shock and low in-plane modulus of elasticity [210]. The samples were fabricated using the facility at the Florida Institute of Technology, using a Praxair SG-100 spray gun. 3 mm thick Alloy 247 substrate disks with a diameter of 25.4 mm were provided by Siemens and were grit blasted using alumina blast media prior to the deposition of the bond coat layer (NI-164/NI-211, Praxair). Table 8 shows the deposition parameters for all bond coats and ceramic top coats. No surface preheating was done before deposition of the different layers. A reference top coat (sample R) was fabricated using industry standard 7-8 wt.% YSZ (ZRO-271, Praxair). Two sensor coatings were fabricated, including a full sensor coating (sample F) and a combined sensor coating (sample C). For top coat deposition, sample F used a mixture of YSZ:Er (1.5 wt.% Er, Phosphor Technology) and standard YSZ (ZRO-271, Praxair) with a 1:2 weight ratio. Sample C used a mixture of YSZ:Er (1.5 wt.% Er, Phosphor Technology), YSZ:Eu (3 wt.% Er, Phosphor Technology) and standard YSZ (ZRO-271, Praxair) with a 1:1:4 weight ratio. The different multilayer TBC configurations fabricated for this study are shown in Figure 29. Each disk was sliced with a diamond saw performing two parallel cuts to obtain two circular sections for electron microscopy and luminescence testing, and a pseudo-rectangular piece of width 2.5 mm for standardized volume probed for synchrotron X-ray diffraction measurements.

Table 8: Materials and parameters for the air plasma spray deposition.

Layer	Bond coat	Top coat
Spray distance (cm)	10	7.5
Current (A)	802	902
Voltage (V)	43.3	43.7
Argon (SLM)	49.1	25.5
Helium (SLM)	20.3	20.8
Gun translational speed (mm/s)	300	150
Feeding wheel speed (rpm)	1.17	3.29 (YSZ), 0.48 (YSZ:Er and YSZ:Eu)

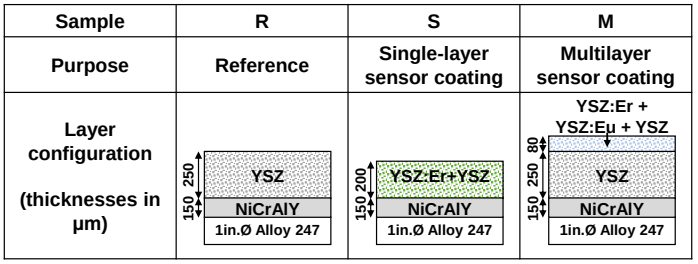

Figure 29: Samples manufactured at the Florida Institute of Technology using air plasma spray.

Microstructure of coatings

Micrographs of the samples were taken with and are presented in Figure 30. The APS as-deposited TBCs show relative homogeneity between rare-earth doped and undoped YSZ material layers. Porosity and surface roughness analyses were performed for the top coats using ImageJ [197]. Sample R, the reference sample, with standard YSZ top coat, has a top coat porosity of approximately 35% and a surface roughness of 8.7 μm. Sample F, fully luminescent YSZ:Er top coat, has a porosity of 20% and a surface roughness of 6.5 μm. Sample C corresponds to the multilayer configuration with a top coat including a standard YSZ base layer with a porosity of 21% and a co-doped YSZ:Er,Eu top layer with a porosity of 15% and a surface roughness of 7.0 μm. It is hypothesized that the lower porosity of the rare-earth doped layer is due to the finer particle size of the preprocessing powders that were used for the mixture as well as the slower deposition rate used for deposition and potentially higher melting temperature of the doped powder. The increased porosity means for lower Young's modulus [146] and increased strain tolerance. A greater porosity means scattered thermal radiation and reduced conduction [134]. Larger stresses may also form preferentially in rare-earth doped top coat portions as they correspond to the areas of reduced porosity.

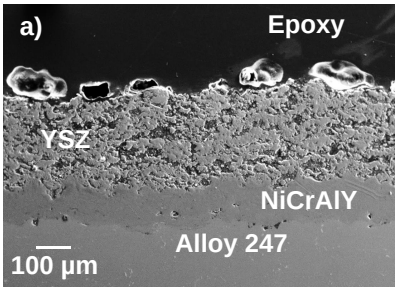

(a) Sample R: Reference coating containing standard YSZ.

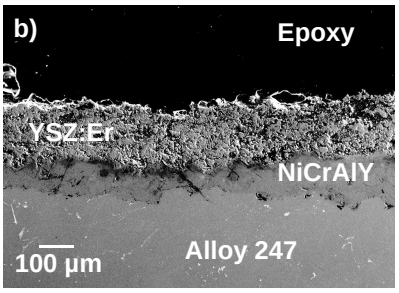

(b) Sample F: Full sensor coating of YSZ:Er.

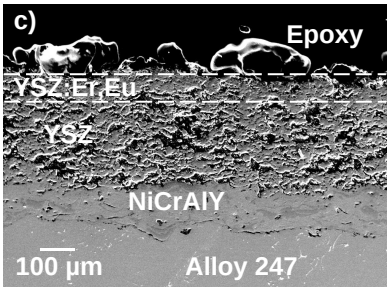

(c) Sample C: Combined sensor coating with top layer containing both YSZ:Er and YSZ:Eu and bottom layer containing standard YSZ.

Figure 30: Micrographs of the TBC configurations.

Experimental setup at the beamline

The experiments were conducted at the beamline 1-ID of the Advanced Photon Source at Argonne National Laboratory. The high-energy beamline is ideal for material characterization including crystal phase volume fraction, grain size, texture and quantification of stress/strain. A nickel-based ultra-high temperature Alloy X (McMaster-Carr) sample holder was manufactured to hold two samples face-to-face simultaneously, as shown in Figure 31. A K-type thermocouple was set in contact with the top surface of one of the samples and placed below the incident X-ray beam area to obtain temperatures measurements as close as possible from the area of interest without disruption for data acquisition. The sample holder was then mounted inside an infrared heater which includes beam entrance and exit holes for direct and diffracted beams, respectively. Alignment and calibration was achieved prior experimentation using ceria powder (CeO_2, NIST Standard Reference Material SRM-674a), with an X-ray beam energy of 71.68 keV and a sample-to-detector distance of 1780 mm. Fit2D [98] was used to refine detector parameters. The sample holder was mounted on a moving stage that allows to move the sample and probe different

locations on coatings during experimentation [205, 155]. Previous studies have applied this experimental setup successfully to capture in-situ strains within TBCs [127, 126, 154]. For each sample, three line scans separated by 1 mm from each other in the in-plane (vertical) direction were completed to get an average strain distribution in the depth of the TBCs. For each line scan, points were acquired in the out-of-plane direction (horizontally, across the thickness of the coatings) and with a distance of 15 μm between each point. X-ray beam passes through a 150 $\times$ 400 μm^2 slit as it enters the beamline and is further reduced using focusing lenses to obtain a 15 (out-of-plane direction) $\times$ 150 (in-plane direction) μm^2 probing area. X-ray beam orientation is shown in Figure 31. This beam orientation ensures sufficient volume is probed for each point in the in-plane direction, as well as to reduce texture by averaging signal from randomly oriented crystal grains (crystallite size is approximately 100 nm). Tomography measurements were done prior to experimentation to adjust surface alignment such that the three line scans can be compared point-by-point. The diffraction peak intensity of $t'-$YSZ (101) was used as a marker of top coat limits for this alignment. The thermal profile that was applied to each sample and data acquisition periods for the experiment is given in Figure 31. The 6-minute temperature holds included 1 minute for homogenizing temperature and avoid significant thermal gradients through the top coats before starting data acquisition from the three line scans, which took 5 minutes to complete. Temperature was then rapidly increased after completion of data acquisition, using a 200°C/min ramp rate.

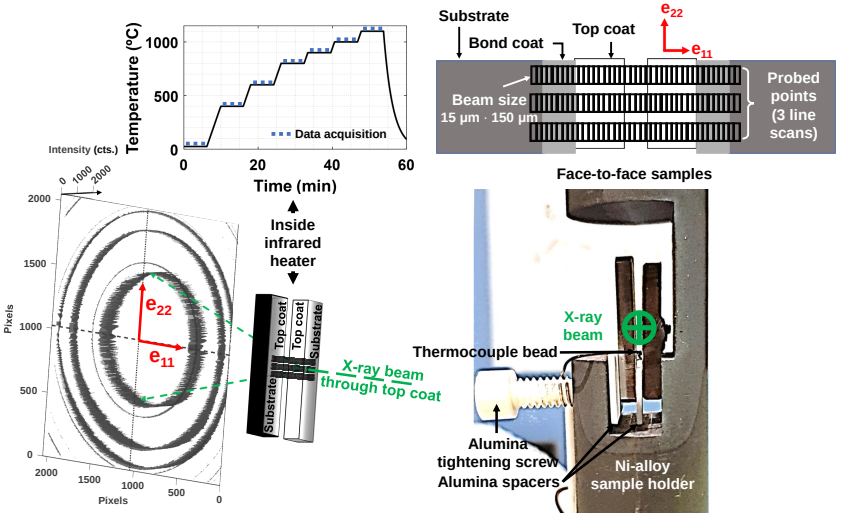

Figure 31: Synchrotron X-ray transmission experimental setup with Debye-Scherrer rings obtained from sample R, and thermal profile for the in-situ experiment at the beamline.

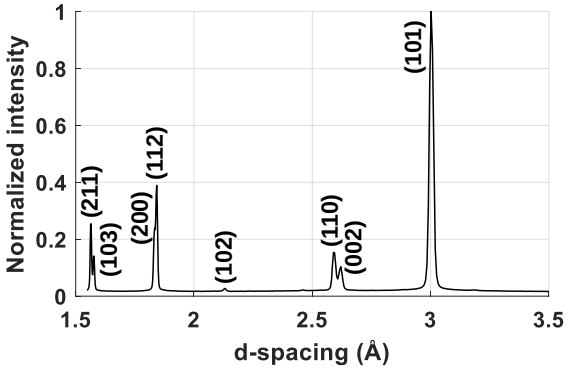

Figure 32: XRD lineout of the surface of sample R showing $t'-$YSZ at 1100°C.

Data analysis

The diffraction pattern was collected using a GE-41RT, 2048×2048 pixels area detector. The resulting matrix of X-ray intensities is composed of individual pixels that can be given in polar coordinates I(r,η), where r is the radial distance from the center of the Debye-Scherrer ring to the pixel being investigated and η is the azimuthal angle between the x-axis and the vector Or [8, 105]. The diffraction rings were integrated to obtain averaged lineouts, as the one shown in Figure 32, using an azimuthal bin size of 5°. r was converted to d-spacing using Bragg's law. A strain-free reference angle for each diffraction ring, η^*, was measured for the strain free radial position, r_0 and implemented into the strain equation, $\varepsilon = (r\text{-}r_0)/r_0$. This angle was calculated from the X-ray elastic constants using DECcalc [157]. Poisson ratio was determined using the Kröner-Eshelby method [169] and given in Table 9 for each diffraction plane.

Table 9: Numerical values used for the η^* method based on the Kröner-Eshelby model and using the elastic stiffness constants of YSZ [150].

t'-YSZ lattice plane used for strain analysis	**{101}**	**{110}**	**{112}**	**{211}**
ν_{hkl}	0.348	0.338	0.342	0.344
η^* (°) zero strain reference angle	45.9	45.3	45.6	45.7
S_1 (MPa^{-1})	-1.96×10^{-6}	-1.41×10^{-6}	-2.05×10^{-6}	-1.61×10^{-6}
$\frac{1}{2}S_2$ (MPa^{-1})	7.61×10^{-6}	5.60×10^{-6}	8.06×10^{-6}	6.30×10^{-6}

The peaks were fitted using a pseudo-Voigt function to obtain radial values R_η that were then converted to d-spacing values using Bragg's law, d_η, for a given azimuthal bin. Both the in-plane strain (ε_{22} along the axis passing by $\eta = \frac{\pi}{2}$ and $\frac{3\pi}{2}$) and out-of-plane strain (ε_{11} along the axis passing by $\eta = 0$ and π) were calculated with the resulting bistrain plots. It should be noted that this study only reports deviatoric strain and not hydrostatic strain, as the hydrostatic strain expands the diffraction ring uniformly around the azimuth, but does not alter the angle at which the strain-free reference is calculated.

Numerical simulations

In this section, numerical models were developed to estimate as-deposited residual stresses at room temperature and thermal stress due to the experimental thermal load, as shown in Figure 31, in the three different sample configurations. As mentioned in the introduction, developing FEA models provides the capability of investigation in the residual and thermal strain/stress in the multilayer TBCs. The FEA models could include the modeling of interface roughness between the layers by using an undulation shape, and also the creep behavior of the various layers, in particular that of the metallic substrate. In this work, finite element simulations were carried out using commercially available software ABAQUS/CAE 2017 (Dassault Systèmes). Usually, some idealizations and simplifications are assumed in computational models for TBCs to achieve a reasonable computation time alongside with a realistic response due to complex materials behavior. Three different models were considered to study sample configurations R, F, and C. Also, to investigate the role of local roughness at TC/BC interface, two different interface geometries for each sample configurations were considered, as shown in Figure 33. In the first interface geometry, the interface was assumed to be straight and the stress at the top coat was obtained along a path named "Straight Interface", or SI, as displayed in Figure 33. In the second

interface geometry, typical interface roughness between the bond coat layer and top coat layer was assumed. A semicircular periodic geometry with amplitude 20 μm was selected to approximate the undulations of the interface which can be observed using microscopy, and as shown schematically in Figure 33 [18, 21, 51, 13]. In this case, two distinct paths were simulated, either through the “Interface Peak" (IP) or through the “Interface Valley" (IV). Perfect bonding is assumed between TBC layers. The models considered an arbitrary cut in the middle of a TBC system. Thus, due to symmetry, the FE model was defined as an axisymmetric model using ABAQUS with an axisymmetry boundary condition on the left side of the geometries [189, 249, 185, 208]. This model attempts to represent a portion of the actual TBC systems, therefore, to impose the periodicity boundary condition on the right side of the model, a multipoint constraint (MPC) boundary condition was applied to allow the nodes on this edge to move freely and simultaneously [1, 189, 130, 15]. The bottom left corner was fixed in y-direction to avoid rigid body motion of the whole model in y-direction.

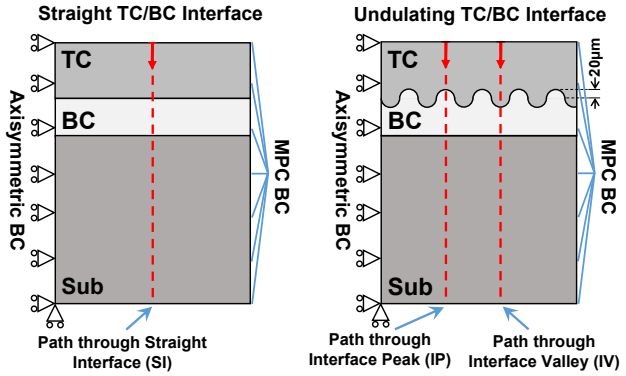

Figure 33: Different paths through the layers of thermal barrier coatings were assumed for the simulation, not to scale.

For these FE simulations, in total six different models were developed for the three different sample configurations which are shown in Figure 29, and for each sample configuration, two different interface geometries, straight interface and undulating interface, were considered. In these models, the axisymmetric quadrilateral 8-node quadratic elements (CAX8T) and axisymmetric triangle 6-node quadratic elements (CAX6T) were utilized. A mesh convergence study was carried out to find sufficient mesh density for different areas of the model. For the models with straight interface, the number of elements is approximately 12,000. For the models with undulating interface, the number of elements is approximately 70,000 due to the more complex interface geometry.

In this work, the TBC system is composed of a YSZ top coat, a NiCrAlY bond coat, and an Alloy 247 substrate. The thickness of layers for different configurations are presented in Figure 29. The material properties of the layers are listed in Table 10 as function of temperature [21, 166, 51, 249, 186, 28], including modulus of elasticity (E), Poisson’s ratio (ν), coefficient of thermal expansion (α), density (ρ), thermal conductivity (k), and specific heat (c_p).

In addition to mentioned material properties, the temperature-dependent creep behavior was taken into account for all three layers. The Norton power law creep behavior was utilized according to the following equation:

$$\dot{\varepsilon}_{cr} = A\sigma^n \tag{13}$$

where $\dot{\varepsilon}_{cr}$, A, σ and n are the creep strain rate, stress pre-factor, stress, and creep exponent,

Table 10: Material properties of different layers of the system

Layer	T (°C)	E (GPa)	ν	α (10^{-6}/K)	ρ (kg/m^3)	k (W/mK)	c_p (J/kgK)
	20	17.5	0.2	9.68	5400	1.5	456
	200	16.44	0.2	9.67	5400	1.5	535
	400	15.28	0.2	9.7	5400	1.5	579
Top Coat	600	14.12	0.2	9.79	5400	1.5	604
(YSZ)	800	12.96	0.2	10	5400	1.5	624
	1000	11.8	0.2	10.34	5400	1.5	642
	1100	11.22	0.2	10.58	5400	1.5	648
		[21]	[21]	[21]	[166]	[51]	[51]
	20	200	0.3	13.6	7320	4.2	540
	200	190	0.3	14.2	7320	5.35	630
	400	175	0.31	14.6	7320	6.4	695
Bond Coat	600	160	0.31	15.2	7320	8.35	722
(NiCoCrAlY)	800	145	0.32	16.1	7320	10.1	743
	1000	120	0.33	17.2	7320	11.8	765
	1100	110	0.33	17.6	7320	12.6	775
		[249]	[249]	[249]	[166]	[51]	[51]
	20	198	0.16	12.45	8630	8.13	400
	200	191	0.16	12.71	8570	10.1	440
	400	180	0.16	13.19	8500	13.6	480
Substrate	600	169	0.16	13.61	8430	16.9	510
(Alloy 247)	800	157	0.16	14.25	8350	20.4	540
	1000	140	0.16	15.56	8250	21.3	563
	1100	128	0.16	16.65	8190	21.55	573
		[186]	[186]	[28]	[28]	[28]	[28]

respectively. The coefficients A and n are listed in Table 11 as function of temperature [192, 1, 18].

Table 11: Creep properties of the different layers of the system

Layer	T (°C)	A (MPa^{-n}/s)	n
Top Coat	1000	1.80×10^{-7}	1
(YSZ) [192]	1200	1.80×10^{-7}	1
	≤600	6.54×10^{-19}	4.57
Bond Coat	700	2.2×10^{-12}	2.99
(NiCoCrAlY) [1]	800	1.84×10^{-7}	1.55
	≥850	2.15×10^{-8}	2.45
Substrate	10	4.85×10^{-36}	1
(Alloy 247) [18]	1200	2.25×10^{-9}	3

During the air plasma spray deposition process, the coating builds up layer-by-layer, each pass containing splats of individual thickness comprised in the range of 1-5 μm and typically resulting in a pass thickness of approximately 10-20 μm [170, 20]. During the thermal spray deposition, the coating's residual stress state is altered due to high air plasma spray splat temperature. Thus, the as-deposited residual stress must be taken into account to obtain a realistic model. The model was set as a transient coupled temperature–displacement analysis with nonlinear geometry option in ABAQUS. Air plasma spray of top coat powder onto the surface of bond coat layer from a plasma gun was modeled by adding the top coat's elements layer-by-layer to the model using the "Model Change" option in ABAQUS in each time step, with layer thickness of 10 μm, as shown in Figure 34. The layers were considered stress-free with the melting temperature as the melting temperature of YSZ splats 2650°C [166, 189]. For sample F and C, the melting temperatures for layers associated with the doped layers of YSZ:Er+YSZ and YSZ:Er+YSZ:Eu+YSZ were assumed to be in the range of 2650±50°C. This temperature range was implemented in the model by taking minimum temperature and maximum temperature of this range as input as to account for the possible effect of rare-earth dopant addition on the melting temperature of the feedstock powder, as there is limited literature to quantify more precisely melting temperature variation [12]. The results showed no significant effect of melting temperature in final post-deposition stress results, with a maximum deviation of 4% with respect to results obtained using the reference melting temperature of 2650°C and were therefore not reported in the plots. The time step for each layer deposition was set to 1 s, and after the deposition of the last layer, a 1200 s cooling time step was implemented for the system to reach room temperature. Due to the mismatch between coefficients of thermal expansion of the different layers, residual stress accumulated in the thermal barrier coating in the as-deposited condition.

For sample C, after modeling the layer-by-layer deposition of YSZ top coat with 250 μm, a 300 s cooling time step was imposed. Then, the layer-by-layer deposition of the YSZ:Er+YSZ:Eu+YSZ top coat was modeled to achieve an extra 80 μm thickness with a 1 s per layer deposition rate. Finally, a 1200 s cooling time step was given to the whole system to cool down to room temperature. In addition to the modeling of the deposition steps, multiple transient coupled temperature–displacement steps were included to the FEA to analyze the thermal stress due to the thermal load applied post-deposition to the outer surface of the TBC system, as shown in Figure 31.

During the deposition procedure, transient temperature distribution in the layers including substrate, bond coat, and deposited top coat depends on the heat generated by the added top coat layers with melting temperature, heat conduction between the layers, and the

radiative and convective heat flux out of the top and bottom surface of the system, as shown in Figure 34. The heat generated by the high temperature added layer and radiative and convective heat flux out of the surfaces can be denoted as $\dot{q}_{in}$ and $\dot{q}_{out}$, respectively [233]. The lost heat flux can be considered as follows [233]:

$$\dot{q}_{out} = h(T - T_\infty) + \epsilon\sigma(T^4 - T_\infty^4), \tag{14}$$

where h, ϵ, σ, T, and T_∞ are convection coefficient, emissivity, Stefan–Boltzmann constant, temperature of the surface, and ambient or room temperature (25°C), respectively. Convection coefficient h of air with free convection was considered to be 25 W/(m^{2}K) [129]. The emissivity for the YSZ was estimated to be 0.729 [4].

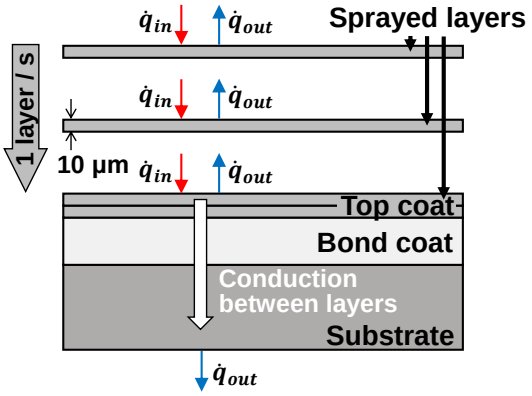

Figure 34: Schematic of layer-by-layer top coat deposition.

Results and discussion

Strain analysis using the four peaks presented in Table 9 was performed for data collected at 800°C and 90 μm from the top surface of each sample to compare the interface strain from sample C where the rare-earth doped layer was applied with the other samples that present a single layer to form the top coat. The lowest strain magnitude at 90 μm from the surface is found in sample R, followed with sample F and sample C that exhibits higher strain at this location, as highlighted in Figure 35 which presents the strain from top surface to the interface between the top coat and the bond coat for all samples and at different temperatures. It can be noted that the measurement at 1100°C for sample C was not achieved because the sample tipped due to thermal expansion and moved away from the probing zone.

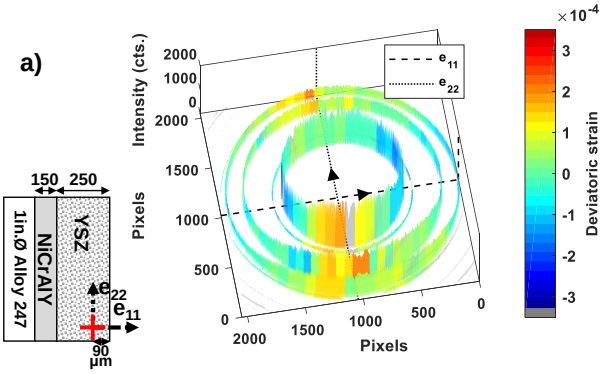

(a) Sample R: Reference coating containing standard YSZ.

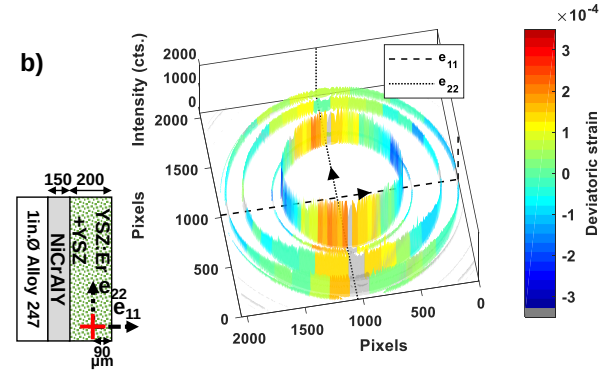

(b) Sample F: Full sensor coating of YSZ:Er.

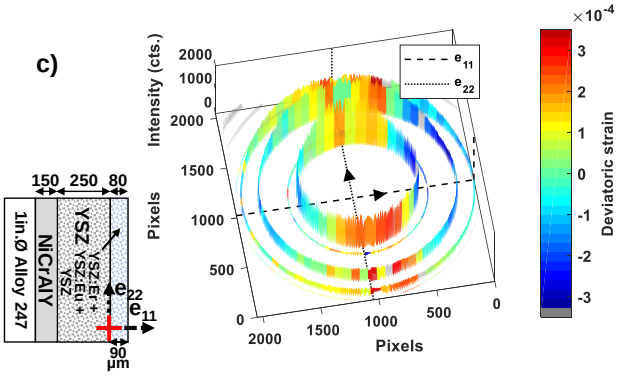

(c) Sample C: Combined sensor coating with top layer containing both YSZ:Er and YSZ:Eu and bottom layer containing standard YSZ.

Figure 35: In-situ strain measured at 90 µm from surface of TBCs at 800° C.

The strain results are presented in Figure 36. It is important to highlight that the internal strains that are present in those samples built up during air plasma spray deposition and the materials were not cycled such that they exhibit typical tensile in-plane strain across the thickness of the APS coating [140, 222, 124].

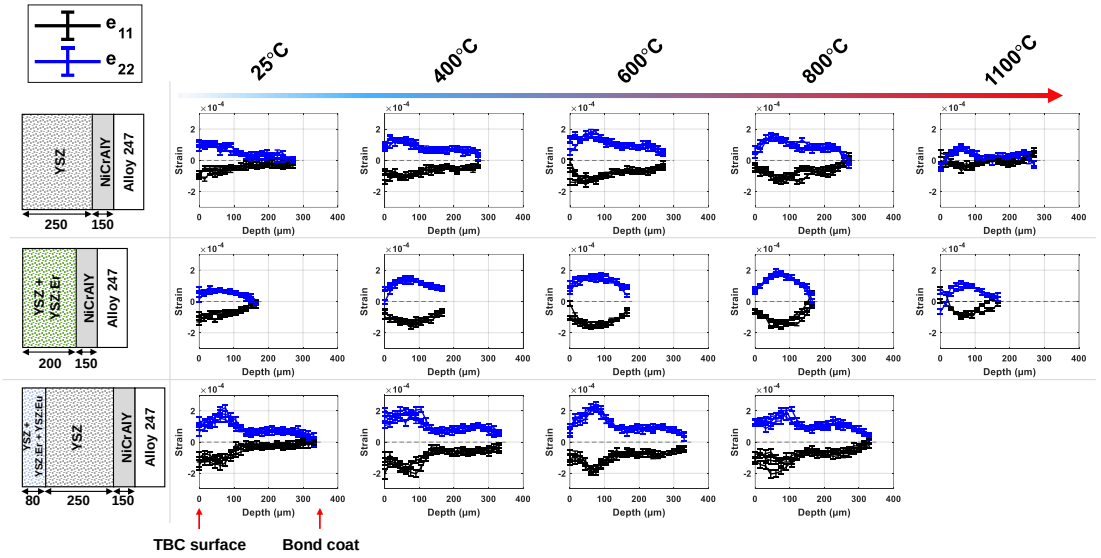

Figure 36: Depth-resolved strain results at different temperatures.

Stress results

The deviatoric strain values were converted to stress using Equation 15 [103]. The biaxial strain assumption gives $\varepsilon_{22} = \varepsilon_{33}$.

$$\sigma_{22} = \frac{1}{\frac{1}{2}S_2}(\varepsilon_{22} - \frac{S_1}{\frac{1}{2}S_2 + 3S_1}(\varepsilon_{11} + 2\varepsilon_{22})) \tag{15}$$

The residual and thermal stresses were found at different locations in the top coats including top surface, coating midpoint (independently of whether the top coat is composed of a single layer or has a multilayer structure) and the interface between the top coat and the bond coat. The results are presented in Figure 37 and show the mostly tensile state of stress (σ_{22}) of the coatings. Low stress in as-deposited APS coatings are expected due to the brittle nature of the ceramic top coats [159]. It can be highlighted that sample C exhibits the highest residual (room temperature) stress at all locations. This could be generated during the top rare-earth doped layer deposition. The interface between the top coat and the bond coat corresponds to a sensitive spot that drives failure mechanisms in TBCs. Therefore, it is important to characterize the stress around this location during the lifetime of coatings. This information provides insights on coating degradation.

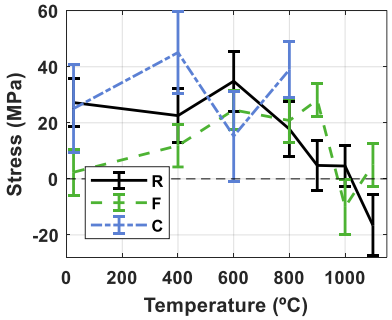

(a) Coating surface.

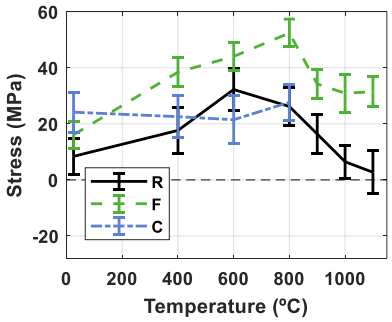

(b) Coating midpoint.

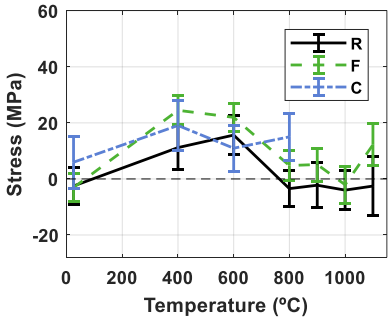

(c) Interface between top coat and bond coat.

Figure 37: Comparison of in-plane stress σ_{22} at comparable depths for the different TBC configurations.

Numerical model results and comparisons with experiments

The deposition of top coat was modeled to replicate the layer-by-layer deposition process used in APS, in which at each time step, one layer with thickness of 10 μm is added to the model. In Figure 38, in the first row, the layer-by-layer deposition is illustrated by representing stress contour plots of the model at four different time spots during the top coat deposition.

The second row of Figure 38 is representing the contour plots of thermal stress in the TBC system due to the thermal load applied to the outer surface of the TBC system, which is shown in Figure 31, at four different time spots. As it can be observed during the thermal load, the stress in the top coat is almost constant and the undulating TC/BC interface

geometry only generates a local increase in the stress at the area close to the interface and does not significantly affects the stress distribution far away from the interface in the top coat. These stress contour plots are obtained from the FE modeling of the sample R configuration.

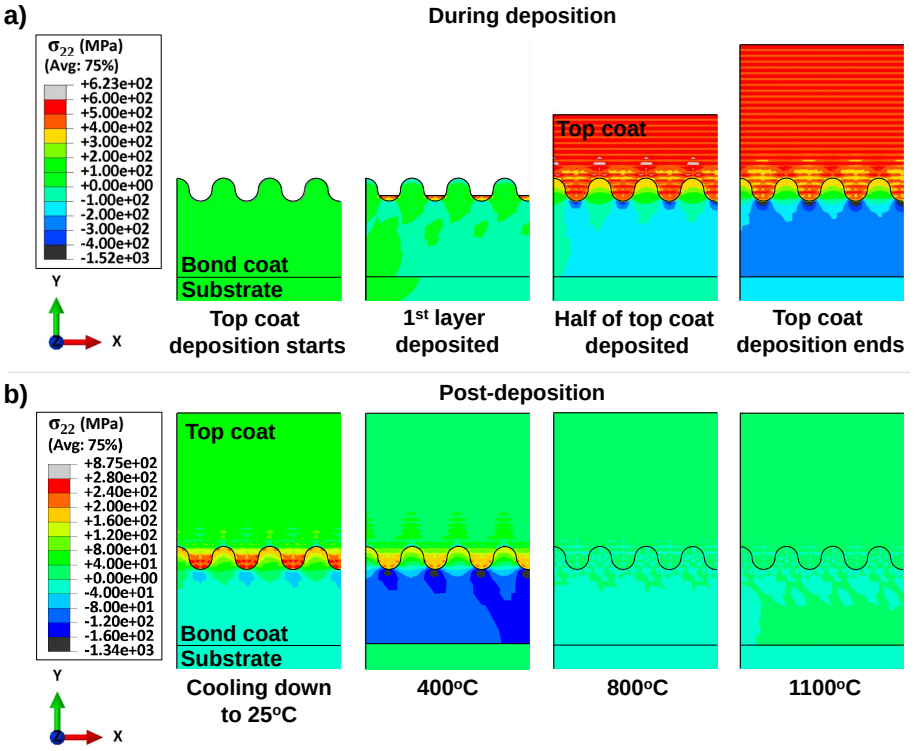

Figure 38: Stress contour plots during the top coat deposition and thermal loading steps for sample R for the model containing undulating TC/BC interface.

Figure 39 shows the comparison of experimental and numerical in-plane stress through the top coat measured from the outer surface. This figure shows the residual stress at room temperature, which is the as-deposited residual stress, and the thermal stress at different temperatures according to the thermal load shown in Figure 31. The raw numerical results show stress oscillations into the coating due to thermal shock occurring between each step of the layer-by-layer air plasma spray deposition process. To enable direct comparison of experimental and numerical results, FE results are presented showing the moving average with a fixed subset size of 15 μm. Experimental measurements provide an average that depends on volume probed, in this case with a resolution of 15 μm through the coating.

As it can be observed in Figure 39, there is a good agreement between the numerical results with the experimental results, despite the simplifications assumed in the FE model. These plots also show that the TC/BC interface geometry has just local effect in the area close to the interface and does not have significant effect on the stress of top coat far away from the interface, and qualitatively does not affect the average of in-plane stress through the thickness of the top coat aggressively. At the stress plots for the sample C, there is an obvious jump related to the the deposition of doped YSZ layer. As it can be observed in Figure 39, the residual stress present in the samples slightly decreases in magnitude as they are brought to high temperatures.

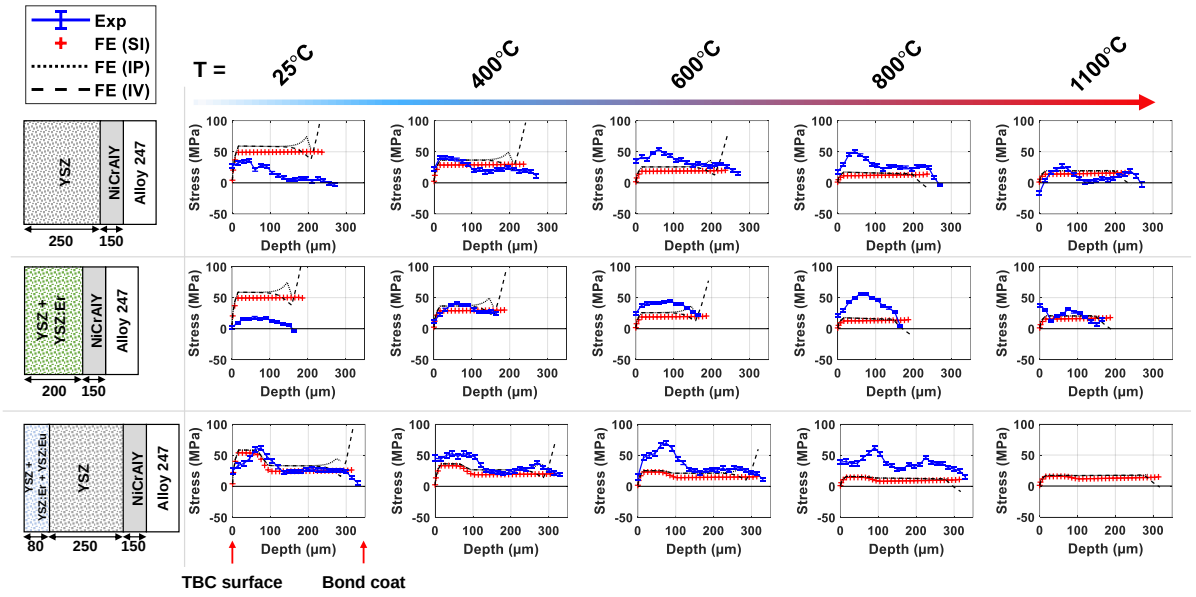

Figure 39: Comparison of experimental and modeled results for in-plane stress.

Conclusive remarks on strain measurements

Recent progress towards the implementation of integrated sensors in thermal barrier coatings for temperature and health monitoring with limited intrusiveness presents great potential in terms of resulting fuel savings, optimization of maintenance schedules and reparation costs. In practice, the embedding of luminescent ions in standard yttria-stabilized zirconia to enable thermal barrier coating multifunctionality is highly promising and is key for better control over gas turbine engine operating parameters. Indeed, such coating configurations allow for in-situ temperature and ex-situ structural integrity monitoring. It is however crucial to improve our understanding on their thermomechanical properties to determine suitability for the safe substitution of turbine blade coatings with no significant reduction of the typical residual stress condition found in industry materials. In this work, synchrotron X-ray diffraction was used to measure in-situ strain in three novel rare-earth doped yttria-stabilized zirconia configurations. Depth-resolved strain contained in top coat layers of multifunctional sensor TBC configurations was quantified in realistic gas turbine engine temperature conditions and in-plane stress was determined from strains. The results reveal in-plane tensile stress in as-deposited air plasma spray coatings which is released as temperature increases up to typical gas turbine engine service temperatures. The results also show that the coatings that were successfully designed and manufactured in this study present similar residual and thermal stress properties, compared to industry yttria-stabilized zirconia coatings, indicating potential suitability of the novel coatings in standard gas turbine engines. The findings are encouraging for the safe implementation of sensor coatings that can combine effective thermal protection, coating lifetime and embedded monitoring capabilities. This work also highlights the importance of thermal-shock induced stress for multilayer configurations and provides a numerical modeling approach to predict and validate depth-resolved stress due to thermal loads and layer deposition parameters that can be used for future designs of multifunctional and multilayer coating configurations.

Sensor coating damage monitoring

Tracking damage and monitoring the integrity of TBCs through their lifetime is essential to prevent engine failure, reduce maintenance costs and increase turbine systems efficiency. To this objective, well-known optical imaging techniques such as infrared thermography are used to reveal delamination progression on coatings. More specifically, these methods use the thermal radiation emitted in the mid-infrared [58, 59, 218, 223] or in the long-wave infrared [41, 152, 29, 101, 248], post-exposition to an intense heat source (generally a flash of light). More recent investigation promotes luminescence-based imaging as an efficient delamination-detection method when doping the ceramic top coat with luminescent rare-earth ions [41, 61, 55, 53, 141, 44]. This allows for high-contrast and high-resolution delamination mapping to better monitor the integrity of engine components that are exposed to extreme environments. Delamination monitoring is therefore achieved through the tracking of luminescence intensity, to highlight areas of enhanced reflectance, corresponding to damage locations. The luminescence-based approach is a more appropriate method to quantify luminescence contrast to detect early stages of delamination as well as crack propagation since it uses shorter wavelengths than those used in infrared methods [60]. Current literature exclusively presents experimental results on configurations which consist of a sensing layer in direct contact with the bond coat, deposited below a standard top coat layer. In addition, no prediction models are available to evaluate delamination progression on luminescent multilayer TBCs. Overall, the interest regarding these new multilayer luminescent sensor TBC configurations has rapidly grown over the past years as they allow not only delamination sensing but also accurate turbine engine temperature measurements via phosphor thermometry [77] and even erosion detection [57, 52]. One key mechanism that generates significant and unpredictable delamination on TBCs is known as foreign-object damage. The effective detection of such potentially serious deterioration is critical to ensure the integrity of turbine blades and it is paramount to accurately predict the advancement of delamination on multilayer TBC configurations. To fill this gap, a 2×2-flux Kubelka-Munk model has been constructed in this work to estimate the luminescence intensity variations that are caused by local delaminations on multilayer sensing coatings. In literature, the Kubelka-Munk model has been successfully implemented to estimate luminescence intensity decays emerging out of TBCs to measure the effects of thermal gradients during engine operation [74, 78, 176]. However, this work shows the first evidence of the effectiveness of this model to quantify luminescence contrast for the detection and monitoring of delamination in TBCs. The drastic change in diffuse internal reflectivity due to the formation of an air gap at the interface between the top coat and the bond coat is used for the characterization of delamination areas. To validate the results of the model experimentally, an artificial delamination was created by Rockwell indentation on two distinct sensing layer configurations.

Coating manufacturing for damage monitoring

The model outcomes were supported by concurrently fabricating two luminescent TBC sample configurations embedding a YSZ:Er^{3+} layer, as represented in Figure 40. Samples consist of a Rene N5 superalloy substrate, a NiPtAl bond coat, a standard 125 μm, 8 wt. % yttria-stabilized zirconia (YSZ) Electron-Beam Physical Vapor Deposition (EB-PVD) TBC and an additional 12.5 μm EB-PVD layer for subsurface delamination sensing composed of 0.8 mol. % erbium-doped YSZ, where the total amount of rare-earth stabilizer was kept constant at 8 wt.% to ensure the prominence of the metastable tetragonal phase of zirconia. For sample A, the doped layer was deposited over the undoped top coat layer which makes it an attractive layer configuration for many ongoing research applications. First of all, placing the sensing layer at the top of the TBC significantly increases the

intensity of the luminescence that can be collected by the detector which facilitates data acquisition. This configuration is also advantageous to avoid direct interaction between the bond coat and the sensing layer, therefore avoiding large uncertainties on interface properties in comparison with industry-standard bonding properties. Finally, a sensing layer placed at the top of the TBC can be further used for erosion indication as the sensing layer on the surface is directly exposed to extreme engine environments. On the other hand, for sample B, the doped layer was placed underneath the undoped top coat, interfacing with the bond coat. This coating configuration provides a better luminescence intensity contrast for delamination assessment as the signal originates from the region that is impacted the most by the drastic change in reflectance below the top coat. Because the as-deposited EB-PVD coatings are oxygen deficient, both samples were annealed at 1000°C for 3 h in air. This helps to restore the crystallinity and remove compounds containing the hydroxy group that could be present and quench luminescence [123, 125, 165]. An artificial delamination was then created by Rockwell indentation on both samples. For sample A, a 2.45 kN load was applied normal to the surface and resulted in an observable spallation of the coating at the indentation spot and the delamination of the surrounding area of about 12 mm^2. This spherical indentation load resulted in a central impression spreading to a typical butterfly wing-like area that could be explained by anisotropic inelastic deformation of the substrate [17]. For sample B, a 1.96 kN load was applied and resulted in a lower lateral extent of delamination of the surrounding area, on about 7 mm^2. It can be noted that both delamination areas generated using Rockwell indentation were intended to replicate foreign-object damage and produced visible contrast to the naked eye, suggesting coating buckling with a micron-sized delamination width, as reported in literature [60].

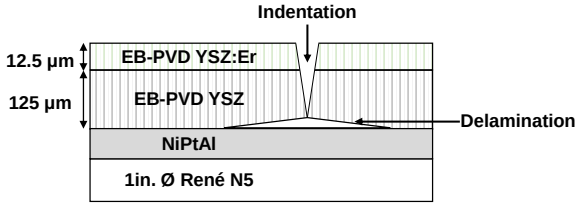

(a) Sample A, with doped layer at the top surface.

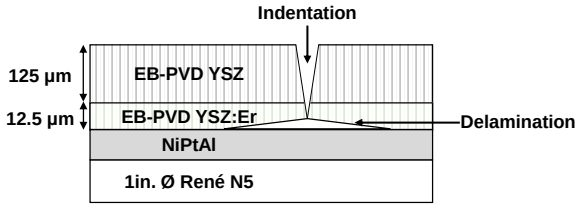

(b) Sample B, with doped layer at the bottom of the top coat.

Figure 40: TBC configurations that include a luminescent layer capable of detecting an underlying delamination zone.

Photoluminescence measurements

The spectral acquisition was done using a photoluminescence piezospectroscopy instrument [99] that uses a fiber collection spectrometer (Pixis 100, Princeton Instruments), under a 15 mW, 532 nm laser excitation. The probe has a focal length of 7.5 mm, a depth of field of 2.2 mm, a numerical aperture of 0.27, and a spot size of 200 μm. The probe is capable

of fast scanning over the surface of the sample by the means of an XYZ stage, as presented in Figure 41. This instrument has been successfully used for damage identification through piezospectroscopic stress evaluation using the R-line emission of α-Al_2O_3 [156, 62, 215, 81, 82, 83] and could potentially be used to obtain more comprehensive information such as spectral characteristics, intensity ratio or stress quantification based on comparison of rare-earth emission spectra over the probed area. This method is effective for thermal barrier coating stress characterization using luminescence from the thermally grown oxide (TGO) [230, 231, 86, 172, 107]. For this study, the wavelength range was adjusted to 540 - 580 nm to collect the Er-lines and the instrument was calibrated using a Hg lamp. The TBC samples were mounted on a vertical support and aligned normally to the laser beam. The spectral intensity was recorded over the surface of the samples with spatial step increments of 200 μm. The emission peak at 562 nm, corresponding to the transition $^4S_{3/2} \rightarrow {}^4I_{15/2}$ of erbium, was fitted using a pseudo-Voigt model and a linear baseline removal. For larger area measurements, other methods such as direct imaging with a bandpass filter could be more advantageous with faster data collection time.

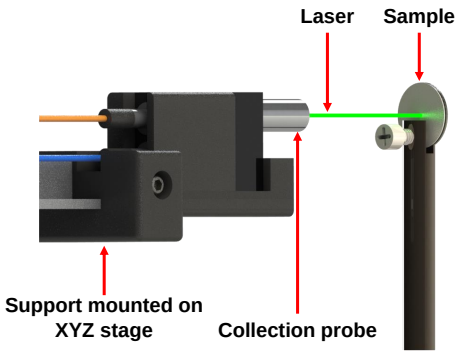

Figure 41: Measurement setup for delamination monitoring based on luminescence contrast.

Theory and calculation

The Kubelka-Munk model is a radiative transport model that can be applied to high scattering media for numerical estimation of light intensity distribution. In this work, it is applied to luminescent TBC layers for the evaluation of laser excitation and luminescence emission intensities, with the intent of quantifying delamination-induced luminescence contrast in TBCs. For a given incident laser excitation intensity on the top surface of the TBC, the luminescence intensity emerging out at the top surface and emitted from the sensing layer is calculated based on the diffuse internal reflectivity in the coating as well as the absorption and the scattering properties, taken at the specific excitation and emission wavelengths. Two model cases were evaluated in this work. The first approach considers simply a TBC top coat containing two layers (the sensing layer and the regular undoped layer). Two common assumptions were made to solve the model in this first case. On the one hand, the sensing layer, that contains very low levels of dopant, is assumed to have the same optical properties as standard undoped EB-PVD YSZ. On the other hand, the whole ceramic top coat is assumed to be isotropic. This simplification intends to provide good initial approximation. However, in reality, even low dopant concentration and agglomeration can result in a substantial modification of absorption and scattering properties [96]. Nonetheless, numerical estimations using the isotropic assumption are expected to be in good accordance with reality in relatively homogeneous microstructures, such as plasma spray coatings, as shown in literature [66, 216]. However, for EB-PVD coatings, the assumption on uniform scattering and absorption coefficients through the TBC thickness is problematic due to the waveguide-like scattering produced by the widening columnar

microstructure that forms from small equiaxed grains at the base of the top coat where scattering is expected to be much stronger than near the coating surface. Therefore, the second modeling case focuses on creating more accurate quantitative predictions incorporating three layers to account for the well-defined two-zone anisotropic microstructure of EB-PVD coatings [198, 9] as well as for the luminescent layer.
A schematic description of the Kubelka-Munk used for the first case study, including boundary conditions and definitions, is presented in Figure 42, where the doped layer is represented as a dotted area at the top of the TBC. In this modeling approach, light is traveling along the x-axis, corresponding to the normal to the surface of the TBC, in two opposite directions. The light vector component directed towards the bond coat is denoted by I and the light vector component directed back to the top surface of the TBC is denoted by J. The 2×2-flux model differentiates both excitation and emission wavelengths to solve for the laser (labeled ℓ) and luminescence (labeled $\mathcal{L}$) intensities separately. Similarly, the generalized absorption and scattering coefficients, K and S, respectively, are defined for a specific wavelength (labeled λ).

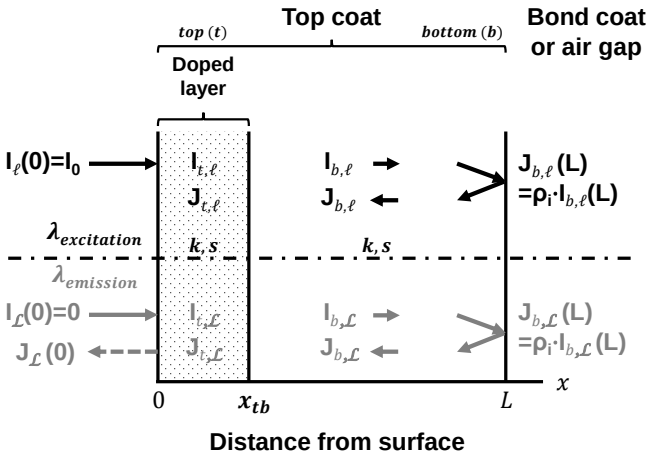

Figure 42: Kubelka-Munk first modeling approach and boundary conditions to model laser and luminescence intensities in isotropic TBCs.

The column vector $Y_\lambda(x) = [I_{t,\lambda}(x)J_{t,\lambda}(x)I_{b,\lambda}(x)J_{b,\lambda}(x)]^T$ defines radiation intensities and the matrix that determines optical properties in a specific layer z (top layer $z = t$ or bottom layer $z = b$) is given by:

$$A_{z,\lambda} = \begin{pmatrix} -(K_{z,\lambda} + S_{z,\lambda}) & S_{z,\lambda} \\ -S_{z,\lambda} & K_{z,\lambda} + S_{z,\lambda} \end{pmatrix}$$

Equation 16 is then used to solve for the intensity of laser light, as a function of the depth in the coating.

$$\frac{dY_\ell(x)}{dx} = \begin{pmatrix} A_{t,\ell} & 0 \\ 0 & A_{b,\ell} \end{pmatrix} \cdot Y_\ell(x) \tag{16}$$

The luminescence is assumed to occur exclusively due to the excitation of the sensing layer by the laser, which is given by I_ℓ or J_ℓ. The matrix that defines the amount of luminescence generated in a specific layer z is given by:

$$Q_z = \frac{1}{2}\begin{pmatrix} q_z K_{z,\ell} & q_z K_{z,\ell} \\ -q_z K_{z,\ell} & -q_z K_{z,\ell} \end{pmatrix}$$

where q_z is the quantum efficiency of the layer z. If the layer is luminescent, $q_z = 0.5$ [66], and if not then $q_z = 0$ (for example, for sample A, $q_t = 0.5$ and $q_b = 0$). Therefore, Equation 17 can be used to solve for the distribution of the luminescence intensities in the coatings.

$$\frac{dY_{\mathcal{L}}(x)}{dx} = \begin{pmatrix} A_{t,\mathcal{L}} & 0 \\ 0 & A_{b,\mathcal{L}} \end{pmatrix} \cdot Y_{\mathcal{L}}(x) + \begin{pmatrix} Q_t & 0 \\ 0 & Q_b \end{pmatrix} \cdot Y_{\ell}(x) \tag{17}$$

The second case study expands the complexity of the model by which considering three layers in the TBC top coat, as represented in Figure 43. At the base of the top coat, the shaded zone corresponds to the high scattering area, that is representative of EB-PVD microstructure.

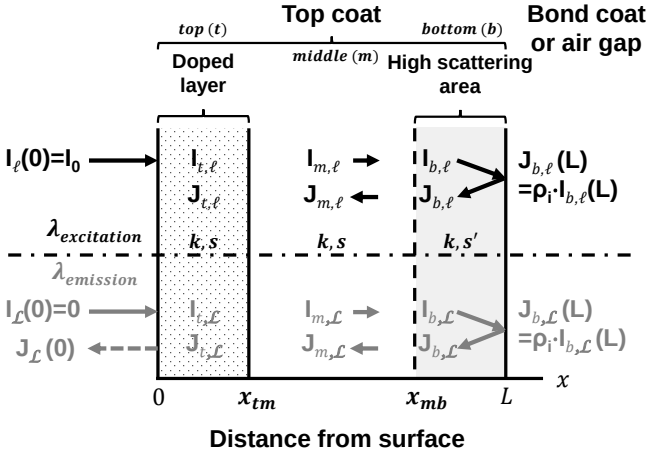

Figure 43: Kubelka-Munk second modeling approach to solve for laser (ℓ) and luminescence ($\mathcal{L}$) intensities, accounting for the high scattering zone, close to the bond coat in EB-PVD TBCs.

The column vector $Y_\lambda(x) = [I_{t,\lambda}(x) J_{t,\lambda}(x) I_{m,\lambda}(x) J_{m,\lambda}(x) I_{b,\lambda}(x) J_{b,\lambda}(x)]^T$ defines radiation intensities. Equations 18 and 19 are used to solve for the intensity of laser and luminescence lights, as a function of coating depth, respectively.

$$\frac{dY_{\ell}(x)}{dx} = \begin{pmatrix} A_{t,\ell} & 0 & 0 \\ 0 & A_{m,\ell} & 0 \\ 0 & 0 & A_{b,\ell} \end{pmatrix} \cdot Y_{\ell}(x) \tag{18}$$

$$\frac{dY_{\mathcal{L}}(x)}{dx} = \begin{pmatrix} A_{t,\mathcal{L}} & 0 & 0 \\ 0 & A_{m,\mathcal{L}} & 0 \\ 0 & 0 & A_{b,\mathcal{L}} \end{pmatrix} \cdot Y_{\mathcal{L}}(x) + \begin{pmatrix} Q_t & 0 & 0 \\ 0 & Q_m & 0 \\ 0 & 0 & Q_b \end{pmatrix} \cdot Y_{\ell}(x) \tag{19}$$

The generalized coefficients K and S that account for the bidirectional path of light are calculated from the absorption and scattering coefficients, respectively k and s, given in Table 12, and such that $K = 2k$ and $S = 2s$ (isotropic backscattering with no forward scattering) [228]. The high scattering area is characterized by stronger diffusion of light,

which can be simulated in this work using $s' > s$ and where k remains unchanged inside the entire TBC top coat. The thickness of the high scattering zone is fixed to 10 μm, based on reported values of microstructure [118, 235].

Table 12: Scattering and absorption coefficients [144, 240] of as-deposited EB-PVD YSZ from experimental data published in literature and considered at the wavelengths of interest for this study.

λ (nm)	Scattering coefficients s [s'] (m^{-1})	Absorption coefficient k (m^{-1})
532	12965 [46015]	407
562	12107 [39336]	319

The boundary conditions are defined such that, at the top surface, the percent intensity of the incident laser light is set to $I_\ell(x = 0) = I_0 = 100\%$ and there is no external luminescence input at the surface so that $I_\mathcal{L}(x = 0) = 0\%$. Depending on the interface type considered at the bottom of the top coat, either with an air gap (in the case of a delamination) or with the bond coat (for an intact coating), the reflectivity ρ_i is set to a specific value. For the case corresponding to delamination, Equation 20 defines the diffuse external reflectivity at the interface between the top coat and the air gap. This expression is obtained by applying the integrated average of the Fresnel equation [206, 211] and is used in Equation 21 to obtain the diffuse internal reflectivity ρ_i, at the interface between the top coat and the air gap, that is used as a boundary condition for the model.

$$\begin{aligned}\rho_0(n) =& \frac{1}{2} + \frac{(3n+1)\cdot(n-1)}{6\cdot(n+1)^2} + \frac{n^2\cdot(n^2-1)^2}{(n^2+1)^3}\cdot\ln(\frac{n-1}{n+1}) \\ &- \frac{2n^3\cdot(n^2+2n-1)}{(n^2+1)\cdot(n^4-1)} + \frac{8n^4\cdot(n^4+1)}{(n^2+1)\cdot(n^4-1)^2}\cdot\ln(n)\end{aligned} \tag{20}$$

$$\rho_{i,max}(n) = (1 - \frac{1}{n^2}) + \frac{\rho_0(n)}{n^2} \tag{21}$$

where ρ_0 is the diffuse external radiation at the interface between the top coat and the air gap, $\rho_{i,max}$ is the maximum diffuse internal reflectivity and $n = n_{YSZ}/n_{air}$ is the ratio of refractive indices (which must comply with the condition $n \geq 1$). The refractive index of EB-PVD YSZ is given in Table 13 and, by definition, $n_{air} = 1$. The value of reflectivity obtained at 532 nm is 82% and, at 562 nm, it is 83%, for the case of a delamination, for which the air gap width is assumed to be larger than the signal radiation wavelength which enables maximum reflectivity and discards frustrated reflectance. It can be noted here, although it is not investigated, that the formation of TGO at this location after aging of the TBC can contribute substantially to a change of reflectivity, estimated to be approximately 39% at the interface top coat/TGO (using Equations 20 and 21, with α-Al_2O_3 where $n_{TGO} = 1.76$) [142, 47].

Table 13: Refractive index of EB-PVD YSZ [241], considered at the wavelengths of interest for this study.

λ (nm)	n
532	2.17
562	2.16

The reflectivity for the interface between the top coat and the bond coat was estimated using the model for the frustrated angle-averaged reflectivity for radiation with angle of incidence greater than the critical incident angle θ_c ($\approx 27°$), which can be calculated using Equation 22 [60, 225, 226].

$$\overline{R}_f(d) = \frac{\int_0^{2\pi}\int_{\theta_c}^{\frac{\pi}{2}} \frac{\alpha\cdot\sinh^2(\beta\cdot d)}{1+\alpha\cdot\sinh^2(\beta\cdot d)}\cos\theta\cdot\sin\theta d\theta d\varphi}{\int_0^{2\pi}\int_{\theta_c}^{\frac{\pi}{2}}\cos\theta\cdot\sin\theta d\theta d\varphi} \tag{22}$$

where d is the air gap width formed through delamination, θ is the angle of incidence, φ is the azimuthal angle. α is given for a perpendicular polarization in Equation 23 and for a parallel polarization in Equation 24. β is given in Equation 25.

$$\alpha_\perp = \frac{(n^2-1)^2}{4n^2\cdot\cos^2\theta\cdot(n^2\sin^2\theta-1)} \tag{23}$$

$$\alpha_\parallel = \alpha_\perp\cdot(\sin^2\theta\cdot(n^2+1)-1) \tag{24}$$

$$\beta = \frac{2\pi}{\lambda_0}\sqrt{n^2\cdot\sin^2\theta-1} \tag{25}$$

where λ_0 is the radiation wavelength and $n = n_{YSZ}/n_{air}$. The frustrated angle-averaged reflectivity for unpolarized radiation is then found using Equation 26.

$$\overline{R}_{f,unp} = \frac{\overline{R}_{f,\perp}+\overline{R}_{f,\parallel}}{2} \tag{26}$$

where $\overline{R}_{f,\perp}$ and $\overline{R}_{f,\parallel}$ are the frustrated angle-averaged reflectivities for perpendicular and parallel polarized radiation, respectively, and can are calculated using $\alpha = \alpha_\perp$ and $\alpha = \alpha_\parallel$. Finally, the air gap width dependent diffuse internal reflectivity, that can be of particular interest for example for the examination of early stages of delamination, is obtained using Equation 27.

$$\rho_i(d) = \overline{R}_{f,unp}(d)\cdot(1-\frac{1}{n^2}) + \frac{\rho_0(n)}{n^2} \tag{27}$$

The numerical value of the reflectivity at the interface between the top coat and the bond coat was obtained using Equation 27 and taking the limit as d goes to 0. The reflectivity was found to be approximately 4% at 532 and 562 nm wavelengths.

Delamination monitoring results

The intensity maps of the samples are presented in Figure 44. In both cases, delamination areas can be detected easily due to much larger sharp increases in luminescence intensity than in the increase in reflectance observed by the naked eye. The TBC coatings also show some defects that can be detected with this method as they are associated with a luminescence intensity that is significantly lower than the one collected in an intact zone of the coating. For sample A, for example, distinct locations close to the indent area have top surface markings (contamination) causing local reduction of emission intensity. Furthermore, spallation results in zero luminescence and can be seen in gray on the intensity map. Other factors that are not considered in this study but which can affect measurements include irregularities of coating thickness, concentration variation and dispersion inhomogeneity of the luminescent ions in the material concentration, curvature of the TBC along

the turbine blades, partial erosion, sand glazing or calcia-magnesia-alumina-silicate surface deposition. These elements contribute to luminescence intensity inconsistencies or surface coating opacity in localized areas [92], which point towards inevitable challenges for practical online implementation. For sample A, it can be seen that, although the sensing layer is not in direct contact with the bond coat, the drastic increase of diffuse internal reflectivity at the bottom of the ceramic top coat that is associated with a debonding at the interface between top coat and bond coat produces a noticeable increase of luminescence intensity. For sample B, on the other hand, even though the indentation load was modestly lower than that of sample A, generating smaller lateral delamination expansion, a considerable contrast was observed, indicating particular effectiveness of luminescence-based measurements for this layer configuration. These luminescence intensity contrasts are due to the increased reflection of the laser and luminescence lights at the interface between the top coat and the bond coat in presence of an air gap, providing more excitation to the sensing layer and more reflected luminescence to emerge out of the TBC surface. It can be noted in both samples that the indentation location shows a reduced luminescence intensity due to the possible compaction of the sensing layer. Moreover, for both samples, there is enough luminescence intensity contrast for fast delamination detection, which is promising for the application of this technique using any multilayered configuration. However, for the application of this method for delamination detection on curved surfaces, luminescence intensity gradients are expected and configurations like sample B with high luminescence intensity contrast will be preferred.

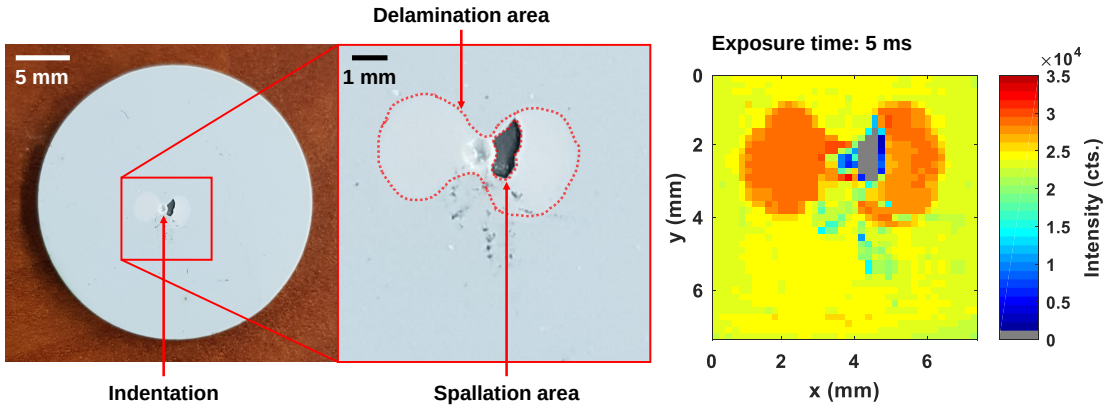

(a) Sample A, with doped layer at the top surface.

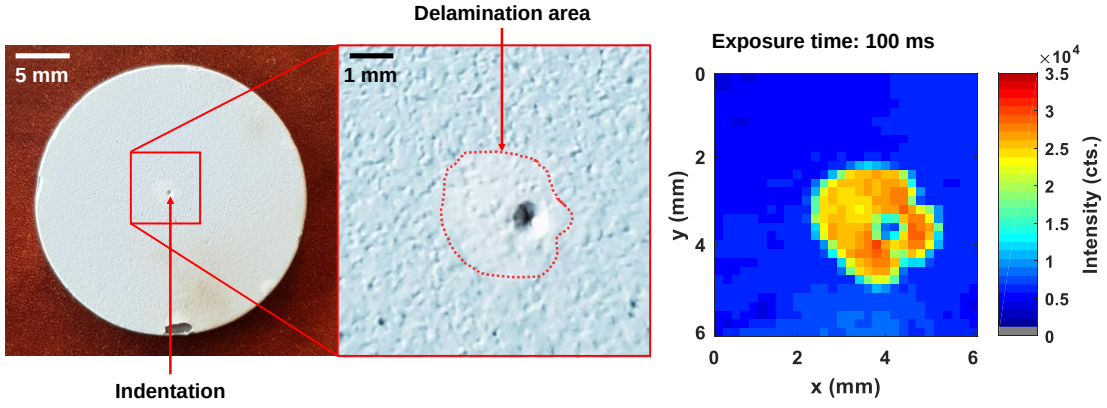

(b) Sample B, with doped layer at the bottom of the top coat.

Figure 44: Photograph of the coatings with Rockwell indentation-induced delamination or spallation areas and corresponding luminescence intensity maps of the Er-line at 562 nm.

The solutions obtained by the Kubelka-Munk model for the first case study where only two layers are considered (sensing layer and regular layer) provide the distribution of light intensities. At any point in the coating, the intensities I and J for laser (ℓ) and luminescence ($\mathcal{L}$) are calculated based on absorption, scattering and interface reflectivity. The results for the laser intensity are presented in Figure 45. It can be noted that, in the presence of a delamination (case presented in red), there is a significant difference in the intensity of light traveling back to the top surface (J_ℓ). The additional excitation intensity in the doped layer, particularly enhanced in regions closer to the interface between the top coat and the bond coat, contributes to the higher intensity of luminescence produced in the sensing layer. For sample A, in the doped layer, the increase of the intensity of the backscattered laser radiation J_ℓ contributes almost exclusively to the gain in excitation intensity that is available for the production of luminescence, in the case of delamination. For sample B, in the doped layer, the summation of the integrated intensities of the incoming laser radiation I_ℓ and the backscattered laser radiation J_ℓ is drastically increased in the presence of a delamination, largely contributing to the higher intensity of luminescence. The results of the model for the luminescence intensities for samples A and B are presented in Figure 46 and 47, respectively, and the dotted areas represent the location of the doped layer. It can be seen that there is an overall increase of luminescence intensity when a delamination is present. This is due to both higher amount of laser excitation energy available, as de-

scribed above, and greater reflection of the luminescence radiation itself, at the bottom of the top coat.

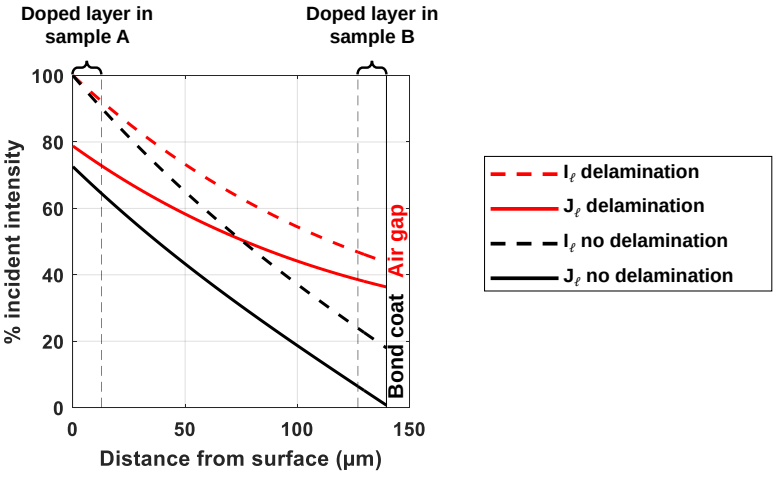

Figure 45: Distribution of laser intensity in the two-layer model. In the case where there is delamination, higher intensities are scattered back due to increased reflectivity. The location of the doped layer for samples A and B is represented on the same figure.

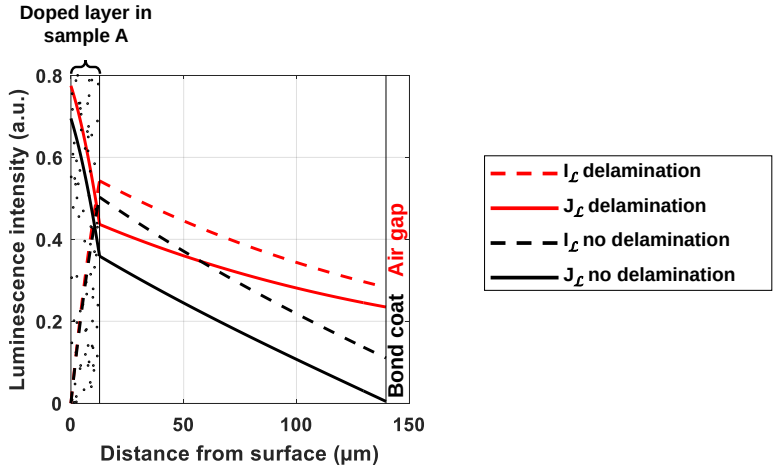

Figure 46: Distribution of luminescence intensity in the two-layer model for sample A: doped layer on top.

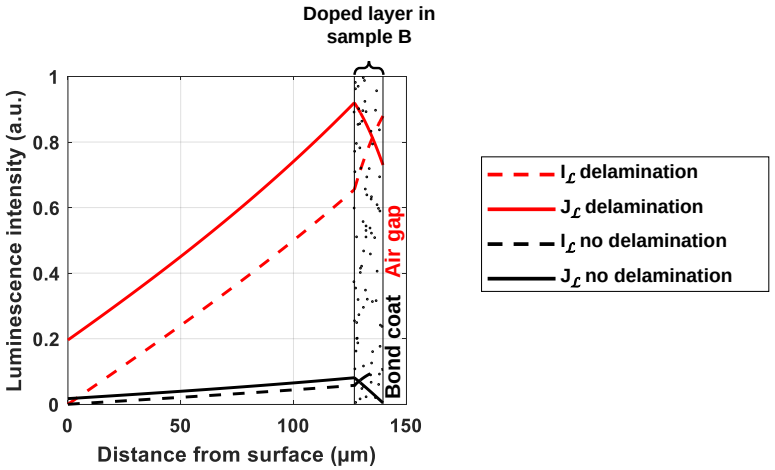

Figure 47: Distribution of luminescence intensity in the two-layer model for sample B: doped layer at bottom of top coat.

The three-layer model is an improvement of the two-layer model as it integrates a high scattering layer located at the base of the top coat, with the set of distinct optical properties discussed previously, and as observed on typical EB-PVD microstructures. This modeling approach is expected to produce more accurate results in comparison with the two-layer model since it captures the differences in optical properties associated with the evolving microstructure of EB-PVD coatings with depth. The solutions obtained in this second case study provide the distribution of laser intensity, as shown in Figure 48. The results for the luminescence intensities for samples A and B are presented in Figure 49 and 50, respectively.

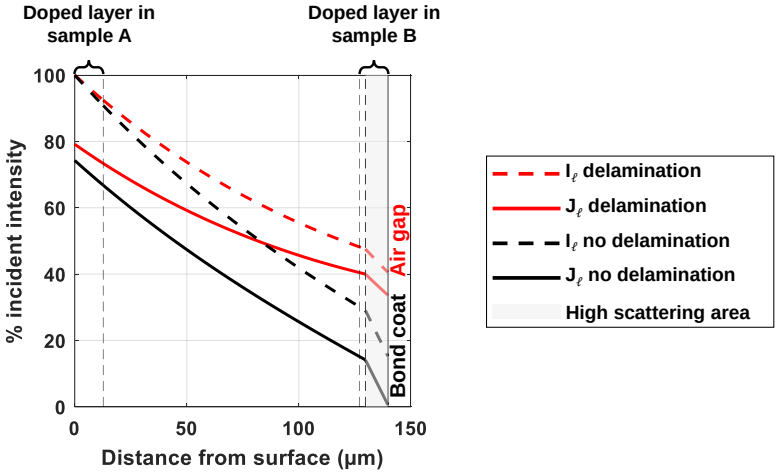

Figure 48: Distribution of laser intensity in the three-layer model. In the case where there is delamination, higher intensities are scattered back due to increased reflectivity. The location of the doped layer for samples A and B is represented on the same figure.

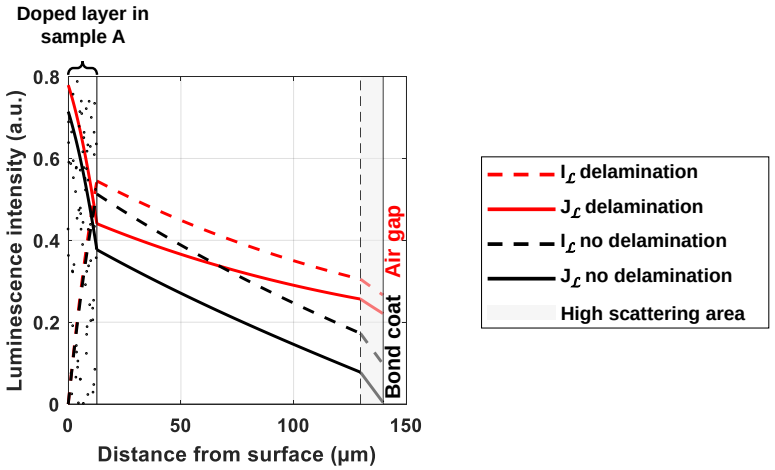

Figure 49: Distribution of luminescence intensity in the three-layer model for sample A: doped layer on top.

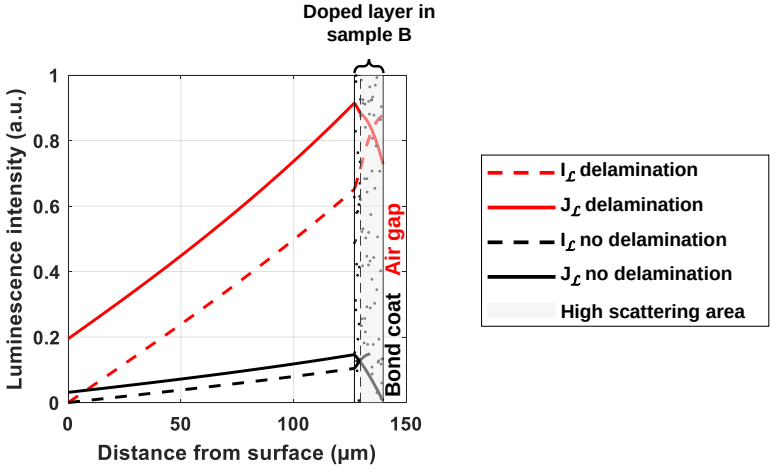

Figure 50: Distribution of luminescence intensity in the three-layer model for sample B: doped layer at bottom of top coat.

The sensitivity to layer thickness variations that exist in practice is taken into account for the calculation of the standard deviation error on the model results for the calculation of $J_{\mathcal{L}}(x = 0)$, which represents the measurable luminescence intensity that is emerging from the top surface and that can be collected by a detector. The numerical values found for $J_{\mathcal{L}}(x = 0)$ are reported in Table 14. Generally, the EB-PVD technique leads to good control on the thickness of the deposited coatings, with a precision that can be as low as 1 μm [199, 190]. Assuming that the overall top coat thickness remains constant (137.5 μm), the model was solved for a sensing layer thickness of 12.5 $\pm$ 1 μm.

Table 14: Results of the Kubelka-Munk model for the predicted luminescence intensity emerging out at the surface.

Intensity (a.u.)	Sample A	Sample B
Two-layer model		
$J_{\mathcal{L}}(x=0)$ delamination	0.764 ± 0.057	0.198 ± 0.017
$J_{\mathcal{L}}(x=0)$ no delamination	0.683 ± 0.049	0.017 ± 0.003
Three-layer model		
$J_{\mathcal{L}}(x=0)$ delamination	0.768 ± 0.057	0.196 ± 0.019
$J_{\mathcal{L}}(x=0)$ no delamination	0.703 ± 0.052	0.031 ± 0.005

Table 15 allows for direct comparison of modeling and experimental results. The luminescence intensity contrast (or enhancement factor η) between a delamination area and an intact coating area was obtained in models by juxtaposition of the two extreme cases of diffuse internal reflectivity (4% for intact coating and 82-83% in the presence of a delamination area). The error shown in the Kubelka-Munk models accounts for typical thickness variation, as defined previously. Experimentally, the enhancement factor η was obtained dividing the average of 10 measurements in the delamination area by the average of 10 measurements outside this area and the reported error corresponds to the standard deviation over these points.

Table 15: Modeling and experimental results for the ratio of delamination over intact coating luminescence intensities.

Enhancement factor η	Sample A	Sample B
Two-layer model	1.12 ± 0.16	11.36 ± 2.98
Three-layer model	1.09 ± 0.16	6.32 ± 1.63
Experimental measurement	1.17 ± 0.02	4.82 ± 0.47

The comparison indicates that, as expected, the three-layer model better correlates with experimental measurements. For sample A, the enhancement factor η that was obtained from both modeling approaches is close to the experimental result. However, for sample B, the two-layer model predicts an enhancement factor well above the actual experimental results, which indicates that the sensing layer of sample B actually presents a different (stronger) scattering behavior when compared to the rest of the TBC, making the assumption on the isotropy limited for accurate predictions in such sensing layer configurations. Because much of the contrast is produced by multiple scattering events (both laser and luminescence) in the sensing layer, the larger mismatch with the prediction is expected for sample B. The three-layer model that accounts for this high scattering at the base of the TBC (in this case it also corresponds to the base of the sensing layer) generates a more accurate estimation and validates this modeling approach for EB-PVD coatings. Figure 51 better shows the comparison between models prediction accuracy and experiment where the three-layer model is particularly appropriate for estimations on TBC layer arragement as found in sample B.

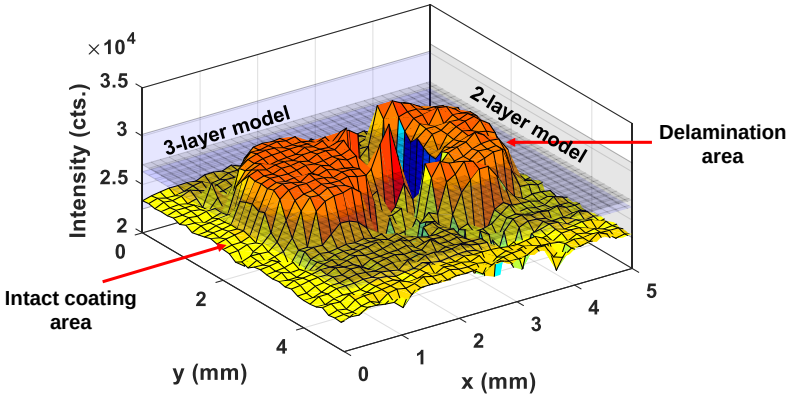

(a) Sample A, with doped layer at the top surface.

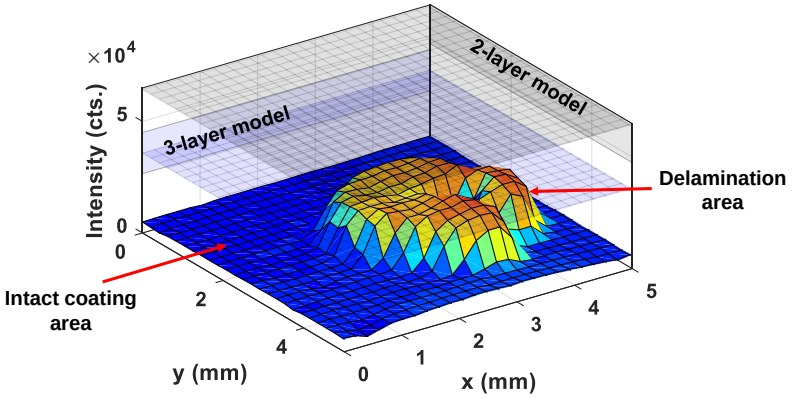

(b) Sample B, with doped layer at the bottom of the top coat.

Figure 51: Comparison of experimental measurements (colored surface) with modeling predictions for delamination area intensity. Error bar for each model is represented on a wall.

The Kubelka-Munk models presented in this work help to characterize the progression of coating delamination. The coating health can be monitored measuring luminescence intensity over extended areas. The locations where luminescence contrast exceeds the lower boundary of the enhancement factor predicted by the models indicate delamination zones. It must be noted that assumptions and simplifications on the Kubelka-Munk models as well as the accuracy of the coefficients selected for the material can contribute to discrepancies between model estimations and reality.

The evaluation of luminescence enhancement factor and signal intensity trade-offs clearly showed that having the sensor layer on the bottom of the TBC, as found in sample B, is preferable for delamination monitoring. Although this location is intuitive, the approach presented in this work is uniquely powerful for optimizing the thickness of the sensing layer at the bottom of the TBC. Figure 52 provides the signal trade-offs for 137.5 μm EB-PVD TBC configurations containing a luminescent layer with varying topology (the position axis indicates the location of the top of the sensing layer embedded in the TBC), accounting for the high scattering zone at the base of the coating (10 μm), as given in the three-layer model. The enhancement factor η corresponds to the achievable luminescence contrast generated in the presence of a delamination, and confirming that very thin sensing layers located at the bottom of the top coat (such as for sample B) are more ideal when looking for maximum contrast for detection. Luminescence intensities are normalized to allow for direct intensity comparisons between distinct layer configurations while being cau-

tious and avoiding inaccurate numerical estimations that could originate from the inherent uncertainty on quantum efficiency. A thicker sensing layer would provide more intensity, but with some contrast loss (less contrast from portions of the sensing layer farther from the interface). Additionally, although sample configurations with a sensing layer at the top surface provide high luminescence intensities, they are vulnerable to erosion. This can however be used to our advantage to monitor erosion using the luminescence-based modeling method presented in this work. A configuration that might be of interest for multi-purpose detection capabilities could be the fully doped coating, with the highest luminescence intensity and higher contrast than the other configurations with sensing layer placed on top of a regular coating (as for sample A). Finally, the effects of frustrated total internal reflectance that occurs for air gaps smaller than the radiation wavelength can be later studied using this approach. Indeed, the substantial variations of diffuse internal reflectivity can be used for the characterization of the early stages of delamination during formation of air gaps. Similarly, TGO growth and location of delamination with respect to this oxide layer can be evaluated using the models presented in this work.

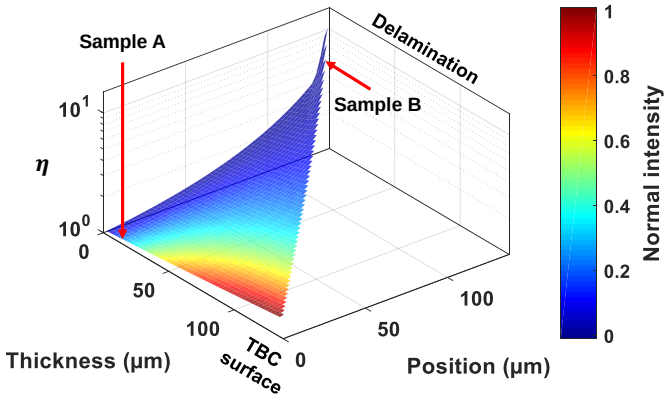

Figure 52: Modeled signal trade-offs for an EB-PVD TBC containing an embedded sensing layer.

A promising modeling approach was developed to enhance the understanding of the factors underlying TBC delamination using the contrast provided by luminescence measurements. In particular, this study presents an improved fundamental framework for evaluating the trade-offs between luminescence signal strength and delamination contrast that can be used to optimize doped layer coating configurations. Specifically, two-layer (sensing layer and regular layer) and three-layer (with high scattering area integrated to the previous case) Kubelka-Munk models were formulated to predict, for any TBC configuration that embeds a luminescent layer, the luminescence intensity contrast which can be used to effectively quantify and monitor delamination areas in TBCs. Modeling results were compared to experimental values that were collected on two as-deposited EB-PVD TBCs which each contain an erbium-doped YSZ layer for delamination sensing. An artificial delamination zone created by Rockwell indentation was successfully quantified by measuring the intensity of the erbium emission at 562 nm over the surface of the coatings. The luminescence contrast predicted by the three-layer model was found to be in good accordance with experiments, emphasizing the importance of considering the microstructure anisotropy in EB-PVD TBCs for accurate delamination characterization. This modeling approach is very promising for the determination of signal trade-offs for layer topology optimization.

Task 5: Lab scale instrumentation development

Thermal barrier coatings are widely used in turbine systems to protect the components operating at high temperatures. They are generally used in combination with active cooling systems that allow for temperature drops through the ceramic top coat, in the order of 1°C/μm [45, 238]. Accurate measurement of coating temperatures in such extreme environments is crucial to ensure and maintain good performance, functionality of the system, and predictions on the lifetime of the turbine blades. The temperature measurement uncertainty has to be reduced to a few degrees at service temperatures as failure mechanisms are thermally driven. This is particularly important due to the extreme sensitivity of the growth rate of the Thermally Grown Oxide to the temperature at the interface between top coat and bond coat [35]. Currently, the viable techniques for non-contact *in-situ* temperature measurements are infrared thermometry, for which precision is limited by the presence of emissions from the operation of the turbine engines as well as emissivity variation, and phosphor thermometry, that shows potential as a reliable method for precision temperature measurements [69, 41]. Phosphor thermometry has proven to be effective at high temperatures using rare-earth or transition metal doped ceramics that can be embedded into TBC configurations to enable real-time temperature monitoring in service conditions [7, 54, 68, 111, 93, 33]. Among the possible sensors for high temperature measurements integrated into TBCs, rare-earth doped Yttria-Stabilized Zirconia (YSZ:RE) have been largely studied as they offer sensing capabilities with ease of integration in existing standard TBCs and no layer compatibility mismatches. Particularly, europium-doped YSZ (YSZ:Eu^{3+}) has been extensively selected as it has excellent temperature sensitivity past its quenching temperature of about 500°C [168] and an intense visible luminescence with a long room temperature decay time [55, 30]. Similarly, erbium doped YSZ (YSZ:Er^{3+}) has a strong visible luminescence intensity [60]. It has a shorter room temperature decay time and a temperature sensitivity on the entire range between room temperature and turbine operating temperatures [202]. Having a usable absorption band at 532 nm [11] and distinct emission wavelengths, both dopants can be used together in a co-doped configuration that possesses their combined properties. The two dopants have been used together in literature in a YSZ host for multi-layer rainbow sensors [88], thermal history sensors [11, 42], and in Y_2O_3 for intensity ratio measurements [182].

In this work, instrumentation was developed so that the luminescence produced by YSZ:Er^{3+} and YSZ:Eu^{3+} could be isolated and simultaneously collected with the objective of doubling the data for higher precision, combining sensitivities of the dopants and extending the temperature range at which the instrument can measure *in-situ* temperature on rare-earth doped YSZ TBCs. The decay and intensity ratio methods were used jointly, as reported in literature [84, 24], to take advantage of the synchronized collection of two dopants. The sample contains the sensing layer at its top surface so the phosphor thermometry measurement can be compared with infrared thermometry. Additionally, this configuration allows for the strongest luminescence intensity to emerge out of the sample [75].

Phosphor thermometry laser source and detector

An advanced phosphor thermometry system was designed and built up in this task to measure the luminescence lifetime decay on sensor thermal barrier coatings. The pulsed laser is an Nd-YAG 1064 nm laser with 1-10 Hz repetition rate. Energy output of the 1064 nm pulsed laser is 1 mJ. A series of crystals were used for second and third harmonic generation. Specifically, a potassium titanyl phosphate (KTP) crystal was used to convert the 1064 nm wavelength into a combination of 1064 nm and 532 nm wavelengths. A lithium triborate (LBO) crystal was used to generate 355 nm wavelength. The wavelegnth to be used in practice for laser excitation is to be determined later based on the phosphor of

interest. Schematic of the doubling and the tripling method is presented in Figure 53.

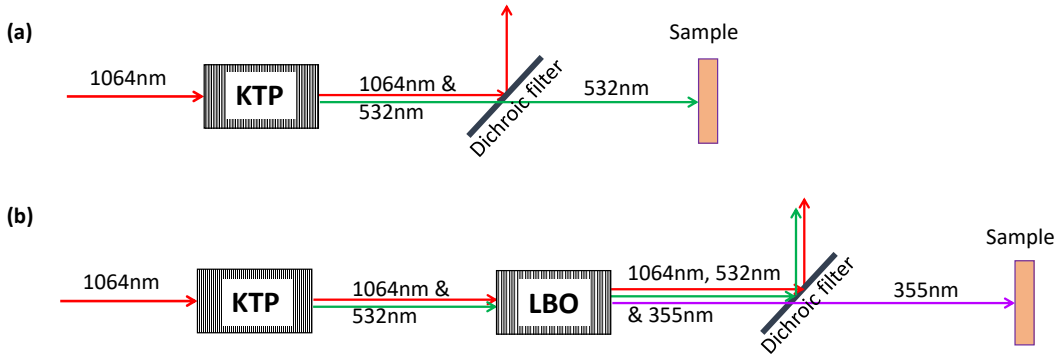

Figure 53: Schematic of (a) Doubling method and (b) Tripling method

A six-stage photomultiplier tube (PMT) is used to detect the luminescence emission. Low signal from the emission is amplified using the PMT and the gain can be adjusted by changing the voltage input of the PMT. The PMT typically detects emission from a surface area of about 0.5×0.5 cm^2. Additional PMTs were added to the phosphor thermometry instrument setup to enable simultaneous multi-wavelength characterization.

Initial testing and calibration of the instrument using alumina

Alumina was used as a reference for calibration and to ensure proper collection of luminescence decay using the initial phosphor thermometry instrument prototype. The instrument was tested using the well known R-line (ruby) emitted from an alumina block under a 532 nm excitation pulse. This experiment was performed at room temperature and using a 694.3 nm bandpass (10 nm FWHM - Thorlabs) for the specific collection of the R1-line decay. A cyan dichroic filter (FD1C - Thorlabs) was used to transmit the laser beam to the sample and to reflect the luminescence signal to the detector. The resulting decay was fitted using a single-exponential model and is presented in Figure 54. The obtained decay is comparable to values found in literature [32, 200].

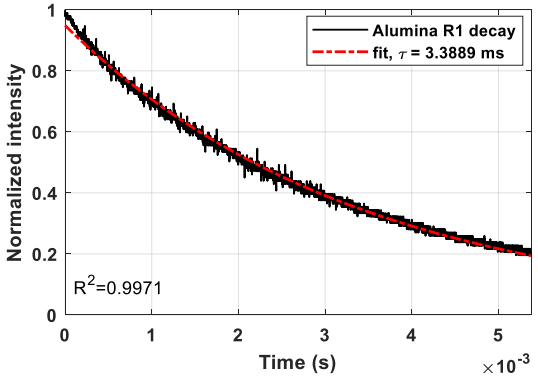

Figure 54: Room temperature decay of the R1-line of alumina.

The alumina sample was then placed in an infrared (IR) heater to get initial temperature-decya correlations. The setup with the heater is presented in Figure 55. The first instrument prototype for these measurements was assembled on a cart for portability and for

easy integration to the sample environment (in particular to be adjustable in height). The setup is shown in Figure 57. The PMT was aligned in height with the sample using a scissor lift platform and the excitation laser was redirected using fast response laser mirrors that reflect the 10 ns laser pulses.

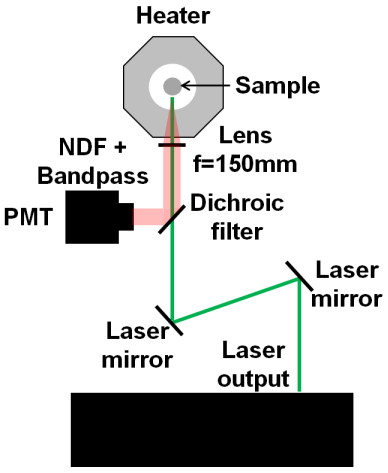

Figure 55: Phosphor thermometry setup for measurements on alumina (Al_2O_3:Cr) using the IR furnace

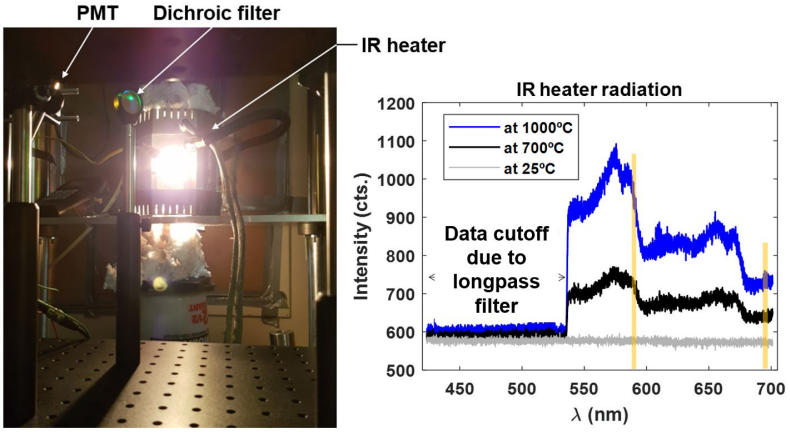

Figure 56: Phosphor thermometry system combined with IR heater for high temperature measurements.

For the luminescence decay measurements using the heater, the maximum temperature at which we were able to collect signal was approximately 306^{o}C. Past this point, the strong visible light noise emitted by the IR incandescant lamps prevent from capturing decays. The actual spectrum of the lamps was collected using a Pixis 100 spectrometer in the visible range and is presented in Figure 56. A longpass in the spectrometer probe cuts off the spectrum portion with wavelengths smaller than 532 nm. The two bandpass filter configurations used typically for phosphor thermometry measurements on alumina (694.3 nm +/-10 nm FWHM, Thorlabs) and YSZ:Eu (600 nm +/-40 nm FWHM, Thorlabs + 580 nm +/-10 nm FWHM, Thorlabs) are represented in yellow. It can be seen that a non-neglgible radiation directly coming from the heater lamps affects data collection at these wavelengths.

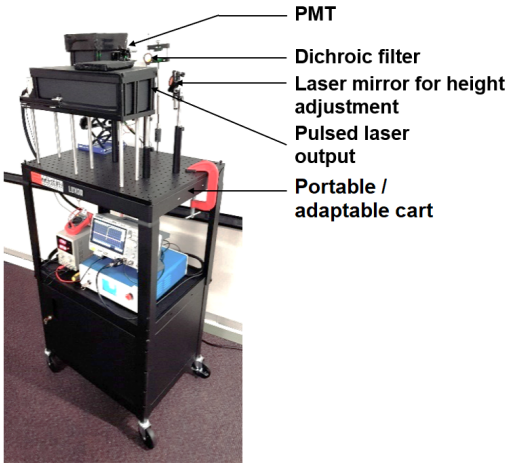

Figure 57: Phosphor thermometry system (first prototype).

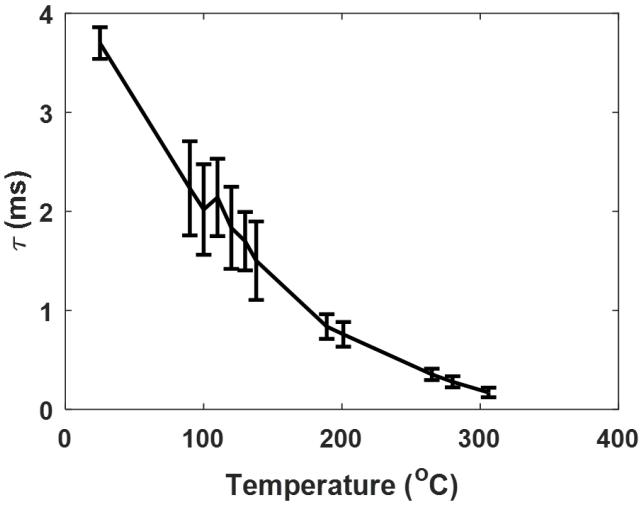

Figure 58: Initial temperature-decay curve obtained for alumina.

Fabrication of temperature sensor TBCs for the demonstration of the instrumentation

The main sample configuration for Task 5 allowed to characterize two dopants (Er and Eu) and to demonstrate an innovative phosphor thermometry setup. This sample configuration was fabricated using an SG-100 (Praxair) spray gun at the Air Plasma Spray (APS) facility of the Florida Institute of Technology. The materials and parameters used for the deposition of the layered configuration are given in Table 16. The substrate is a 25.4 mm diameter and 3 mm thickness CM247 disk. The sample was grit blasted prior to the deposition of the bond coat layer. A stud was welded on the back of the substrate to mount the sample on the deposition stage. NiCrAlY bond coat powder (NI-164/NI-211, Praxair), 7-8 wt.% YSZ undoped top coat powder (ZRO-271, Praxair) and erbium and europium doped YSZ top coat powders (produced by solid state reaction by Phosphor Technology Ltd.) were used for the deposition of the layers, as shown in Figure 59(a). The erbium concentration of 1.5 wt.% in YSZ was chosen for optimal luminescence intensity, based on literature [88]. The europium concentration of 3 wt.% was chosen for high luminescence intensity and limited dopant intrusiveness to prevent from phase change [213]. As the preprocessing doped YSZ powders that we got had a small particle size (D_{50}10 μm, which is

too small for APS deposition) and irregular particle shapes, they were mixed together with state-of-the-art sprayable undoped YSZ powder to ensure the flowability of the mixture and a good deposition rate for the uppermost layer. The feeding wheel speed was decreased to get a constant deposition rate with reduced clogging probability of the APS system. It was found that a mixing ratio of 1:2 for the doped powder in undoped powder was optimal to get a good deposition rate while keeping sufficient doped material for luminescence intensity. The fabricated TBC sample was examined using scanning electron microscopy, as presented in Figure 59(b), with secondary electrons and an accelerating voltage of 15 kV. The uninterrupted and successive deposition of undoped and doped YSZ layers ensured the uniformity of the overall top coat with no visible interface. The sample was annealed 2 h at 800°C to remove potentially present luminescence quenching compounds.

Table 16: Materials and parameters for the Air Plasma Spray deposition.

Layer	Bond coat	Undoped top coat	Doped top coat
Material (Mixing percentages given in wt. %)	NiCrAlY	YSZ	66% YSZ + 17% YSZ:Er (1.5% Er) + 17% YSZ:Eu (3% Eu)
Thickness (μm)	150	250	80
Spray distance (cm)	10	7.5	7.5
Current (A)	802	902	902
Voltage (V)	43.3	43.7	43.7
Argon (SLM)	49.1	25.5	25.5
Helium (SLM)	20.3	20.8	20.8
Feeding wheel speed (rpm)	1.17	3.29	0.48

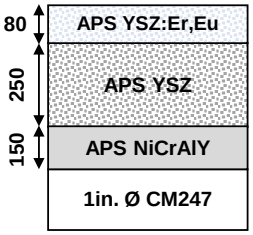

(a) TBC sample layer configuration. Units in μm.

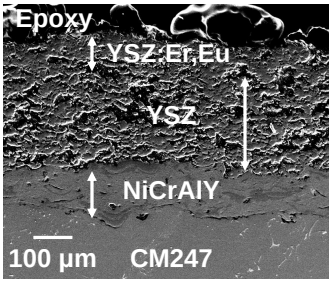

(b) TBC sample microstructure.

Figure 59: APS TBC configuration including a luminescent layer of YSZ:Er,Eu.

Spectral characterization of the sample

The emission spectrum of the YSZ:Er,Eu sample was measured with a collection time of 1 ms using a fiber collection spectrometer (Pixis 100, Princeton Instruments) under a 15 mW 532 nm laser excitation. The probe has a focal length of 7.5 mm, a depth of field of 2.2 mm, a numerical aperture of 0.27, and a spot size of 200 μm. The Er-lines at 545 nm and 562 nm and the Eu-lines at 590 nm and 606 nm were observed. The co-doping might introduce some level of re-absorption of the erbium-lines due to the presence of europium that possesses an absorption band that excites the $^5D_1$ level and that extends from 520 to 550 nm [55, 32]. This could ultimately result in a smaller intensity ratio between erbium and europium. For this study, the peak of erbium at 545 nm ($^4S_{3/2} \rightarrow {}^4I_{15/2}$) and the

peak of europium at 590 nm ($^5D_0 \rightarrow {}^7F_1$) were chosen for luminescence intensity and decay measurements. Figure 60 shows the emission spectrum of the YSZ:Er,Eu sample, highlighting the two regions that were collected by the phosphor thermometry detectors.

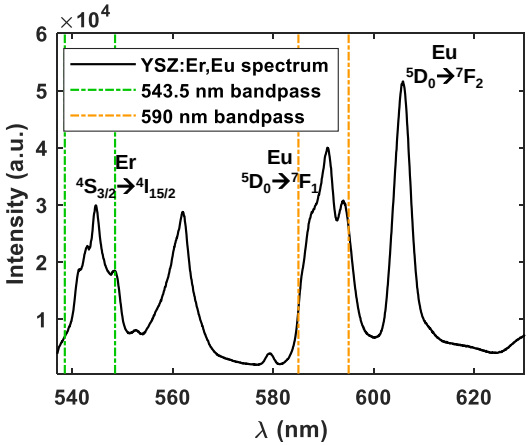

Figure 60: Emission spectrum of YSZ:Er,Eu under 532 nm laser excitation. The full width at half maximum of the bandpasses is represented to indicate the range of wavelength collected for the luminescence measurements.

Phosphor thermometry system characteristics (second prototype with two PMTs)

The phosphor thermometry system that is presented in Figure 61, was constructed so it is adaptable to any temperature sensor that has at least two emission peaks that can be isolated by means of dichroic filters. The instrument was also made portable by setting up the system on a stable cart for which the height can be adjusted by either lifting the top surface of the cart or lifting individually the photomultiplier tubes (PMTs) as they are mounted on precision lab lift jacks, fixed on the main optical breadboard. The PMTs are two Hamamatsu R3896 powered by a single precision direct current power supply providing 15 V and a maximum current of 90 mA for each detector. The maximum internal resistance of the gain control module of each PMT was measured to be around 80 kΩ.

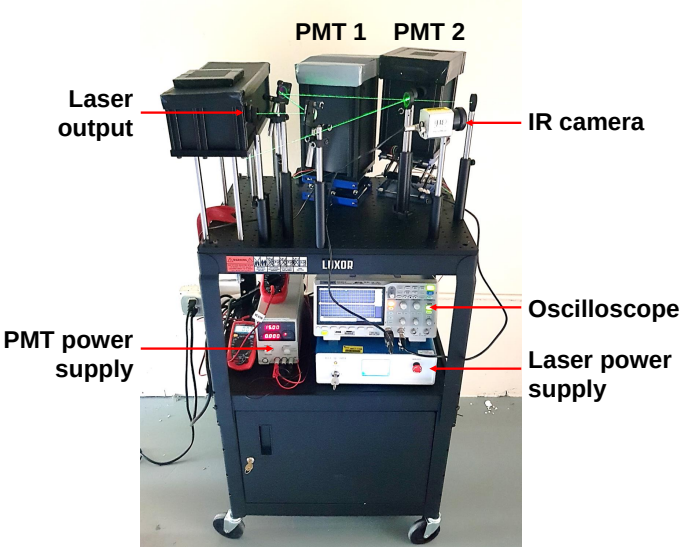

Figure 61: Overall view of the phosphor thermometry instrumentation.

For this experiment, the 532 nm excitation was chosen and the 355 nm was stopped with a beam blocker. A couple of laser mirrors were used to adjust the direction of the beam to the sample. After the laser beam was correctly aligned in the axis of the sample, a cyan dichroic filter (FD1C - Thorlabs) was placed in the path of the beam so the angle of incidence (AOI) is 30°. This value was chosen as it lowers the reflection of the laser light on the dichroic filter and allows for a higher excitation intensity onto the sample. A magenta dichroic filter (FD1M - Thorlabs) was then placed with an angle of incidence of 45° from the axis of reflection of the cyan dichroic filter. This allowed the convoluted luminescence of the co-doped sample that was reflected on the cyan dichroic filter to be further split into two spectral bands. The shorter wavelengths containing the erbium emissions were reflected on the magenta dichroic filter and directed to PMT 1, located in the axis of reflection of the magenta dichroic filter. On the other hand, the longer wavelengths containing the europium emissions were transmitted through the magenta dichroic filter to PMT 2, located in the axis of reflection of the cyan dichroic filter. The distance from the cyan dichroic filter to the sample was approximately 30 cm and the distance between the two dichroic filters was approximately 8 cm. For the collection of the decays, the two PMTs were used simultaneously. On PMT 1, connected to the channel 1 of the oscilloscope, a 543.5 nm (10 nm FWHM - Thorlabs) bandpass was placed in the viewing port of the detector. Because the wavelengths of the erbium emission at 545 nm and the excitation at 532 nm are close to each other, some laser leakage occurred due to laser reflections passing though the bandpass which has a transmission and optical density at 532 nm of 0.19% and 2.73, respectively. As the laser intensity is very high in comparison with the luminescence intensity, to better protect the PMT and avoid the undesired collection of laser light, a longpass filter with an optical density of 5 on the 190-532 nm range was added. On PMT 2, connected to the channel 2 of the oscilloscope, a 590 nm (10 nm FWHM - Thorlabs) was mounted in the viewing port. To avoid direct exposition to intense laser reflections, prevent from the collection of external light, and capture exclusively light traveling through the optical components of the instrument, a laser barrier panel was placed in front of the instrument. A viewing hole was extruded to insert an iris, opened to its maximum aperture (25 mm) and a 125 mm convex lens, that converges the slightly divergent laser beam onto the sample. This arrangement results in a spot size of about 4 mm on the surface of the sample, placed at the focal distance of the convex lens, and allows for the collimation of the luminescence light traveling to the detectors. The optical setup that was assembled for this study is presented in Figure 62.

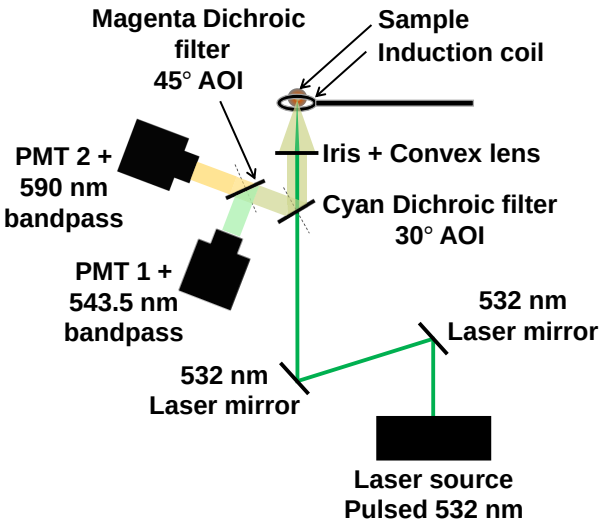

Figure 62: Phosphor thermometry instrumentation for synchronized monitoring of luminescence from YSZ:Er,Eu.

High temperature setup

We determined earlier that measuring decays in an IR heater environment does not yield sufficient temperature range. For this study, high temperature was achieved via induction heating (RDO HU2000), that produces the high frequency pulsating of magnetic fields to induce internal eddy currents in the material. These eddy currents begin to circulate, causing resistive heating within the material [46]. A frequency of 272 kHz and lift off distance of 5 mm was used between the induction coil and the surface of the sample, as shown in Figure 63(a). The resistive heating Q, generated by the internal eddy currents can be described by Equation 28:

$$Q = \frac{1}{\sigma} \cdot \mid J_s \mid^2 \tag{28}$$

Where σ is equal to electrical conductivity and J_s is the eddy current density generated by the magnetic field. In order to keep the sample surface parallel to the induction coil and normal to the horizontal path of the laser beam, a circular segment of the disk was cut off so the sample can stand on refractory blocks, as shown in Figure 63(b). Temperature increments of 50°C were achieved up to 1100°C through increasing the power of the inducting system and phosphor thermometry data was collected at each temperature step. Induction heating was chosen for this study as it does not produce background thermal radiation which facilitates luminescence measurements.

Control of the temperature using infrared thermometry

The temperature was measured using a TIM450 (Micro-Epsilon) longwave infrared camera (7-13 μm) operating at 30 Hz and placed at 20 cm from the sample, which corresponds to the focal distance of the camera. The collection area was reduced to match the phosphor thermometry laser spot size. The camera uses the program TIM Connect to track the thermal radiation emitted from the sample. The emissivity was set to $\epsilon = 0.95$ for all readings as this value corresponds to the emissivity of YSZ in the longwave infrared range and does not vary noticeably with temperature [94, 158, 153].

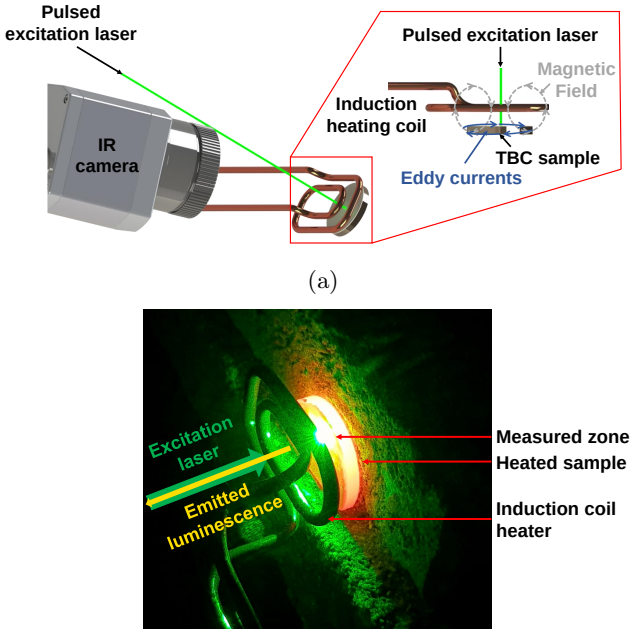

Figure 63: High temperature setup with a) the induction system principle and temperature control using a longwave infrared camera, b) a view of the heated sample with the phosphor thermometry measurement.

Acquisition of luminescence decays

The luminescence decays of the erbium emission at 545 nm and the europium emission at 590 nm were captured simultaneously, using PMT 1 and PMT 2, respectively. A Siglent SDS 1204X-E oscilloscope was used to convert the electric signal to data matrices. In front of the viewing port of PMT 1, the incoming light is composed of a spectral band which ranges in wavelength between 532 nm and 560 nm. It contains the luminescence emitted by erbium as well as some laser reflections. This light followed the optical path originating at the sample surface, reflected on the cyan dichroic filter with $R_{cyan,545nm} \approx 95\%$ and reflected on the magenta dichroic filter with $R_{magenta,545nm} \approx 92\%$. The spectral band was narrowed down to select the peak of erbium at 545 nm, using both a 543.5 nm bandpass and a laser cutoff longpass, as described in the optical setup section. Similarly, in front of PMT 2, the incoming signal contains a spectral band with a wavelength range between 560 nm and 720 nm. It contains the europium luminescence that emerges out of the sample surface and is reflected on the cyan dichroic filter with $R_{cyan,590nm} \approx 100\%$ and transmitted through the magenta dichroic filter with $T_{magenta,590nm} \approx 91\%$. The specific luminescence emission peak of europium at 590 nm was selected by placing the 590 nm bandpass described in the optical setup section in the viewing port of PMT 2. To obtain a greater amplitude of the signal that facilitates the detection of the luminescence decay and increases the signal-to-noise ratio (SNR), fixed resistance loads were connected to the RG58 coaxial cables that link the PMT detectors to the oscilloscope. Impedances of 50 kΩ and 5 kΩ were applied to the acquisition channels associated with PMT 1 for erbium and PMT 2 for europium, respectively. Figure 64 shows an example of the simultaneous decay acquisition, captured at 500°C and showing the long decay of europium (≈ 632 μs) compared to the one of erbium (≈ 13 μs) as well as the higher noise of the europium decay due to the lower resistance value chosen for the acquisition. For this experiment, the amplitude of the signal was favored over time response to enable the use of luminescence

intensities up to high temperature. By selecting these high feedthrough resistances, the minimum lifetime decay that could be accurately measured was found to be ≈ 6 μs for channel 1 and ≈ 1.5 μs for channel 2. After the completion of the experiment, the collected data was processed using a MATLAB code that synchronizes all decays so that $t = 0$ corresponds to the start of the decay at all temperatures, as presented in Figure 65. The code uses a single exponential model to fit the data of both decays. Even though the europium decay has been shown to have a triple-exponential decay behavior [106], the single exponential model has been widely used as it offers a more robust fit for the temperature measurement using this phosphor [32, 242, 203].

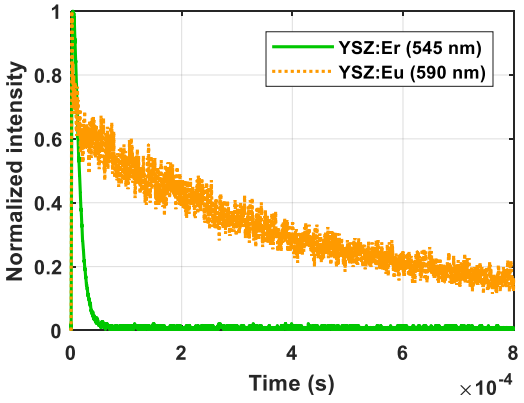

Figure 64: Synchronized collection of erbium and europium decays at 500° C.

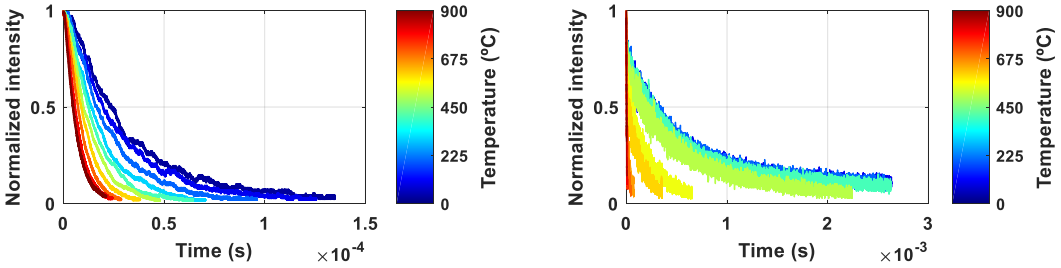

(a) Er emission at 545 nm.

(b) Eu emission at 590 nm.

Figure 65: Behavior of the luminescence decays of (a) erbium and (b) europium with respect to temperature.

Measurement of luminescence intensities

The use of two independent PMTs and high signal-to-noise ratio allows for the comparison of the intensities at $t = 0$, when the laser excitation pulse ends and where the luminescence intensity reaching the detectors is maximal. The PMTs receive a reduced region of the spectrum that is let through by the bandpasses and convert all the reaching photons to an electrical amplitude, measured in volts. The quantum efficiency of the PMTs is expected to be slightly higher at 545 nm ($\approx 20\%$) than at 590 nm ($\approx 18\%$). For this experiment, the feedthrough resistance of channel 1, that collects the luminescence of erbium, was set to a higher value than the one of channel 2, as it allowed to get amplitudes exceeding 1 V for both dopants. At room temperature, the integrated intensity of the luminescence of europium between 585 nm and 595 nm was found to be about 55% higher than the one of erbium between 538.5 nm and 548.5 nm (in the spectral ranges of the bandpasses). This is mainly due to the particular quantum yield of erbium and uropium in YSZ, with the

specific concentration and distribution parameters that were obtained for this sample. All the collected intensities were processed by the MATLAB routine to subtract the growing thermal radiation background from the measurements by averaging the intensity received by the PMTs when laser excitation is off and no luminescence remains. This takes place typically just before a new excitation pulse, which corresponds on the oscilloscope window to the trace preceding the rise-time and decay. The ratio between the normalized intensities of the two dopants can be used for high temperature measurements, assuming that the spectral shift due to temperature is negligible in comparison with the spectral bandpass of the filters used for the collection of light [135]. The integrated intensity measured by each of the two PMTs is, in consequence, assumed to remain proportional to the peak intensity of each radiative transition.

Temporal analysis

The independent luminescence decays were fitted at each 50°C step and the results were reported in Figure 66. The error bars represent the standard deviation of three independent measurements that were performed with an identical setup, on three different locations onto the sample. It can be seen that the decay of erbium at 545 nm is sensitive to temperature over the entire range of temperature from room temperature to 850°C with a lifetime decay time at room temperature of approximately 31 μs. The decay of europium has a very high sensitivity in the range of temperature comprised in between the quenching temperature of the phosphor in YSZ ($\approx$ 500°C) and 850°C, with a lifetime decay time of approximately 1.2 ms at room temperature. The advantage of the co-doped configuration and simultaneous data acquisition of the decays is the extension of the temperature range on which the decay method is applicable as the individual dopant have different maximum sensitivity temperature ranges. Past 850°C, the fits of the europium decay indicate a lifetime that stagnates around 1.5 μs which corresponds to the detection limit of the instrument on this channel, which is related to the resistance used for collection of the signal, as described in the data acquisition section. This temperature also matches with the limit found in literature for YSZ:Eu^{3+} [203, 67]. This inaccurate lifetime decay is generated by the limited response of the instrument at high temperature [26]. Reducing the resistance feedthrough on the channel can reduce the response time to some extent, but it implies a significant degradation of the SNR. A compromise between signal-to-noise ratio and time-resolution has to be selected for high temperature phosphor thermometry. The sensitivity of the decay of europium appears to be very high between 500°C and 850°C which corresponds to the luminescence quenching of the dopant into YSZ, due to the higher probability of vibrational deexcitation past the quenching temperature. However, the sensitivity of the decay of europium outside this highly sensitive temperature range is close to zero. The combination of europium with erbium, facilitated by the instrument, allows for the extension of the range of temperature that can be measured using the decay method. This is because the lifetime decay of erbium can be conveniently differentiated for any temperature between room temperature and turbine system operating temperatures.

Intensity considerations

The luminescence intensity variation was measured and the ratio between the intensities of the erbium emission at 545 nm and the europium emission at 590 nm, normalized with respect to their distinct room temperature intensity. This data was obtained to provide additional information for the temperature measurement using the phosphor thermometry instrumentation. The luminescence intensity was obtained by measuring the maximum of the amplitude of the luminescence decay, that is proportional to the amount of photons reaching each PMT at the moment where the laser excitation pulse produces the strongest

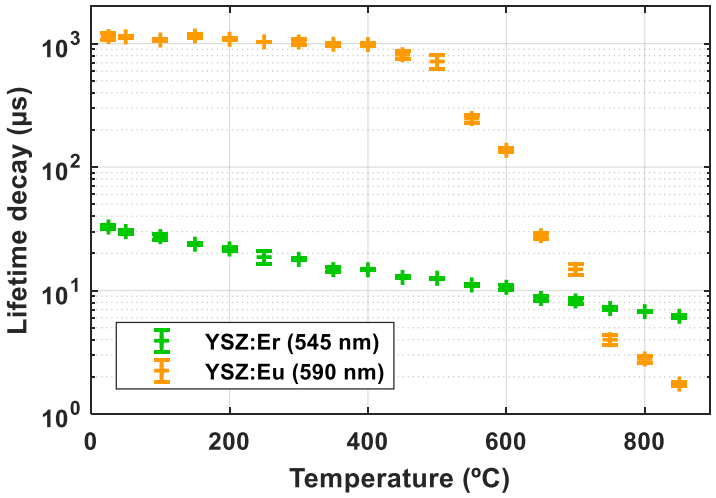

Figure 66: Lifetime decay response of APS co-doped YSZ:Er,Eu.

luminescence.

As the temperature increases, it was found that the luminescence intensity of both dopants initially increased, due to the thermal filling of the energy levels, then decreased due to thermal quenching. The growing thermal radiation, which spectral radiance can be predicted using Planck's law, provides a contribution to the overall intensity of which one part is the luminescence. The percent variation of the luminescence intensity for each dopant, with respect to the room temperature intensity is reported in Figure 67. The error bars indicate the standard deviation of three independent measurements that were performed with an identical setup, on three different locations onto the sample. It was also found that the ratio of the normalized intensity variation of erbium to europium, $R_{Er/Eu}$, has a sensitive range of temperature, usable from 850°C up to at least 1100°C, as presented in the lower plot. The error bars report the propagation of error from the ratio of the intensity variation between erbium and europium. This is a result of the fast quenching of europium luminescence on this range compared to the luminescence of erbium, that remains strong, as shown in the 3D plots. Although the lifetime decay of europium cannot be accurately determined past 850°C due to the limitation on the temporal resolution of the instrument, the high SNR allows for valid intensity measurements at higher temperatures.

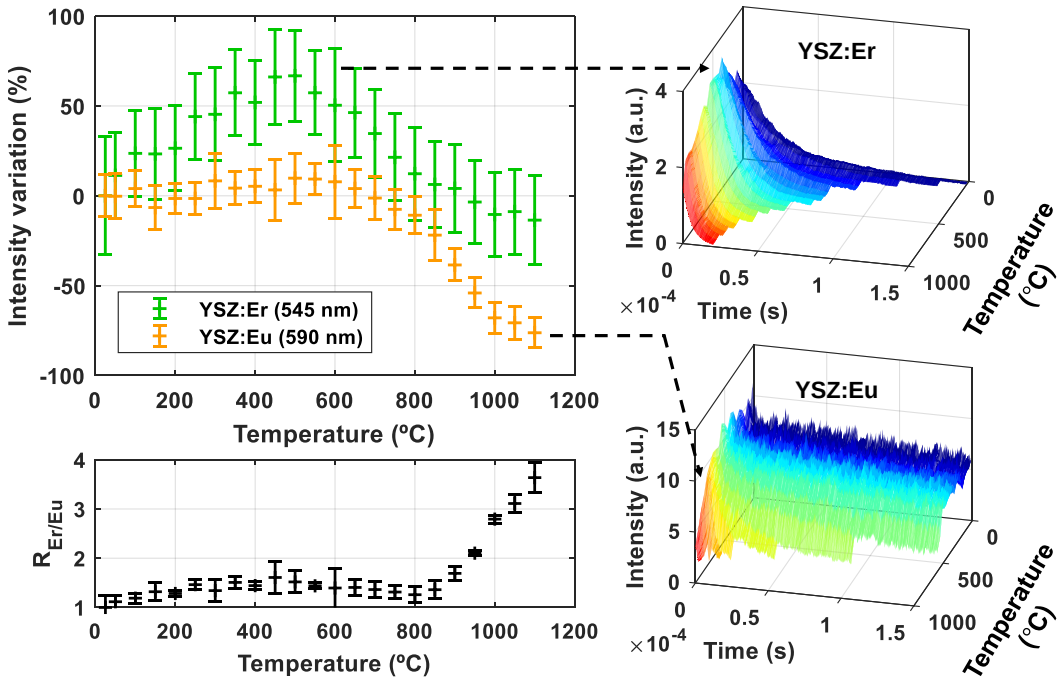

Figure 67: Percent luminescence intensity variation with respect to room temperature intensity for each dopant and corresponding ratio, sensitive between 850°C and 1100°C and usable for high temperature measurements.

Measurement error considerations

To evaluate the precision and obtain a representative response of the instrument with the YSZ:Er,Eu sample, three independent measurements were performed. The phosphor thermometry instrumentation setup remained unchanged while the sample and the induction coil were translated normally to the laser to collect the luminescence signal from three different locations. It is important to consider the intrinsic temperature measurement uncertainty implied by the utilization of infrared thermometry, which accuracy is ± 2% at high temperature. Indeed, the material was brought to the desired temperature values for data collection using infrared thermometry as the reference to determine the power input of induction heating. Another limiting factor when targeting a temperature for measurement is due to the gradient of temperature in the doped layer, created by the heat flux from the top surface to the bond coat in TBCs, but which direction is inverted in this study due to the utilization of the induction coil that heats preferentially the metallic substrate and dissipates heat by convection at the free surfaces of the material. Furthermore, material characteristics can vary importantly with position probed on the sample. For example, the random distribution of porosity affecting both thermal and optical properties of the material and the irregularity of the doped layer thickness contribute in possible variations in the luminescence of the sample. A possible uneven distribution of dopant into the material, possibly intensifying ion-ion interaction, or the consecutive thermal cycling can also result in intensity and lifetime decay variation when probing different locations onto the doped layer. Uncertainty on the exponential fit can also be significant, in particular with europium, that exhibits a triple-exponential decay behavior typically. The precision of the measurements at 800°C was found to be ± 8°C and ± 3°C, using erbium and europium decays, respectively. In addition, it can be noted that the current instrumentation is a lab-scale prototype that would necessitate automated acquisition for calibration to reduce experimental errors and that would require further development to allow for measurements on an operating engine, using an optical port, similarly to other existing instrumentation

[71].

Summary of the instrument developement

A phosphor thermometry instrument was developed for the synchronized data collection of the luminescence decay and intensity ratio measured from two independent emission peaks coming from an erbium-europium co-doped yttria-stabilized zirconia air plasma spray thermal barrier coating. The luminescence emerging out of the doped layer was collected up to 1100°C with 50°C steps, while the surface temperature was concurrently measured using a longwave infrared camera. The high resistances at the input of the oscilloscope, chosen to amplify the signal-to-noise ratio, allowed to collect lifetime decays with a sufficient bandwidth up to 850°C. The results were found to be in good accordance with literature. At higher temperatures, the limited response time was compensated by the acquisition of the ratio of intensity between erbium and europium emission peaks, that varies significantly due to the faster quenching of europium. As a consequence, the range of temperature that can be accurately measured using rare-earth doped YSZ configurations was extended up to turbine engine operating temperatures. The simultaneous acquisition of phosphor thermometry data achieved in this work paves the way for increased precision measurements on extended temperature ranges using the high-sensitivity decay method combined with the high-detectability intensity ratio method. The capabilities of this phosphor thermometry instrumentation were further demonstrated for *in-situ* temperature measurements in an actual engine rig in the following Task.

Task 6: Instrumentation adaptation to engine rig

Task 6 was added to the project in 2020 following the promising outcomes obtained in the project. The main objective of Task 6 was to focus on the adaptation of the instrumentation that we designed in earlier tasks to an operating engine test rig. Specifically, measurements were be performed on the combustion line and exhaust sections of a ramjet engine (with reminiscent gas turbine engine combustor exit temperatures and velocities) via wall sensor thermal barrier coatings.

Manufacturing of luminescent coatings

The thermal barrier coating configuration used for Task 6 was fabricated through air plasma spray using a Praxair Surface Technologies SG-100 spray gun at the Florida Institute of Technology plasma spray facility. The substrate is a 2"×2" plate of IN718 with a thickness of 0.08". The substrate was grit blasted with silica before the deposition of a 125μm NiCrAlY (NI-164/NI-211, Praxair Surface Technologies) bond coat layer. An approximately 200μm erbium-doped yttria-stabilized zirconia (YSZ:Er) top coat was then deposited onto the bond coat. The YSZ:Er powder used for plasma spray was produced by solid state reaction (Phosphor Technology Ltd). The YSZ:Er powder contains ZrO_2 bal. + 6 mol.% $YO_{1.5}$ + 1.5 mol.% $ErO_{1.5}$ (7.5 mol.% stabilizer in the form $REO_{1.5}$). A photo of the sample is shown in Figure 68(a) and the schematic layer configuration is shown in Figure 68(b). Because of mean particle size ($\approx 1\mu$m) and shape (irregular) being not ideal for spraying, 1 wt.% of fumed silica was used as a fluidizing agent to facilitate powder feeding through the air plasma spray system. The sample was annealed 30 min at 800°C to remove luminescence quenching compounds and increase luminescence intensity through partial recrystallization.

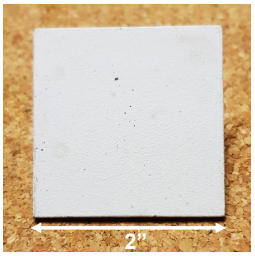

(a) Top view photograph.

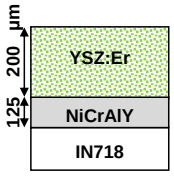

(b) Layer configuration.

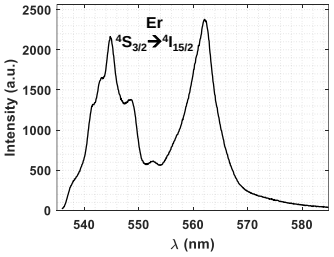

(c) Emission spectrum.

Figure 68: YSZ:Er sensor thermal barrier coating sample.

The emission spectrum of the YSZ:Er sample was measured using a fiber collection spectrometer (Pixis 100, Princeton Instruments) with a 15 mW, 532 nm laser excitation and a collection time of 100 ms. The probe has a focal length of 7.5 mm, a depth of field of 2.2 mm, a numerical aperture of 0.27, and a spot size of 200 μm. The Er-lines approximately centered at 545 nm and 562 nm were acquired. For this study, the erbium peak at 562 nm ($^4S_{3/2} \rightarrow {}^4I_{15/2}$) was selected for decay measurements. Figure 68(c) shows the emission spectrum of the YSZ:Er sensor coating.

Calibration of the temperature-decay response

Calibration of the luminescence decay profile for the sensor coating configuration developed for Task 6 was achieved using the setup presented in Figure 69. A muffle furnace was customized to have a view port for optical access for in-situ luminescence decay measurements while providing the sample placed in the furnace with as close as possible from an isothermal temperature distribution. The temperature inside the furnace was increased progressively (1°C/s) up to 1100°C to get accurate decay data as temperature at all points inside the coating, which is not cooled, can be assumed constant using this heating rate, or within a few degrees of error margin based on conduction models built up to determine heating rates in the synchrotron study. For this experiment, the laser source was set to emit 0.5 - 1 mJ pulses at a wavelength of 532 nm, with a pulse duration of approximately 10 ns, repeating with a frequency of 10 Hz. Laser mirrors were used to direct the laser excitation to the sample. The luminescence signal from the sample was reflected on a cyan dichroic filter (Thorlabs) and collected by a Hamamatsu R3896 PMT which is powered by a single precision direct current power supply providing 15 V and a maximum current of

90 mA. The PMT was used for the real-time collection of data, using a 560 nm bandpass (10 nm FWHM - Thorlabs) to collect exclusively the luminescence peak of Erbium emitted at 562 nm. For the data collection, the electric signal from the PMT passed through a transistor which impedance was set to 1 kΩ, and was then converted for analysis to data matrices using a Siglent SDS 1204X-E oscilloscope. The temperature-decay response data will be used in the engine test to determine temperature values from measured decays.

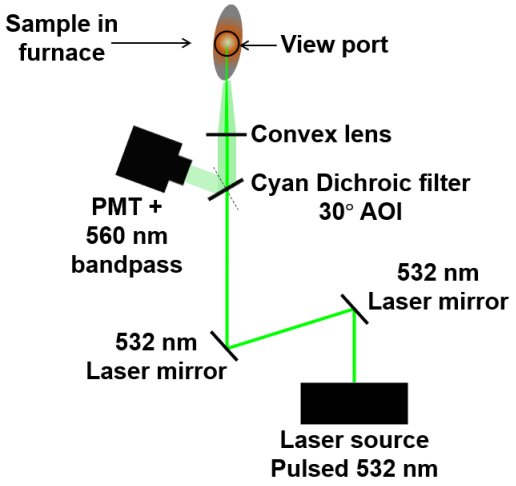

Figure 69: Phosphor thermometry instrumentation setup for the acquisition of the isothermal luminescence decay from YSZ:Er.

it can be noted that the decay of YSZ:Er presents potential for thermal gradient measurements as it exhibits a fairly ideal single-exponential trend. The raw decays are shown in function of temperature in Figure 70. The data was analyzed using a single-exponential fit model using a MATLAB code to correlate decays to temperatures. The temperature-decay response curve is presented in Figure 71. This YSZ:Er sensor is temperature sensitive across the entire range of temperatures that is used in this work, with higher sensitivity past 600°C. The tail of the calibration curve around 1000°C which slope is reduced is a detection artifact, as the decay time is close to the resolution limit that is determined in part from the detector to oscilloscope impedance input [39].

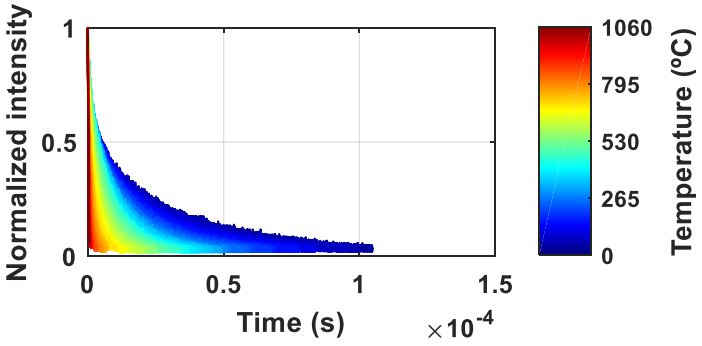

Figure 70: The evolution of the luminescence decays of YSZ:Er with increasing temperature from the emission peak at 562 nm. YSZ:Er presents a decay profile that follows closely an ideal single-exponential model.

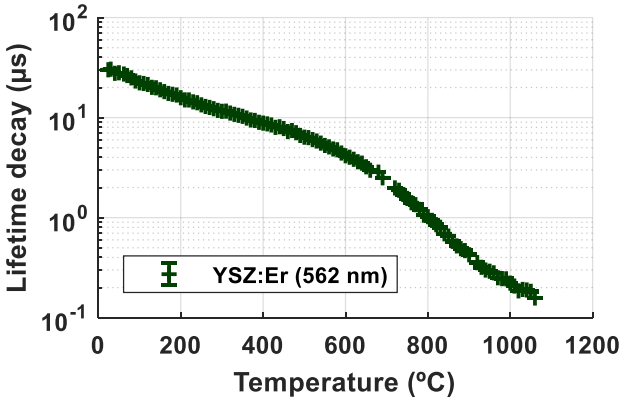

Figure 71: Temperature - luminescence decay calibration curve for the YSZ:Er sensor coating measured under isothermal conditions. This curve will be used during engine testing to determine temperature values from decays.

Integration of a high-speed camera system

One of the major effort for the increase of technology readiness level of the phosphor thermometry instrumentation developed in this project involved the ability of achieving surface temperature measurements. Research in this direction was pursued as we performed Task 6, where sensor coatings were probed using an expanded pulsed laser beam for the measurement of approximately 1-inch diameter surface areas. The setup used for this experiment is presented in Figure 72. The high-speed camera used for the test is a Photron Nova S12 monochromatic calibrated for the acquisition of 250,000 frames per second. It is equipped with a 561 nm bandpass (Edmund Optics) to filter the luminescence signal. The laser beam (which exits the laser source with an initial diameter of approximately 1 mm) was expanded using a Keplerian beam expander (25 and 125 mm focal length N-BK7 convex lenses, Thorlabs). Laser pulse was set to a frequency of 10 Hz and an energy of 0.5 mJ per pulse. A TIM450 infrared camera was used for reference temperature and surface thermal gradient measurements with an emissivity set to 0.93 for TBC in longwave infrared (7.5-13 μm).

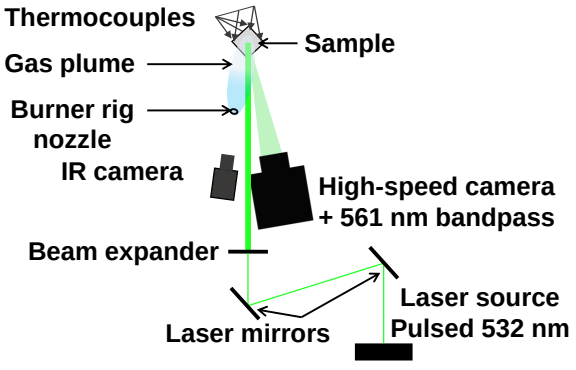

Figure 72: Experimental setup for phosphor thermometry measurements on a TBC panel with an applied thermal gradient.

The expanded beam was targeted to the sample and a laser excitation pulse was sent to the coating. The resulting image series was processed to show the initial intensity of the decay, which corresponds to the peak emission intensity of each pixel, as shown on the

left-hand side of Figure 73. It was found that the profile of intensity is not symmetric and gaussian, as it should ideally be, and this might be due to the angle at which the laser is targeted to the sample (not perfectly normal to surface). The possibility that intensity is higher in a zone of the coating due to poor dopant distribution across the surface of the coating was ruled out by measuring the point-by-point intensity of the sensor coating, as presented on the right-hand side of Figure 73.

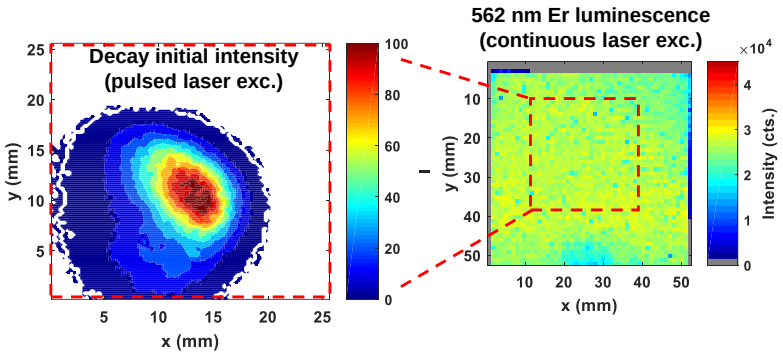

Figure 73: Normalized initial intensity map under expanded pulsed laser excitation, highlighting an asymmetric excitation profile (left). Point-by-point Er-line map (562 nm) indicates that the distribution of dopant across the surface of the sensor coating is homogeneous (right).

An initial measurement was done at room temperature and is shown in Figure 74. The average lifetime decay was found to be matching the value obtained in the calibration curve for this sample, which is around 30 μs at room temperature. The gradient observed on this first measurement could be explained by the low SNR in poorly illuminated areas, where fit quality is low, as shown in the comparison of raw decays, and where R-square is lower than 0.95. This region of low emission intensity therefore reduces confidence on fits and associated temperature measurements. In addition, the apparent gradient obtained on the collected image may be affected by the variation of fluence across the surface (the center of the beam provides slightly higher laser power per surface area). It is found in literature that fluence modifies decay time due to a change of quantum efficiency [161]. From a zero excitation power, increasing fluence initially increases quantum efficiency (more excitation power generates a stronger photon deexcitation path). Eventually, when fluence is increased further, it is known that it would favor dopant ion quenching (too many neighboring ions are getting excited in a reduced area) therefore facilitating phonon deexcitation paths and decreasing luminescence lifetime decay [7]. Other factors that may be responsible for decay variations across the probed area include varying stresses in the coating or local temperature variation due to laser heating although this would typically decrease lifetime decay unlike what is observed in this case.

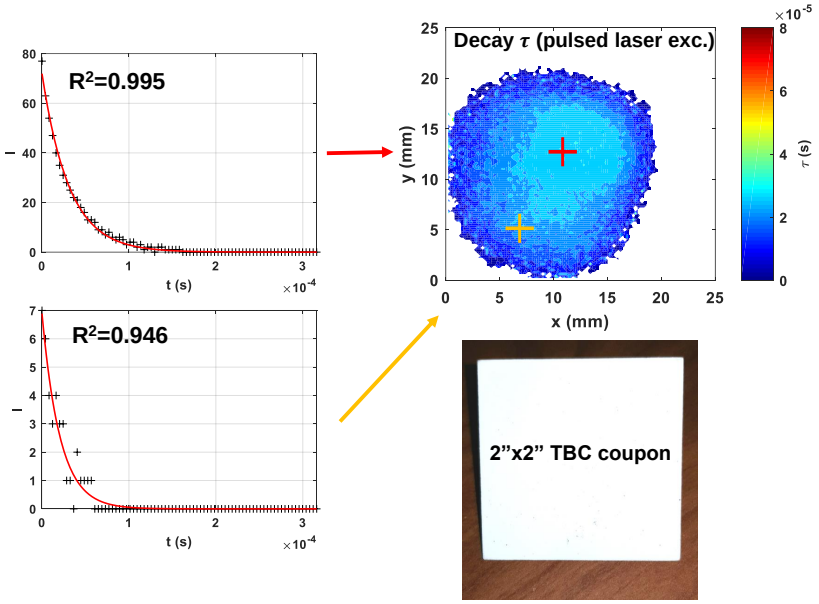

Figure 74: Varying luminescence lifetime decay at room temperature may be related to fit quality which corresponds to areas illuminated with lower laser intensities.

The YSZ:Er sensor coating luminescence lifetime decay calibration curves were collected for both photomultiplier tube (obtained in the previous section) and high-speed camera acquisition systems and are presented in Figure 75.

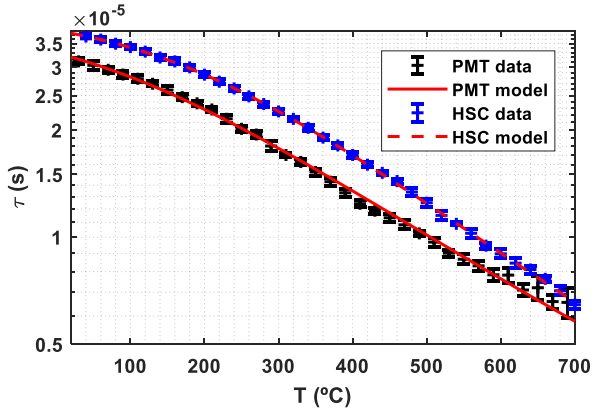

Figure 75: Calibration of the phosphor for photomultiplier tube (PMT) and high-speed camera (HSC) acquisition data methods and fitted models.

Initial high temperature measurements

High temperature measurements were performed using a butane-fueled burner rig, as shown in Figure 76. Reference surface temperatures were tracked with an infrared camera and back substrate temperatures were measured by a K-type flat-welded thermocouple placed behind the laser probed area. An additional K-type bead thermocouple was placed on the top surface for temperature validation.

This preliminary testing was achieved to evaluate high-temperature decays. This test was performed to determine the area that can be probed in high temperature conditions, where signal intensity drops. The measurements at high temperature were performed after the

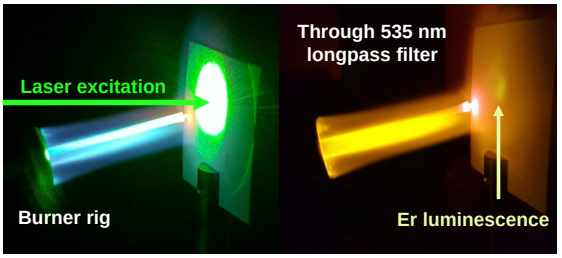

Figure 76: Burner test setup for high-speed camera measurements. Laser beam was expanded to a 1-inch diameter (left) and the 561 nm erbium luminescence decay was captured through a bandpass filter (right - here shown through a longpass filter)

coating surface temperature was brought up to 800-850°C and during cooling down with the burner flame off. Results are shown in Figure 77. To maximize accuracy of results, an area of approximately 10×10 mm^2 was selected for the analysis. It can be observed that, similarly to the data acquired at room temperature, a radial gradient is seen, in particular at 600°C, where the temperature on the probed area tends to be homogeneous based on infrared camera measurements and this gradient could be related to the variation of laser fluence across this section. At 700 and 800°C, as the coating was heated with the flame tip targeting the left side of the laser probed area, a thermal gradient can be observed with the high-speed camera measurement (lateral gradient from left to right), where fastest decays corresponding to higher temperatures can be highlighted on the left portion of the probed area.

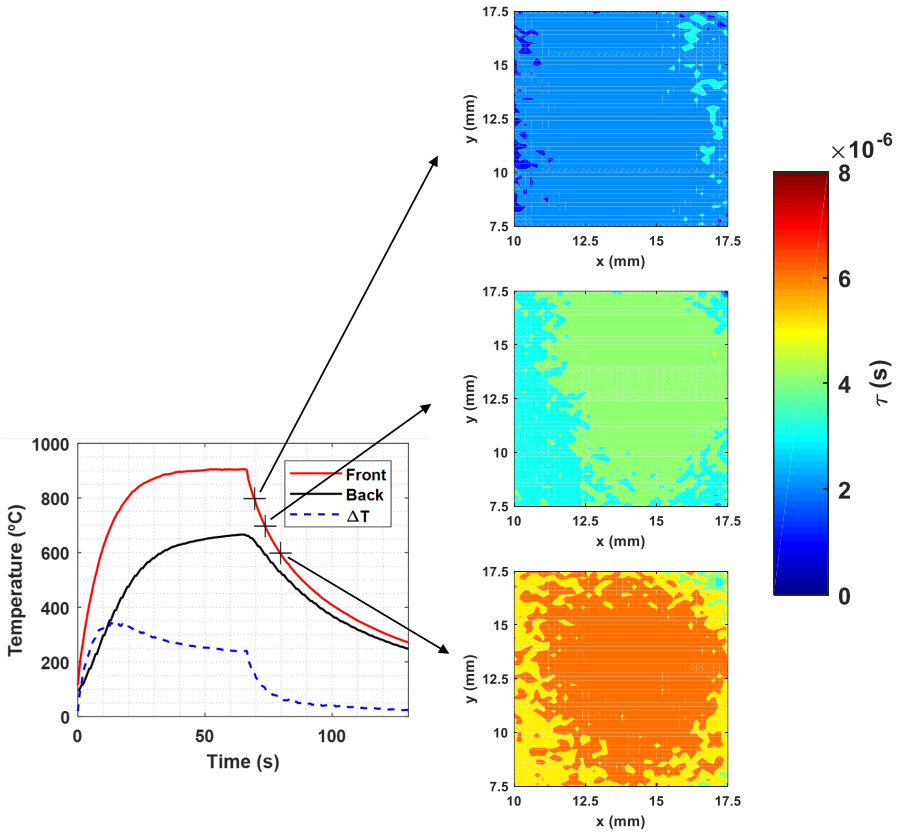

Figure 77: Initial YSZ:Er decay measurements obtained during cool down at 800° C, 700° C and 600° C, after coating surface heating using a burner rig. K-type thermocouples were placed on the front and back of the YSZ:Er coupon.

With the objective of improving confidence of fits which are required for temperature mapping, an additional test was performed using the camera at an acquisition rate of 500k frames / s. There is a compromise between spatial and temporal resolution to be found for the engine rig test. Indeed, this configuration of the camera acquisition rate reduces the number of pixels on the image. For this test, acquisition was performed during transient state (as burner rig is on) and run for 30 s. Results are reported in Figure 78. The average lifetime decay is plotted in function of time. Fluctuations are due to the non-ideal single exponential decay of the erbium line (impurities generate a short-lived decay component). At 500k frames / s, an image is captured every 2×10^{-6} s generating a synchronization shift between laser pulse and camera acquisition implies collection of varying proportion of fast decay trace. This shift can be numerically adjusted (post-processing) to synchronize laser pulse and camera frame acquisition.

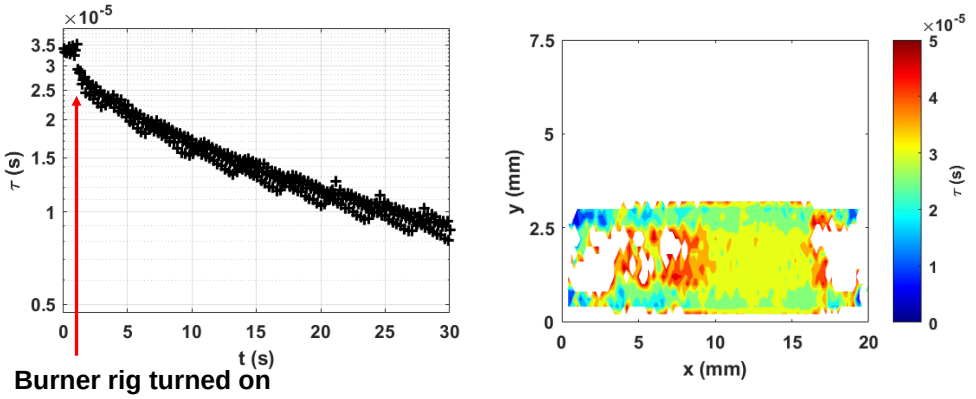

Figure 78: Transient state luminescence decay measurements with the thermal gradient heating. Averaged surface decay (left). High-speed camera decay mapping at the time when burner rig was turned on (right).

Laser beam excitiation profile was readjusted to obtain a probing area of diameter 5 mm. Luminescence lifetime decay results are presented in Figure 82(c) for YSZ:Er at room temperature. The image shows that the realignment was successful as the luminescence intensity profile appears symmetric.

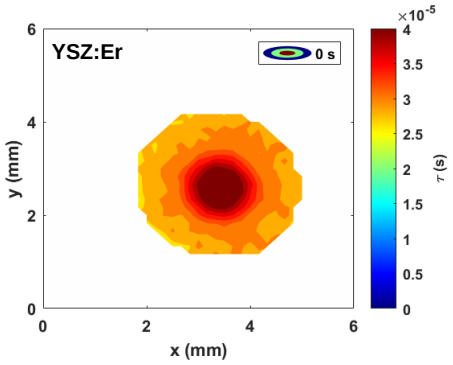

Figure 79: Decay map of YSZ:Er and room temperature after beam realignment and expansion.

Up to this point, calibration and initial testing using the phosphor thermometry instrument with integrated high-speed camera and a lab burner rig setup were performed. A number of challenges were highlighted, including detection frame rate limits, non-ideal single exponential decays, non-symmetric excitation (corrected) and resulting emission, possible varying fluence to decay effects and possible coating stresses.

Engine testing

In this work, temperature measurements were achieved using the luminescence produced by YSZ:Er^{3+} and collected simultaneously with a photomultiplier tube and a high-speed camera for higher precision, combining the two methods and demonstrating the instrument capabilities to measure *in-situ* temperature on rare-earth doped YSZ TBCs in a combustion environment. The luminescence lifetime decay method was used for conversion to temperature data, as it is reported as the most reliable method in literature for YSZ:RE sensors at high-temperature [84, 24]. The sample configuration includes a single luminescent YSZ:Er layer, chosen for maximum signal emission to facilitate data acquisition in a bright, combustion environment [75]. The experiment was conducted in a wind tunnel facility. It includes a flow-conditioning plenum, a converging nozzle, and an optically accessible test section, which exhausts to atmospheric conditions. The optical test section has a rectangular cross section and measures 127.5 mm (depth) × 45 mm (height). Air velocity through the test section was controlled by a JFlow electro-pneumatically positioned ball valve, downstream of a high-pressure regulator and air source. Air pressure was regulated to 63.6 psi upstream of the ball valve, and the mass flow rate was measured downstream of the ball valve by a Venturi flowmeter coupled with a Dwyer Instruments differential pressure transmitter (model 629C-02-CH-P2-E5-S3), resulting in uncertainty in air flow rate of 3.5%. Propane fuel pressure was set to 50.5 psi for an equivalence ratio of 1. JFlow electro-pneumatic ball valve was then actuated using a LabVIEW-based control program to obtain the target test section velocity of 13.8 m/s. The sample was placed in the test section through a 2" × 2" slot placed on the top wall of the combustion test section, coating side facing down to the combustion environment, centered approximately 180 mm upstream of the test section outlet. After the coating was mounted with a flat-welded thermocouple on the back of the substrate, a quick engine run was performed to

ensure nominal engine run conditions were met. During engine testing, high heat flux was applied on to the 2 x 2 in^2 YSZ:Er coating. The sensor coating was mounted on the top wall of the ramjet exhaust. The sample was inserted in a slot such that the YSZ:Er top coat was facing down to the exhaust section and the metal substrate of the sample facing up with a K-type thermocouple controlling back temperature. In this setup configuration, the sensor coating is set parallel to the flow. This is not a configuration that allows to reach ultra-high temperatures because of the limitation on engine run duration and the fact that flows does not impinge on the coating itself (coating is in a slot, flush with the top wall). However, sensitivity to temperature variation as well as demonstration of the temperature mapping capability was achieved. The phosphor thermometry system, presented in Figure 80, was set up to excite the sample and collect the erbium emission at 562 nm. The phosphor thermometry instrumentation is equipped with a YAG:Nd pulsed laser (CNI) that provides 10 ns of laser output at a frequency of 10 Hz. The radiation emitted by the laser head is the fundamental mode at 1064 nm with an pulse energy of approximately 2 mJ. The beam travels through a frequency doubling KTP crystal to generate 532 nm pulses of 0.5 - 1 mJ energy. The PMT is a Hamamatsu R3896 powered by a single precision direct current power supply providing 15 V and a maximum current of 90 mA. The maximum internal resistance of the gain control module of the PMT was measured to be around 80 kΩ.

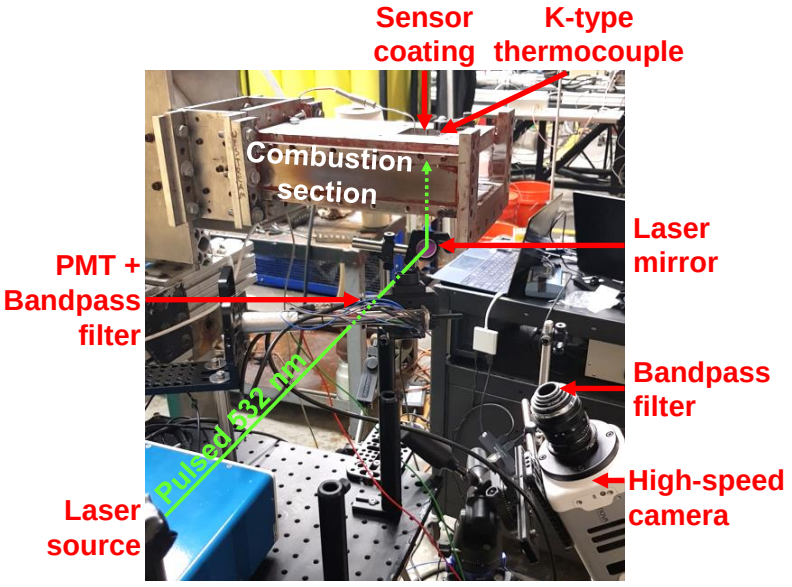

Figure 80: Experimental setup for phosphor thermometry measurements on the sensor coating.

The PMT receives a reduced region of the spectrum that is let through by the bandpass and converts all the reaching photons to an electrical amplitude, measured in volts. The quantum efficiency of the PMT is expected to be approximately 20% at 562 nm. For this experiment, the feedthrough impedance was set to 1 kΩ. The collected decay was processed by a MATLAB routine to extract decay lifetimes. The code also subtracts the the background noise due to the engine running which was found to increase the background level while the maximum initial emission intensity did not vary significantly, as shown in Figure 84. Temperature-induced spectral shift (emission peak position) was assumed to be negligible for decay-based data acquisition [135] and therefore the bandpass collects the same emission peak regardless of coating temperature. It is known that the initial intensity of the YSZ:Er decay varies with temperature [204, 77]. In addition, in an engine

environment, background noise intensity is affected by thermal radiation and laser-induced fluorescence from the combustion gas in the engine. Intensities measured by the PMT when the engine was on and off are presented in Figure 84. The light sensitivity of the high-speed camera was calibrated using the sensor coating at room temperature and in a dark environment (before engine is turned on) a with optimized laser power. The high-speed camera was triggered by the laser source for synchronized data acquisition. 300 images were acquired following each laser pulse (laser excitation duration 20 ns, energy 0.5 mJ and frequency set to 10 Hz). During the test, when engine was on, luminescence decay signal from the coating was successfully measured. For the engine test, data acquisition was started at t=0 s (where temperature of substrate measured by the thermocouple was close to 50°C), the engine started running at t=10 s and the run duration was 100 s. Data acquisition was stopped at around t=330 s. A picture of the test during the engine run is presented in Figure 85.

Moving on to the analysis of high-speed camera data, a qualitative comparison of the luminescence lifetime decay maps for the measurements on YSZ:Er is presented in Figure 81. On these 128 × 48 pixel maps, the luminescence decay obtained from each pixel (fitting a single-exponential decay model on the same pixel for successive frames) is presented. The areas where signal intensity was too weak to determine accurately luminescence lifetime decay are not shown. Therefore, there is an inherent correlation between excitation laser 2D profile intensity (surface laser power distribution), signal emission 2D intensity profile and resulting luminescence lifetime decay profile. These maps need further post-processing as, for example, in the first map a gradient of luminescence lifetime decays is observed while this map was acquired at room temperature (where the temperature at the surface of the coating must be uniform) and with engine off. However, these maps still provide useful information and demonstrate feasibility of high-speed camera measurements in combustion environments. Similarly to what was found with photomultiplier tube measurements, luminescence lifetime decay increases briefly when the engine turns on. The decay values then decrease after engine in turned on due to the increase of surface temperature. In practice, from a single measurement (following one laser pulse), a series of images was acquired by the high-speed camera and the series of intensity of each pixel was fitted to determine luminescence lifetime decays. A selection criterion was applied to remove data with low fit quality, where R^2 of fit is lower than 0.985.

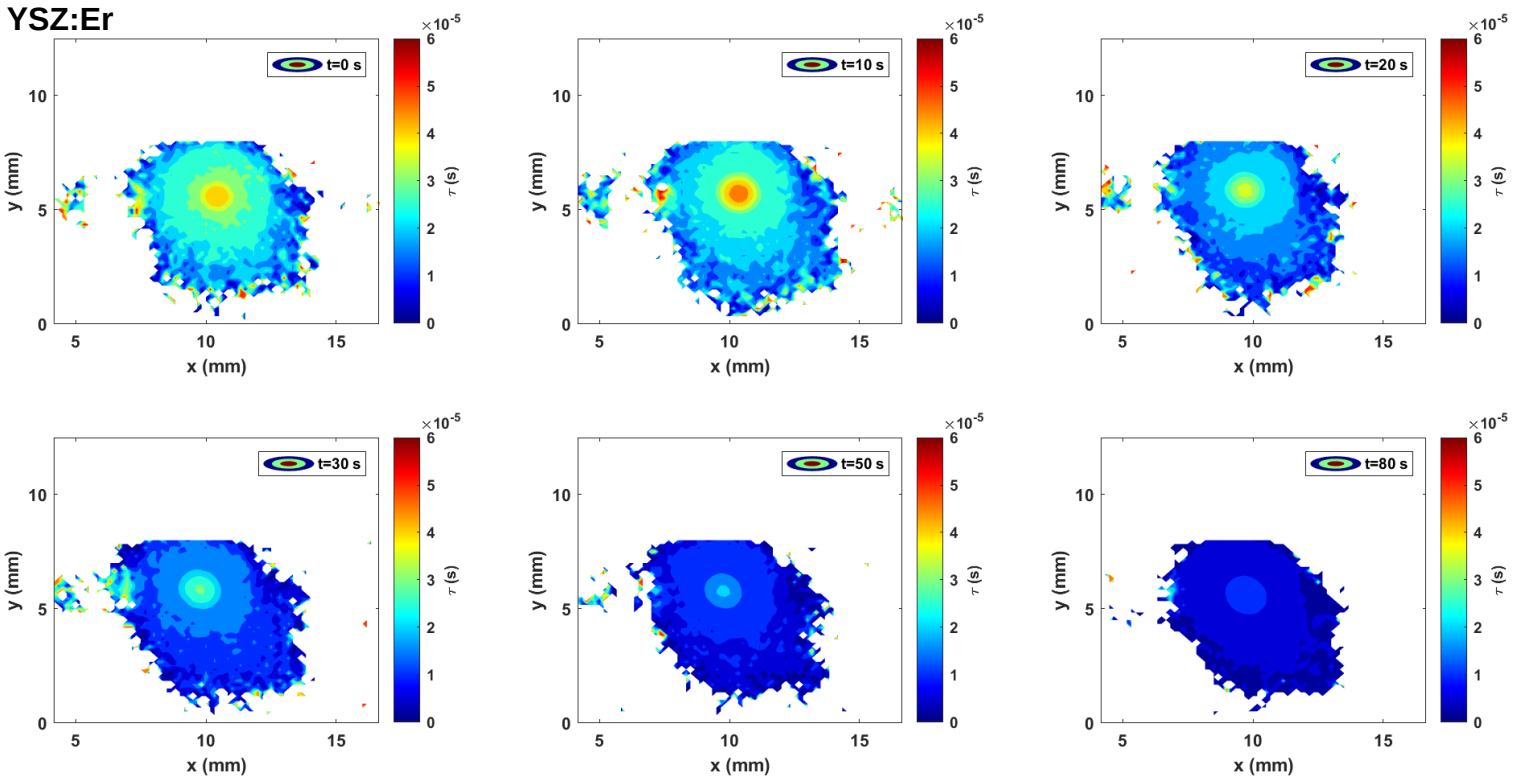

Figure 81: Initial analysis showing luminescence lifetime decay maps at different times during the engine test for YSZ:Er.

These luminescence lifetime decay maps also demonstrate potential for 2D temperature measurements in realistic engine environments. To improve the data analysis process, selective criteria were implemented on each pixel to handle cases where 1- luminescence signal intensity is too low and 2- luminescence signal intensity is too high to the point where there is saturation for the first acquired frames. These cases are presented in Figure 82. In the first case, the fit is performed only if there is sufficient intensity to obtain a decay. Indeed, if intensity corresponding to a pixel is close to background noise level, there will not be sufficient resolution to fit the data accurately. Therefore, here, an arbitrary value was chosen to determine reduce number of fits to only those with sufficient intensity. If the sum of intensities over the first 10 points is higher than 200 intensity counts, then the fit was performed. This typically also largely accelerates the analysis process (from days if we try to fit all the data, $\approx 20\times10^6$ fits, to hours if we apply this simple selection criterion, $\approx 2\times10^6$ fits). An additional restriction will then be applied to cut off decays with R^2 values that do not pass a predetermined quality threshold. The second and third cases show how fits are performed on saturated pixels (where intensity count is 255 on the first few frames), typically at the very center of the laser beam. In these cases, data is cropped to only start at the first frame which intensity is lower than the saturation intensity. This allows to significantly improve fit quality.

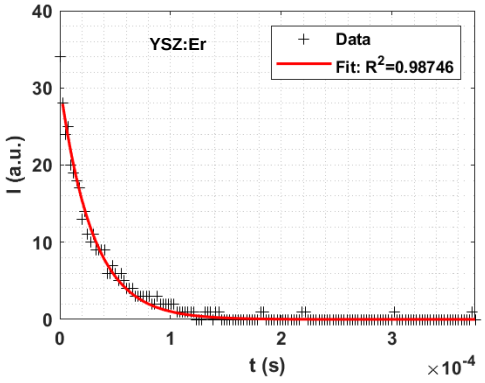

(a) Lowest accepted SNR for fit.

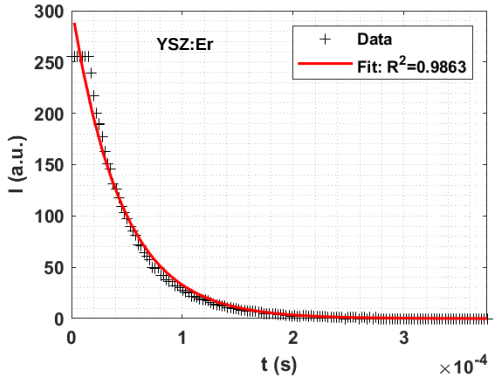

(b) Initial fitting of saturated pixel.

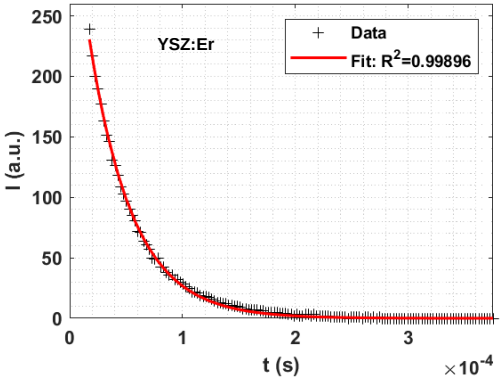

(c) Actual fitting of saturated pixel.

Figure 82: Fitting special cases: a) intensity counts corresponding to the first 10 pixels are summed to determine if the signal-to-noise ratio (SNR) is high enough for fitting, the case shown here represents the lowest accepted SNR, b) in the case where the pixel intensity is saturated, direct fitting is not ideal, c) to correct decay fitting of saturated pixel, fit starts at first non-saturated image.

High-speed camera data collected at 10 s into the engine run (corrected) is shown in Figure 86. This highlights a clear emission intensity profile on the surface of the coating which is related to the laser excitation profile (Gaussian). The determination of temperature values for these decay maps is not straight forward as it ideally requires calibration of each pixel in function of the respective excitation power due to the gradient of decays that is still present after improving the analysis methodology. We averaged the high-speed camera decays to obtain an average temperature of the probed area that can be directly compared with the

temperature obtained from PMT data. The average decay is shown in Figure 83. For YSZ:Er, the high-speed camera measurements seem to better handle the background level variations as there is no background correction needed in the high-speed camera data, in particular during transitions like when engine turns on and off. This data is very promising to accurately measure temperature in combustion environments.

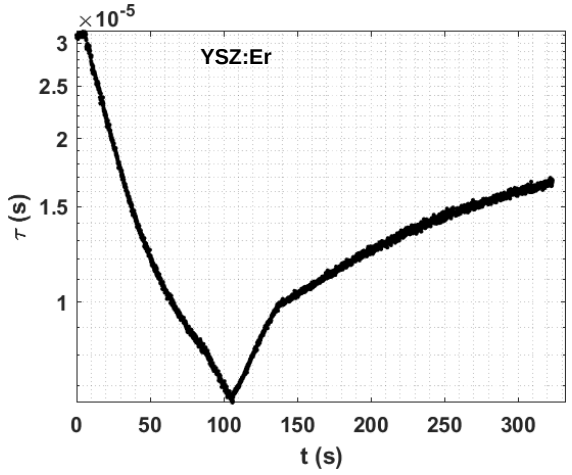

Figure 83: High-speed camera YSZ:Er luminescence decay measurement during the engine test (0-10s engine is off, 10-110s engine is on, >110s engine is off)..

The decays measured by the PMT result from the convolution of decays produced at the surface of the coating. Decays measured at different times during the engine test are presented in Figure 87. Finally, the comparison between temperatures obtained from the thermocouple placed at the back surface of the coating (not directly exposed to the heat), the high-speed camera data and the PMT data is presented in Figure 88. Temperature measured with the temperature keeps rising for more time than the engine runs because this measurement is based on transient conduction from the coating surface to the back of the sample. Overall, there is good concordance of temperature measurements using both HSC and PMT data.

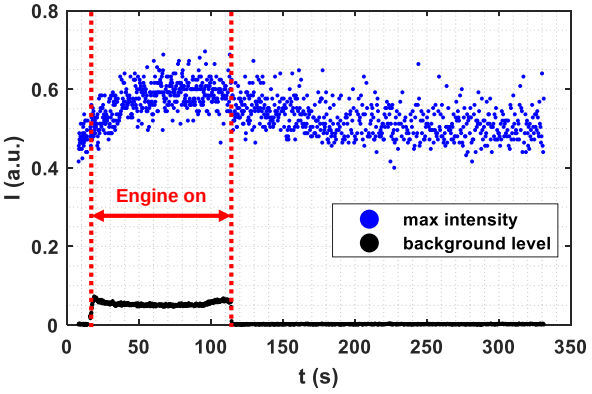

Figure 84: Oscilloscope signal maximum intensity (initial intensity of the decay) and background intensity, highlighting increased background during engine run.

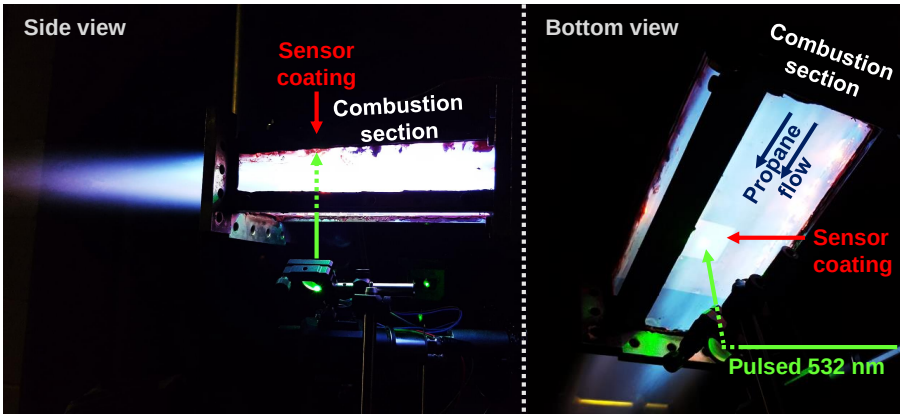

Figure 85: Phosphor thermometry measurements through the combustion environment.

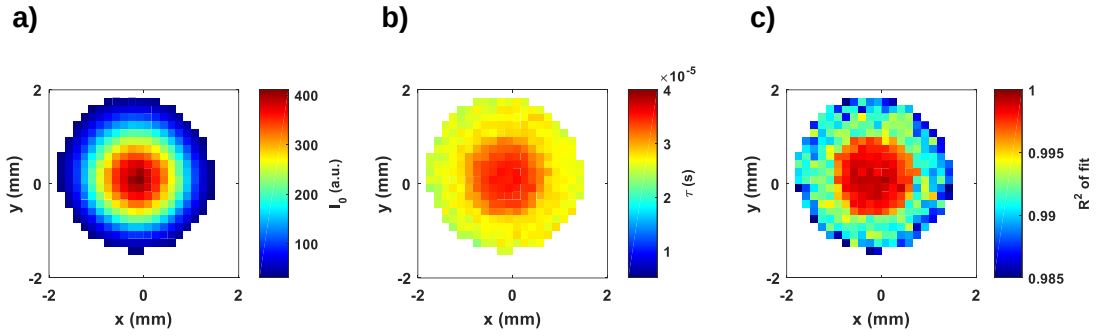

Figure 86: High-speed camera collected at 10 s into the engine run showing a) initial decay intensity, b) decay time and c) fit quality R^2.

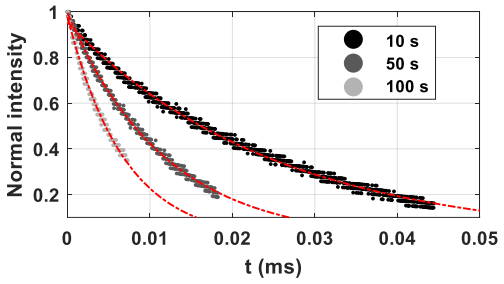

Figure 87: Photomultiplier tube decay fits during engine test.

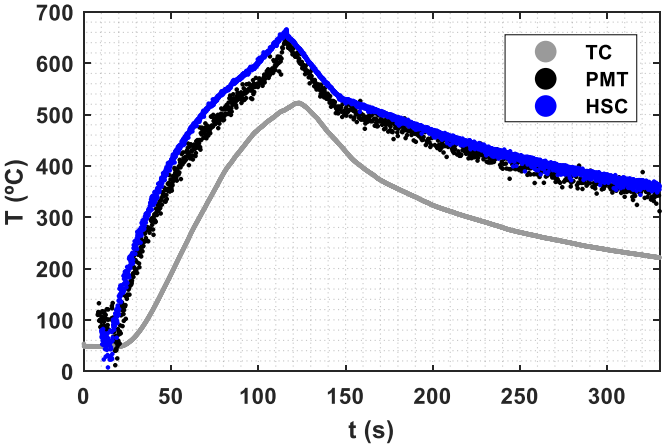

Figure 88: Temperature measured during the engine test.

Thermal barrier coating phosphor thermometry measurements were conducted using the luminescence lifetime decay of YSZ:Er in a combustion environment. Measurements were performed using both a high-speed camera and a photomultiplier tube for decay acquisition. For direct direct comparison with the photomultiplier tube data, the spatial data obtained from the high-speed camera was averaged. The high-speed camera setup provided overall reliable data, in particular during engine run, but lacked time resolution at high-temperatures. On the other hand, for the photomultiplier tube data analysis, engine background light was successfully attenuated which provided better precision at high-temperatures but this acquisition system was more affected by the growing thermal background radiation. The maximum coating temperature measured during the engine run was $\approx 660°C$, while the back surface of the sample was measured at 525°C with a flat-welded thermocouple. The results that were found for this YSZ:Er sensor are in good accordance with what is displayed in literature. This work shows that concurrent data acquisition with distinct methods can result in better confidence in temperature measurements. Further work will investigate surface temperature capabilities provided by this instrumentation for on-line temperature measurements.

c. What opportunities for training and professional development has the project provided?

Researchers have presented their progress on the project during collaborative meetings with General Electric, Siemens, Lumium, and the Argonne National Laboratory.

Collaboration with the Applied Research Laboratory of the Florida Institute of Technology allowed the students to learn about thermal spray deposition and to perform all steps of air plasma spray to create sensor coatings and overcome challenges associated with the deposition of such coatings.

The collaboration with the Argonne National Laboratory provided the opportunity to interact with synchrotron beamline scientists, and run autonomously multiple experimental campaigns at the beamline.

The collaboration with General Electric allowed researchers to identify current challenges for industry application, These exchanges were extremely beneficial to ensure proper advancement of technology readiness level of instrumentation, materials and associated methods.

The collaboration with Siemens allowed researchers to benefit from great expertise in material procurement and coating design. Siemens also mentored students on this project.

The collaboration with Lumium was critical in this project to develop and assemble the initial phosphor thermometry prototype.

The collaboration with Dr Ahmed from our department at the University of Central Florida allowed to perform engine testing on a ramjet engine rig, work achieved in collaboration with his team of students.

In December 2019, researcher Quentin Fouliard wrote his Ph.D. dissertation based on this research and was awarded the UCF (P3) Pre-eminent Postdoctoral Program Fellowship and continued to work on the project as a postdoctoral scholar until the end of this project. He also received the UCF alumni 30 Under 30 award in 2021.

Through his contribution to the project and the collaboration with GE Global Research, Quentin Fouliard was hired in a full time position at GE Global Research. Quentin will start in January 2023 and will continue working in this research field at GE.

d. How have the results been disseminated to communities of interest?

- A conference paper will be presented at the 2023 AIAA Scitech Forum:
  Q. Fouliard, R. Ghosh, S. Raghavan, “Influence of experimental parameters on rare-earth doped yttria-stabilized zirconia thermal barrier coatings for phosphor thermometry measurements”, on January 23, 2023, in National Harbor, MD.
- A manuscript is in preparation, Q. Fouliard, K. Vo, A. Masson, R. Ghosh, S. Raghavan, “Thermal barrier coating temperature measurements in combustion environments using phosphor thermometry”, Applied Physics Letters, expected for submission by the end of the year.
- A manuscript is in preparation, Q. Fouliard, R. Ghosh, S. Raghavan, “Stress-sensing luminescence decay in rare-earth doped yttria-stabilized zirconia thermal barrier coatings”, Measurement Science and Technology, expected for submission by the end of the year.
- Post-doctoral Scholar Quentin Fouliard presented “Increasing the efficiency of gas turbine engines combining novel designs and in-situ monitoring instrumentation”,

Presentation at the University of Tennessee, Knoxville, TN, October 7, 2022.

- Post-doctoral Scholar Quentin Fouliard presented "Increasing the efficiency of gas turbine engines combining novel designs and in-situ monitoring instrumentation", Seminar at Oak Ridge National Laboratory, Large Scale Structures Section, Neutron Scattering Division, Oak Ridge, TN, July 19, 2022
- Post-doctoral Scholar Quentin Fouliard presented updated results on the project at the 2022 DOE University Turbine Systems Research Project Review Meeting, held on September 29, 2022, San Diego, CA.
- Post-doctoral Scholar Quentin Fouliard presented updated results on the project at the 2022 Fossil Energy Sensor & Control Project Review Meeting, held on May 4, 2022 (online conference).
- A manuscript was published in journal Surface and Coatings Technology
  Q. Fouliard, H. Ebrahimi, J. Hernandez, K. Vo, F. Accornero, M. McCay, J.S. Park, J. Almer, R. Ghosh, S. Raghavan, "Stresses within Rare-Earth Doped Yttria-Stabilized Zirconia Thermal Barrier Coatings from in-situ Synchrotron X-Ray Diffraction at High Temperatures", in February 2022.
- A conference paper was presented at the 2022 AIAA SciTech Forum, Q. Fouliard, R. Ghosh, S. Raghavan, "Thermal Barrier Coating Delamination Monitoring Through Thermally Grown Oxide Spectral Characterization", on January 3, 2022.
- Post-doctoral Scholar Quentin Fouliard has presented updated results on the project at the 2021 University Turbine Systems Research Project Review Meeting. Major highlights, rencent project accomplishments and capabilities were displayed. The conference was held on November 10, 2021 (online conference).
- A conference paper was presented at the ASME Turbo Expo 2021 Forum:
  Q. Fouliard, J. Hernandez, H. Ebrahimi, K. Vo, F. Accornero, M. McCay, J-S. Park, J. Almer, R. Ghosh, S. Raghavan, "Synchrotron X-Ray Diffraction To Quantify In-Situ Strain On Rare-Earth Doped Yttria-Stabilized Zirconia Thermal Barrier Coatings", on June 8, 2021.
- Post-doctoral Scholar Quentin Fouliard has presented updated results on the project at the 2021 Fossil Energy Sensor & Control Project Review Meeting, held on May 19, 2021 (online conference).
- A poster titled "A Study on Phosphor Thermometry Thermal Gradient Sensitivities for Gas Turbine Environments" was presented by graduate student Johnathan Hernandez at the UCF CREOL Industrial Affiliates Symposium 2021 on April 15 and 16 (online conference).
- A conference paper was published at the AIAA Scitech 2021 Forum:
  Q. Fouliard, R. Ghosh, S. Raghavan, "Delamination of Electron-Beam Physical-Vapor Deposition Thermal Barrier Coatings using Luminescent Layers", and presented, in the symposium Structural Health Monitoring and Prognosis II, on January 12, 2021.
- Post-doctoral Scholar Quentin Fouliard has presented updated results on the project at 2020 University Turbine Systems Research Project Review Meeting, held on November 19, 2020 (online conference).
- Post-doctoral Scholar Quentin Fouliard has presented updated results on the project at the 2020 Sensors and Controls Project Review Meeting. Major highlights, rencent

project accomplishments and capabilities were displayed. The conference was held on August 26, 2020 (online conference).

- Post-doctoral Scholar Quentin Fouliard presented his work to the phosphor thermometry community at the 2^{nd} International Conference on Phosphor Thermomtery (ICPT 2020), organized in Magdeburg, Germany, on July 27-29, 2020 (online conference):
  Quentin Fouliard, Khanh Vo, Johnathan Hernandez, Ranajay Ghosh, Seetha Raghavan, "Revealing Thermal Barrier Coating Temperature Gradients via Phosphor Thermometry"

- Post-doctoral Scholar Quentin Fouliard presented his work for the 2020 International Twitter Poster Competition, fromn the American Vacuum Society (AVS), on July 8, 2020 (online event):
  Quentin Fouliard, Ranajay Ghosh, Seetha Raghavan, "Thermal Barrier Coating Delamination Evaluation using Luminescence Modeling"

- Post-doctoral Scholar Quentin Fouliard published in Surface and Coatings Technology about the coating delamination work using YSZ:Er sensor coatings, in July 2020.

- Post-doctoral Scholar Quentin Fouliard chaired a session and presented his work at the Southeast Grad Symposium of the Society for Experimental Mechanics, Lexington, KY, on June 15, 2020 (online conference):
  Quentin Fouliard, Ranajay Ghosh, Seetha Raghavan, "Thermal Barrier Coating Delamination Monitoring via Luminescence Sensing"

- Post-doctoral Scholar Quentin Fouliard published in Measurement Science and Technology about the instrumentation work on an innovative YSZ:Er,Eu sensor coating.

- A conference paper was published at the AIAA Scitech 2020 Forum:
  Q. Fouliard, R. Ghosh, S. Raghavan, "Doped 8% Yttria-Stabilized Zirconia for Temperature Measurements on Thermal Barrier Coatings using Phosphor Thermometry", and presented on January 6-10, 2020.

- Graduate student Quentin Fouliard spoke at Material Science & Technology (MS&T) 2019 conference in Portland, OR. He presented his work on Luminescence Characterization of Temperature Sensitive Phosphor Doped Thermal Barrier Coatings.

- Graduate student Quentin Fouliard was invited as a guest speaker at the Advanced Photon Source User Science Seminar at the Argonne National Laboratory in Lemont, IL, USA, on July 19, 2019. He presented results on Modeling and experimentation of temperature sensing Thermal Barrier Coatings for turbine in-situ characterization to Argonne National Laboratory scientists and external visitors.

- Two conference papers were published in TurboExpo 2019 were presented in Phoenix, AZ, USA, on June 17-21, 2019:
  P. Warren, S. Haldar, S. Raghavan, R. Ghosh (2019), Modeling Thermally Grown Oxides in Thermal Barrier Coatings using Fractal Patterns, ASME Turbo Expo 2019;
  S. Haldar, P. Warren, Q. Fouliard, D. Moreno, M. McCay, J.S. Park, P. Kenesei, J. Almer, R. Ghosh, S. Raghavan (2019), Synchrotron XRD Measurements of Thermal Barrier Coating Configurations with Rare Earth Elements for Phosphor Thermometry, ASME Turbo Expo 2019.

- Graduate student Quentin Fouliard presented instrumentation and model results at the Burnett Honors College Match Day, on May 17, 2019. A poster has been also

exposed during this event: " Configurations of Luminescence-based Temperature-Sensing Thermal Barrier Coatings".

- Graduate student Quentin Fouliard published in Applied Optics about the modeling work on sensor coatings in April 2019.
- Graduate student Quentin Fouliard presented a poster at the Industrial Affiliates Symposium, at UCF CREOL (The College of Optics and Photonics) on March 14-15, 2019:
  Quentin Fouliard, Sandip Haldar, Ranajay Ghosh, Seetha Raghavan, " Configurations of Luminescence-based Temperature-Sensing Thermal Barrier Coatings."
- Post-doctoral Fellow Sandip Haldar and Graduate student Quentin Fouliard presented posters at the University Turbine Systems Research Project Review Meeting, in Daytona Beach, FL, in November 2018:
  Q. Fouliard, S. Haldar, R. Ghosh, S. Raghavan, " Configurations of Luminescence-based Temperature-Sensing Thermal Barrier Coatings"
  S. Haldar, Q. Fouliard, P. Warren, D. Moreno, M. McCay, J.S. Park, P. Kenesei, J. Almer, R. Ghosh, S. Raghavan, "Synchrotron X-Ray Diffraction Measurements of Thermal Barrier Coating Configurations with Rare Earth Elements for Phosphor Thermometry"
- Graduate student Quentin Fouliard presented initial modeling results at the 1^{st} International Conference on Phosphor Thermometry (ICPT 2018) in Glasgow, UK, on July 25-27, 2018.

e. What do you plan to do during the next reporting period to accomplish the goals and objectives?

N/A. This is the final report.

2 PRODUCTS

(a) **Publications, conference papers, and presentations**

(i) **Journal publications**

(ii) A manuscript is in preparation, Q. Fouliard, K. Vo, A. Masson, R. Ghosh, S. Raghavan, "Thermal barrier coating temperature measurements in combustion environments using phosphor thermometry", Applied Physics Letters, expected for submission by the end of the year.

(iii) A manuscript is in preparation, Q. Fouliard, R. Ghosh, S. Raghavan, "Stress-sensing luminescence decay in rare-earth doped yttria-stabilized zirconia thermal barrier coatings", Measurement Science and Technology, expected for submission by the end of the year.

Q. Fouliard, H. Ebrahimi, J. Hernandez, K. Vo, F. Accornero, M. McCay, J.S. Park, J. Almer, R. Ghosh, S. Raghavan (2022) "Stresses within Rare-Earth Doped Yttria-Stabilized Zirconia Thermal Barrier Coatings from in-situ Synchrotron X-Ray Diffraction at High Temperatures", Surface and Coatings Technology, 444, 128647.

Q. Fouliard, R. Ghosh, S. Raghavan (2020) Quantifying Thermal Barrier Coating Delamination Through Luminescence Modeling, Surface and Coatings Technology, 399, 126153.

Q. Fouliard, J. Hernandez, B. Heeg, R. Ghosh, S. Raghavan (2020) Phosphor Thermometry Instrumentation for Synchronized Acquisition of Luminescence Lifetime Decay on Thermal Barrier Coatings, Measurement Science and Technology, 31(5), 054007

Q. Fouliard, S. Haldar, R. Ghosh, S. Raghavan (2019) Modeling Luminescence Behavior for Phosphor Thermometry Applied to Doped Thermal Barrier Coating Configurations, Applied Optics, 58(13): D68-D75

(iv) **Books or other non-periodical, one-time publications**
None at this time.

(v) **Other publications, conference papers and presentations**

Q. Fouliard, R. Ghosh, S. Raghavan, "Influence of experimental parameters on rare-earth doped yttria-stabilized zirconia thermal barrier coatings for phosphor thermometry measurements" AIAA SciTech 2023 Forum, 23-27 January 2023, National Harbor, MD

Q.Fouliard "Increasing the efficiency of gas turbine engines combining novel designs and in-situ monitoring instrumentation", Presentation at the University of Tennessee, Knoxville, TN, October 7, 2022

Q. Fouliard, R. Ghosh, S. Raghavan, "In-situ Optical Monitoring of Operating Gas Turbine Blade Coatings Under Extreme Environments" 2022 University Turbine Systems Research (UTSR) Project Review Meeting, September 27-29, 2022, San Diego, CA

Q.Fouliard "Increasing the efficiency of gas turbine engines combining novel designs and in-situ monitoring instrumentation", Seminar at Oak Ridge National

Laboratory, Large Scale Structures Section, Neutron Scattering Division, Oak Ridge, TN, July 19, 2022

Q. Fouliard, R. Ghosh, S. Raghavan, "In-situ Optical Monitoring of Operating Gas Turbine Blade Coatings Under Extreme Environments" 2022 Fossil Energy Sensor & Control Project Review Meeting, May 4, 2022 (online)

Q. Fouliard, R. Ghosh, S. Raghavan, "Thermal Barrier Coating Delamination Monitoring Through Thermally Grown Oxide Spectral Characterization" 2022 AIAA SciTech Forum, January 3, 2022 (online)

Q. Fouliard, R. Ghosh, S. Raghavan, "In-situ Optical Monitoring of Operating Gas Turbine Blade Coatings Under Extreme Environments" 2021 Virtual University Turbine Systems Research (UTSR) Project Review Meeting, November 10, 2021 (online)

Q. Fouliard, J. Hernandez, H. Ebrahimi, K. Vo, F. Accornero, M. McCay, J-S. Park, J. Almer, R. Ghosh, S. Raghavan "Synchrotron X-Ray Diffraction To Quantify In-Situ Strain On Rare-Earth Doped Yttria-Stabilized Zirconia Thermal Barrier Coatings", ASME Turbo Expo 2021: Turbomachinery Technical Conference & Exposition. American Society of Mechanical Engineers, June 7-11, 2021 (online)

Q. Fouliard, R. Ghosh, S. Raghavan, "In-situ Optical Monitoring of Operating Gas Turbine Blade Coatings Under Extreme Environments" 2021 Fossil Energy Sensor & Control Project Review Meeting, May 19, 2021 (online)

J. Hernandez, Q. Fouliard, R. Ghosh, S. Raghavan, "A Study on Phosphor Thermometry Thermal Gradient Sensitivities for Gas Turbine Environments" (poster) Industrial Affiliates Symposium, UCF CREOL, The College of Optics and Photonics, April 15-16, 2021

Q. Fouliard, R. Ghosh, S. Raghavan, "Delamination of Electron-Beam Physical-Vapor Deposition Thermal Barrier Coatings using Luminescent Layers" AIAA SciTech 2021 Forum, 11-15 & 19-21 January 2021

Q. Fouliard, R. Ghosh, S. Raghavan, "In-situ Optical Monitoring of Operating Gas Turbine Blade Coatings Under Extreme Environments" 2020 University Turbine Systems Research Project Review Meeting, November 19, 2020 (online)

Q. Fouliard, R. Ghosh, S. Raghavan, "In-situ Optical Monitoring of Operating Gas Turbine Blade Coatings Under Extreme Environments" 2020 Sensors and Controls Project Review Meeting, August 26, 2020 (online)

Q. Fouliard, K. Vo, J. Hernandez, R. Ghosh, S. Raghavan, "Revealing Thermal Barrier Coating Temperature Gradients via Phosphor Thermometry" 2nd International Conference on Phosphor Thermometry (ICPT 2020), Magdeburg, Germany, July 27-29, 2020 (online)

Q. Fouliard, R. Ghosh, S. Raghavan, "Thermal Barrier Coating Delamination Evaluation using Luminescence Modeling" American Vacuum Society (AVS), 2020 International Twitter Poster Competition, July 8, 2020 (online)

Q. Fouliard, R. Ghosh, S. Raghavan, "Thermal Barrier Coating Delamination Monitoring via Luminescence Sensing" Southeast Grad Symposium of the Society for Experimental Mechanics, Lexington, KY, June 15, 2020 (online)

Q. Fouliard, R. Ghosh, S. Raghavan (2020) Doped 8% Yttria-Stabilized Zirconia for Temperature Measurements on Thermal Barrier Coatings using Phosphor Thermometry", 2020 AIAA SciTech Forum, 6-10 January 2020, Orlando, Florida

Q. Fouliard, "In-Situ Optical Monitoring of Gas Turbine Blade Coatings Under Operational Extreme Environments" 2019 University Turbine Systems Research Project Review Meeting, Orlando, FL, November 5, 2019

Q. Fouliard, B. Heeg, R. Ghosh, S. Raghavan, "Luminescence characterization of temperature sensitive phosphor doped Thermal Barrier Coatings" Surface Protection for Enhanced Materials Performance: Science, Technology, and Application, MS&T19, Portland, OR, October 2, 2019

Q. Fouliard, "Modeling and experimentation of temperature sensing Thermal Barrier Coatings for turbine in-situ characterization" The Advanced Photon Source User Science Seminar Guest Speaker, Argonne National Laboratory, Lemont, IL, USA, July 19, 2019

P. Warren, S. Haldar, S. Raghavan, R. Ghosh (2019) "Modeling Thermally Grown Oxides in Thermal Barrier Coatings using Fractal Patterns", Proceedings of ASME Turbo Expo 2019, Phoenix, AZ, June 2019

S. Haldar, P. Warren, Q. Fouliiard, D. Moreno, M. McCay, J.S. Park, P. Kenesei, J. Almer, R. Ghosh. S. Raghavan, "Synchrotron XRD measyrements of Thermal Barrier Coating Configurations with Rare Earth Elements for Phosphor Thermometry", Proceedings of ASME Turbo Expo 2019, Phoenix, AZ, June 2019

Q. Fouliard, S. Haldar, R. Ghosh, S. Raghavan, " Configurations of Luminescence-based Temperature-Sensing Thermal Barrier Coatings." Burnett Honors College Match Day, May 17, 2019

Q. Fouliard, S. Haldar, R. Ghosh, S. Raghavan, " Configurations of Luminescence-based Temperature-Sensing Thermal Barrier Coatings." Mechanical and Aerospace Engineering Research Day, Graduate Research Forum, University of Central Florida, March 22, 2019

Q. Fouliard, S. Haldar, R. Ghosh, S. Raghavan, " Configurations of Luminescence-based Temperature-Sensing Thermal Barrier Coatings." Industrial Affiliates Symposium, UCF CREOL, The College of Optics and Photonics, March 14-15, 2019

S. Haldar, Q. Fouliard, P. Warren, D. Moreno, M. McCay, J.S. Park, P. Kenesei, J. Almer, R. Ghosh, S. Raghavan, "Synchrotron X-Ray Diffraction Measurements of Thermal Barrier Coating Configurations with Rare Earth Elements for Phosphor Thermometry", University Turbine Systems Research Project Review Meeting, Daytona Beach, FL, November 2018

Q. Fouliard, S. Haldar, R. Ghosh, S. Raghavan, " Configurations of Luminescence-based Temperature-Sensing Thermal Barrier Coatings", University Turbine Systems Research Project Review Meeting, Daytona Beach, FL, November 2018

Q. Fouliard, S. Jahan, L. Rossmann, P. Warren, R. Ghosh, S. Raghavan, "Configurations for Temperature Sensing of Thermal Barrier Coatings", 1st international Conference on Phosphor Thermometry, Glasgow, UK, July 2018

(b) **Website(s) or other Internet site(s)**

(i) http://aerostructures.cecs.ucf.edu/ , the Raghavan Research Group website, contains a page describing the equipment and capabilities associated with the project.

(c) **Technologies or techniques**
The most promising technologies developed in this project resulted in patent filing (see in next section).

An analysis code for phosphor thermometry lifetime decay measurements using surface area enabled by high-speed camera was developed.

A software package for phosphor thermometry was developed to acquire raw signal and post-process it into temperature data.

An algorithm model to optimize the composition of luminescent TBCs is was developed. The program allows for decisions of dopant type and concentration to be used as a sensor turbine blade coating.

A model for sensitivity of sensors coatings to thermal parameters was produced to allow for estimations on temperature precision using phosphor thermometry.

An optical model for TBC delamination was created to facilitate coating degration evaluation and maximize safety on coatings as well as optimize maintenance.

Phosphor thermometry using luminescence lifetime decay is the main method applied in this project to measure the temperature of the TBC at operating condition. The major goal is to increase precision and accuracy of temperature measurements to enable enhancement of gas turbine engine efficiencies and better control of coating degradation parameters. Additionally, the instrument that was designed and assembled was made portable and easy to handle at lab-scale. The measurement system eliminates some of the limitations of the concurrent temperature measurement system (infrared, thermocouples, paints) as it is based on luminescence parameters that are largely independent from combustion radiation and gas flow parameters. This instrumentation will create a new benchmark for high-temperature measurements in highly constrained extreme environments.

(d) **Inventions, patent applications, and/or licenses**

Quentin Fouliard, Ranajay Ghosh, Seetha Raghavan, “Method For Forming a Temperature Sensing Layer Within a Thermal Barrier Coating”, U.S. Patent Serial No. 17/649,929, 02/2022 (Pending)

Quentin Fouliard, Ranajay Ghosh, Seetha Raghavan. “System and Method to Reveal Temperature Gradients Across Thermal Barrier Coatings Using Phosphor Thermometry”, U.S. Patent Serial No. 17/034,156, 09/2020 (Pending)

Quentin Fouliard, Ranajay Ghosh, Seetha Raghavan. “Phosphor Thermometry System for Synchronized Luminescence Life-time Decay Measurements”, U.S. Patent Serial No. 62/944,390, 12/2019 (Pending)

Quentin Fouliard, Ranajay Ghosh, Seetha Raghavan. "Rare-earth doped thermal barrier coating bond coat for thermally grown oxide luminescence sensing." U.S. Patent No. 11,346,006. 31 May 2022.

(e) **Other products**
Nothing to report.

3 PARTICIPANTS & OTHER COLLABORATING ORGANIZATIONS

Who has been involved?
a. What individuals have worked on the project?

Name	Seetha Raghavan	Ranajay Ghosh	Quentin Fouliard	Khanh Vo	Peter Warren	Hossein Ebrahimi	Sandip Haldar	Linda Rossmann	Sanjida Jahan	Johnathan Hernandez	Kyle Rushton
Title	Professor	Associate Professor	Post-doctoral Scholar	Graduate Research Assistant	Graduate Research Assistant	Graduate Research Assistant	Post-doctoral Scholar	Graduate Research Assistant	Graduate Research Assistant	Graduate Research Assistant	Undergrad. Research Assistant
Country of residence	USA	USA	France	USA	USA	Iran	India	USA	Bangladesh	USA	USA
Contribution to the project											
# of months (Fiscal years)	60 (FY18-FY22)	60 (FY18-FY22)	60 (FY18-FY22)	39 (FY20-FY22)	19 (FY18-FY19)	19 (FY19-FY20)	15 (FY18-FY19)	13 (FY18)	10 (FY18)	7 (FY20-FY21)	6 (FY18-FY19)
Task #	All	All	All	T3-T6	T2-T3	T3-T4	T1-T4	T4	T4	T3-T6	T4
Traveled to foreign country (collaborator	Yes, Netherlands (Lumium)	No	No	No	No	No	No	No	Yes, Netherlands (Lumium)	No	No

Individuals who contributed to the project.

b. Has there been a change in the active other support of the PD/PI(s) or senior/key personnel?
No.

c. What other organizations have been involved as partners?

Partner	GE Aviation / GE Global Research	Lumium	Siemens	Florida Institute of Technology	Argonne National Laboratory
Location of organization	1 Neumann Way, Cincinnati, OH 45215 / 1 Research Cir, Niskayuna, NY 12309	Eewal 84, 8911 GV, Leeuwarden, Netherlands	11842 Corporate Blvd, Orlando, FL 32817	328 W. Hibiscus Blvd, Melbourne, FL 32901	9700 Cass Av, Lemont, IL 60439
Partner's contribution	Expertise support and sample manufacturing and preparation	Configuration / Calibration of the equipment for luminescence	Expertise support, materials procurement	Manufacturing expertise support	Synchrotron expertise support

Collaboration with other organizations.

d. Have other collaborators or contacts been involved?
Dr. Jeffrey Bunn, HFIR, ORNL, Oak Ridge, TN (discussions for future research) Dr. Kareem Ahmed, Mechanical and Aerospace Engineering Department, University of Central Florida, Orlando, FL (engine testing, Task 6)

4 IMPACT

What was the impact of the project? How has it contributed to advance research in the field?
It is envisioned that the outcomes of this research will support the goal of improving the operational capability of current TBCs and further lead to innovative design platforms for high temperature materials systems with the potential to extend overall material performance and durability limits in energy and propulsion. This will impact on the economy of the turbine engine industry as well as the research area concerning optics, chemistry, physics etc. The project also provides the opportunity to train university researchers to correlate fundamental, experimental research with industry applications.

a. What was the impact on the development of the principal discipline(s) of the project?
The effectiveness of advanced online instrumentation lies in the capacity to predict physical, chemical and mechanical properties that can provide real-time actionable insight to mitigate failure and damage thereby assuring functionality, safety and cost savings for gas turbine operation. The research effort in this project focused directly on advancing instrumentation to monitor thermal barrier coatings (TBCs) that have contributed significantly to improving fuel efficiency and durability of gas turbine engines. The monitoring of these coatings represents an important advancement toward achieving the program goals of improved reliability availability and maintainability of existing and advanced gas turbine power plants.

b. What was the impact on other disciplines?
The project delivered an advanced phosphor thermometry system that can be integrated to an engine rig to measure in-situ temperatures. This equipment works using the luminescence lifetime decay and intensity variations that are sensitive temperature-dependent properties. Additionally, a software package to analyze phosphor thermometry data was developed for data analysis. Other spectroscopy measurements were made to demonstrate further capabilities of luminescent sensors. For example, thermal barrier coating delamination and erosion evaluation was obtained in addition to the thermometry measurements. This project also contributed to the understanding of the effects of microstructure modifications that are done when converting a standard thermal barrier coating to a sensor coating. For this purpose, X-ray diffraction measurements were used to determine internal stress localization therefore helping towards a better understanding of expected sensor coating lifetime. The development of benchmark methodologies for improved accuracy in engine thermometry was performed, using infrared cameras. A series of models was created to enable predictions on coating optical and mechanical response, therefore enabling optimization of sensor configurations. All the products and results of this research can be applied to broader scientific fields/sectors.

c. What was the impact on the development of human resources?
University students and researchers gained hands-on experience on the experimental work that was necessary to develop the instrumentation. They were guided and instructed by their supervisors, the PI and co-PI of the project, and they benefited from active collaboration with experienced industry partners. They improved communication, planning and scheduling. and presentation skills through report writing, conferences and publications. This project formed a number of individuals that were able to utilize the skills acquired through this project to later face challenges of applying research solutions to industry applications or to pursue their careers in academia or industry.

d. What was the impact on teaching and educational experiences?
Significant content regarding the spectroscopy methods for non-destructive evaluation and

phosphor thermometry instrumentation are being taught in class (UCF EAS 6222 - Non-Destructive Evaluation Methods for Aerospace Applications).

Researchers in this project contributed to the STEM event at the AIAA Space Conference held in Orlando, 17-19 September, 2018. and to STEM events organized by the University of Central Florida and held yearly on its campus.

e. What was the impact on physical, institutional, and information resources that form infrastructure?
The optimization algorithm and other models that were developed in this project help towards fast selection of TBC configurations (in terms of compositions, topology, optical performance for sensor, thermal properties). The measurement technologies including the instrumentation buildup that were developed in this project will help improve gas turbine reliability and efficiency through more accurate monitoring of operational conditions in gas turbine engines. The methods developed in this project provide means to better understand factors of coating degradation and lifetime. For phosphor thermometry measurements specifically, viable sensor coating configurations were demonstrated and details on the optimal optical setup was published. Methods for delamination monitoring was presented and approved by the scientific community through various conferences and publications.

f. What was the impact on technology transfer?
Instrumentation, methodologies and key concepts developed in this project were patented. It is expected that the technology will gain attractiveness in the future as more advanced gas turbine engines are produced. The research led in this project will positively contribute to accelerate transition to greener and safer gas turbine engine operation. Phosphor thermometry luminescence lifetime measurements through sensor TBCs is rapidly developing and concepts were largely demonstrated in this research, improving TRL of this technology.

g. What was the impact on society beyond science and technology?
Improving the accuracy and reliability of in-situ measurements of gas turbine engine components will improve engine efficiency, which is highly beneficial to reduce emission and fuel consumption. The research performed through this project is a step forward towards zero carbon emission and safer engine operation.

h. What percentage of the award's budget was spent in foreign country(ies)?
6.95% of overall budget spent in a foreign country (Netherlands) as part of the collaboration with Lumium for the development of the $51,000 multipoint phosphor thermometry system, as described in the proposal.

5 CHANGES/PROBLEMS

(a) **Changes in approach and reasons for change**
This project received a two-year extension following the successful demonstration of lab-scale instrumentation over the initial duration of the awarded project to adapt it to an engine rig. During the initial period (October 2017 - September 2020), tasks 1 to 5 were successfully completed, Task 6 was successfully completed by the end of the project (September 2022). Results are presented in reports and pending publications.

(b) **Actual or anticipated problems or delays and actions or plans to resolve them**
N/A.

(c) **Changes that have a significant impact on expenditures**
The extension of the project to modify the instrumentation and adapt it to an engine rig required significant modification on the setup, mounting and optics.

(d) **Significant changes in use or care of human subjects, vertebrate animals, biohazards, and/or select agents**
N/A.

(e) **Change of primary performance site location from that originally proposed**
N/A.

6 SPECIAL REPORTING REQUIREMENTS

None.

7 BUDGETARY INFORMATION

See attached spreadsheet.

8 PROJECT OUTCOMES:

What were the outcomes of the award?
Precise determination of temperatures in TBCs result in large benefits in terms of fuel savings, reduction of emission, as well as better monitoring of TBC lifetime. This award allowed to:

- Develop sensor coating configurations and phosphor thermometry instrumentation. Through this research:
  - We enabled the extension of the range of measurable temperatures using phosphor thermometry with higher sensitivity by capturing simultaneously luminescence decays and intensities using a co-doped YSZ:Er,Eu sensor TBC.
  - We demonstrated surface temperature measurement capabilities using a phosphor thermometry system with a high-speed camera setup for in-situ engine measurements.
- Quantify stress in sensor coatings through synchrotron transmission X-ray diffraction.
  - Sensor coatings exhibit similar residual / in-situ top coat stresses (compared to state-of-the-art)
- Highlight luminescence spectroscopy capabilities for damage detection in coatings.
- Demonstrate capabilities for accurate delamination quantification
- Develop representative models to extrapolate to different coating configurations

Results were published in Applied Optics (2019) for the prediction models for the selection of sensor coating configurations. Measurement Science Technology (2020, 2022) for the design and demonstration of the phosphor thermometry system. Surface and Coatings Technology (2020, 2022) for delamination monitoring using embedded luminescence sensors and for the determination of phosphor coating thermomechanical integrity . Research was presented at conferences including: AIAA Scitech (2020, 2021, 2022), ASME Turbo Expo (2019, 2021), ICPT (2018, 2020), AVS (2020), SEM (2020), MS&T (2019).
Four patent submissions were completed on instrumentation, material configurations and data processing methodologies developed for improved temperature measurement accuracy using phosphor thermometry.

References

[1] J Aktaa, K Sfar, and D Munz. Assessment of tbc systems failure mechanisms using a fracture mechanics approach. *Acta materialia*, 53(16):4399–4413, 2005.

[2] Khaled Al-Athel, Kaspar Loeffel, Haowen Liu, and Lallit Anand. Modeling decohesion of a top-coat from a thermally-growing oxide in a thermal barrier coating. *Surface and Coatings Technology*, 222:68–78, 2013.

[3] Sami Alaruri, Lisa Bianchini, and Andrew Brewington. Effective spectral emissivity measurements of superalloys and ysz thermal barrier coating at high temperatures using a 1.6 μm single wavelength pyrometer. *Optics and lasers in engineering*, 30(1):77–91, 1998.

[4] Sami D Alaruri, Lisa Bianchini, and Andrew Brewington. Emissivity measurements for ysz thermal barrier coating at high temperatures using a 1.6-um single-wavelength pyrometer. *Optical Engineering*, 37(2):683–687, 1998.

[5] Marcus Aldén, Alaa Omrane, Mattias Richter, and Gustaf Särner. Thermographic phosphors for thermometry: a survey of combustion applications. *Progress in energy and combustion science*, 37(4):422–461, 2011.

[6] Stephen Allison, Shawn Goedeke, Michael Cates, Tom Bonsett, Donald Smith, Andrew Brewington, and Timothy Bencic. Phosphor thermometry in an operating turbine engine. In *41st AIAA/ASME/SAE/ASEE Joint Propulsion Conference & Exhibit*, page 4374, 2005.

[7] SW Allison and GT Gillies. Remote thermometry with thermographic phosphors: Instrumentation and applications. *Review of Scientific Instruments*, 68(7):2615–2650, 1997.

[8] JD Almer and SR Stock. Internal strains and stresses measured in cortical bone via high-energy x-ray diffraction. *Journal of Structural Biology*, 152(1):14–27, 2005.

[9] Ö Altun and Y Böke. Effect of the microstructure of eb-pvd thermal barrier coatings on the thermal conductivity and the methods to reduce the thermal conductivity. *Arch Mater Sci*, 48(48):48, 2009.

[10] Stéphane AMIEL, Etienne COPIN, Thierry SENTENAC, Yannick LE MAOULT, and Philippe LOURS. Caractérisation de marqueurs photoluminescents de l'histoire thermique.

[11] Stéphane Amiel, Etienne Copin, Thierry Sentenac, Philippe Lours, and Yannick Le Maoult. On the thermal sensitivity and resolution of a ysz: Er3+/ysz: Eu3+ fluorescent thermal history sensor. *Sensors and Actuators A: Physical*, 272:42–52, 2018.

[12] ER Andrievskaya. Phase equilibria in the refractory oxide systems of zirconia, hafnia and yttria with rare-earth oxides. *Journal of the European ceramic Society*, 28(12):2363–2388, 2008.

[13] S Asghari and M Salimi. Finite element simulation of thermal barrier coating performance under thermal cycling. *Surface and Coatings Technology*, 205(7):2042–2050, 2010.

[14] MP Bacos, JM Dorvaux, O Lavigne, R Mévrel, M Poulain, C Rio, and MH Vidal-Setif. Performance and degradation mechanisms of thermal barrier coatings for turbine blades: a review of onera activities. *AerospaceLab*, (3):p–1, 2011.

[15] Martin Bäker. Finite element simulation of interface cracks in thermal barrier coatings. *Computational Materials Science*, 64:79–83, 2012.

[16] DS Balint and JW Hutchinson. An analytical model of rumpling in thermal barrier coatings. *Journal of the Mechanics and Physics of Solids*, 53(4):949–973, 2005.

[17] Marion Bartsch, Iulian Mircea, Jens Suffner, and Bernd Baufeld. Interfacial fracture toughness measurement of thick ceramic coatings by indentation. In *Key Engineering Materials*, volume 290, pages 183–190. Trans Tech Publ, 2005.

[18] Piotr Bednarz. *Finite element simulation of stress evolution in thermal barrier coating systems*. Forschungszentrum, Zentralbibliothek, 2006.

[19] V Menvie Bekale, Anne-Marie Huntz, Corinne Legros, Gaël Sattonnay, and François Jomard. Impurity diffusion of cerium and gadolinium in single-and polycrystalline yttria-stabilized zirconia. *Philosophical Magazine*, 88(1):1–19, 2008.

[20] Per Bengtsson and Christer Persson. Modelled and measured residual stresses in plasma sprayed thermal barrier coatings. *Surface and Coatings Technology*, 92(1-2):78–86, 1997.

[21] Marcin Białas. Finite element analysis of stress distribution in thermal barrier coatings. *Surface and Coatings Technology*, 202(24):6002–6010, 2008.

[22] C Bird, JE Mutton, R Shepherd, MDW Smith, and HML Watson. Surface temperature measurement in turbines. In *AGARD conference proceedings*, pages 21–4. AGARD, 1998.

[23] J Brübach, A Dreizler, and J Janicka. Gas compositional and pressure effects on thermographic phosphor thermometry. *Measurement Science and Technology*, 18(3):764, 2007.

[24] Jan Brübach, Christian Pflitsch, Andreas Dreizler, and Burak Atakan. On surface temperature measurements with thermographic phosphors: a review. *Progress in Energy and Combustion Science*, 39(1):37–60, 2013.

[25] Esteban P Busso, ZQ Qian, MP Taylor, and HE Evans. The influence of bondcoat and topcoat mechanical properties on stress development in thermal barrier coating systems. *Acta materialia*, 57(8):2349–2361, 2009.

[26] Tao Cai, Yongzeng Li, Songtao Guo, Di Peng, Xiaofeng Zhao, and Yingzheng Liu. Pressure effect on phosphor thermometry using mg4fgeo6: Mn. *Measurement Science and Technology*, 30(2):027001, 2019.

[27] Pedro P Camanho and Carlos G Dávila. Mixed-mode decohesion finite elements for the simulation of delamination in composite materials. *NASA/TM-2002-211737 (2002)*, 2002.

[28] Novel Material Center. Non-ferrous metal new material property database, 2001 (accessed May 19, 2020). Online Database, http://www.ostec.or.jp/nmc/ndb/main.htm.

[29] F Cernuschi and S Marinetti. Discrimination between over-thickness and delamination of thermal barrier coatings by apparent thermal effusivity thermographic technique. *Journal of thermal spray technology*, 19(5):958–963, 2010.

[30] MD Chambers and David R Clarke. Effect of long term, high temperature aging on luminescence from eu-doped ysz thermal barrier coatings. *Surface and coatings technology*, 201(7):3942–3946, 2006.

[31] MD Chambers and DR Clarke. Terbium as an alternative for luminescence sensing of temperature of thermal barrier coating materials. *Surface and Coatings Technology*, 202(4-7):688–692, 2007.

[32] MD Chambers and DR Clarke. Doped oxides for high-temperature luminescence and lifetime thermometry. *Annual Review of Materials Research*, 39:325–359, 2009.

[33] X Chen, Z Mutasim, J Price, JP Feist, AL Heyes, and S Seefeldt. Industrial sensor tbcs: Studies on temperature detection and durability. *International Journal of Applied Ceramic Technology*, 2(5):414–421, 2005.

[34] Liudmyla M Chepyga, Andres Osvet, Christoph J Brabec, and Miroslaw Batentschuk. High-temperature thermographic phosphor mixture yap/yag: Dy3+ and its photoluminescence properties. *Journal of Luminescence*, 188:582–588, 2017.

[35] NS Cheruvu, KS Chan, and R Viswanathan. Evaluation, degradation and life assessment of coatings for land based combustion turbines. *Energy Materials*, 1(1):33–47, 2006.

[36] Jerome Chevalier, Laurent Gremillard, Anil V Virkar, and David R Clarke. The tetragonal-monoclinic transformation in zirconia: lessons learned and future trends. *Journal of the American Ceramic Society*, 92(9):1901–1920, 2009.

[37] David R Clarke, Matthias Oechsner, and Nitin P Padture. Thermal-barrier coatings for more efficient gas-turbine engines. *MRS bulletin*, 37(10):891–898, 2012.

[38] David R Clarke and Simon R Phillpot. Thermal barrier coating materials. *Materials today*, 8(6):22–29, 2005.

[39] DR Clarke and MM Gentleman. Luminescence sensing of temperatures in thermal barrier coatings. *Surface and Coatings Technology*, 202(4-7):681–687, 2007.

[40] TW Clyne and SC Gill. Residual stresses in thermal spray coatings and their effect on interfacial adhesion: a review of recent work. *Journal of Thermal Spray Technology*, 5(4):401, 1996.

[41] EB Copin, Y Le Maoult, T Sentenac, F Blas, THG Tran, and P Lours. Comparison of ir thermography and photoluminescence for early diagnostic of spallation and temperature sensing in thermal barrier coatings.

[42] EB Copin, X Massol, S Amiel, T Sentenac, Y Le Maoult, and P Lours. Novel erbia-yttria co-doped zirconia fluorescent thermal history sensor. *Smart Materials and Structures*, 26(1):015001, 2016.

[43] Etienne Copin. *Fonctionnalisation de barrières thermiques aéronautiques YSZ issues de la voie sol-gel: mesure de température et diagnostic de l'endommagement par fluorescence*. PhD thesis, Ecole des Mines d'Albi-Carmaux, 2015.

[44] Etienne Copin, Thierry Sentenac, Yannick Le Maoult, Fabien Blas, Florence Ansart, Vanessa Vidal, and Philippe Lours. Feasibility of luminescent multilayer sol-gel thermal barrier coating manufacturing for future applications in through-thickness temperature gradient sensing. *Surface and Coatings Technology*, 260:90–96, 2014.

[45] R Darolia. Thermal barrier coatings technology: critical review, progress update, remaining challenges and prospects. *International materials reviews*, 58(6):315–348, 2013.

[46] John Davies. *Conduction and induction heating*. Number 11. IET, 1990.

[47] Howie RA DEER WA and J Zussman. An introduction to the rock forming minerals, 1966.

[48] Ralph B Dinwiddie, Stephen C Beecher, Wallace D Porter, and Ben A Nagaraj. The effect of thermal aging on the thermal conductivity of plasma sprayed and eb-pvd thermal barrier coatings. In *ASME 1996 International Gas Turbine and Aeroengine Congress and Exhibition*, pages V005T13A006–V005T13A006. American Society of Mechanical Engineers, 1996.

[49] Elena R Dobrovinskaya, Leonid A Lytvynov, and Valerian Pishchik. Properties of sapphire. In *Sapphire*, pages 55–176. Springer, 2009.

[50] Miroslav D Dramićanin. Sensing temperature via downshifting emissions of lanthanide-doped metal oxides and salts. a review. *Methods and applications in fluorescence*, 4(4):042001, 2016.

[51] H Ebrahimi and S Nakhodchi. Thermal fatigue testing and simulation of an aps tbc system in presence of a constant bending load. *International Journal of Fatigue*, 96:1–9, 2017.

[52] Jeffrey I Eldridge. Optical diagnostics for high-temperature thermal barrier coatings. 2009.

[53] Jeffrey I Eldridge and Timothy J Bencic. Monitoring delamination of plasma-sprayed thermal barrier coatings by reflectance-enhanced luminescence. *Surface and Coatings Technology*, 201(7):3926–3930, 2006.

[54] Jeffrey I Eldridge, Timothy J Bencic, Stephen W Allison, and David L Beshears. Depth-selective diagnostics of thermal barrier coatings incorporating thermographic phosphors. 2003.

[55] Jeffrey I Eldridge, Timothy J Bencic, Charles M Spuckler, Jogender Singh, and Douglas E Wolfe. Delamination-indicating thermal barrier coatings using ysz: Eu sublayers. *Journal of the American Ceramic Society*, 89(10):3246–3251, 2006.

[56] Jeffrey I Eldridge, Thomas P Jenkins, Stephen W Allison, Scott Cruzen, JJ Condevaux, JR Senk, and AD Paul. Real-time thermographic-phosphor-based temperature measurements of thermal barrier coating surfaces subjected to a high-velocity combustor burner environment. 2011.

[57] Jeffrey I Eldridge, Jogender Singh, and Douglas E Wolfe. Erosion-indicating thermal barrier coatings using luminescent sublayers. *Journal of the American Ceramic Society*, 89(10):3252–3254, 2006.

[58] Jeffrey I Eldridge, Charles M Spuckler, and Richard E Martin. Monitoring delamination progression in thermal barrier coatings by mid-infrared reflectance imaging. *International journal of applied ceramic technology*, 3(2):94–104, 2006.

[59] Jeffrey I Eldridge, Charles M Spuckler, James A Nesbitt, and Richard E Martin. Nondestructive evaluation of thermal barrier coatings by mid-infrared reflectance imaging. *Advances in Ceramic Coatings and Ceramic-Metal Systems: Ceramic Engineering and Science Proceedings*, 26:121–128, 2005.

[60] Jeffrey I Eldridge and Douglas E Wolfe. Monitoring thermal barrier coating delamination progression by upconversion luminescence imaging. *Surface and Coatings Technology*, page 124923, 2019.

[61] Jeffrey I Eldridge, Dongming Zhu, and Douglas E Wolfe. Monitoring delamination of thermal barrier coatings during interrupted high-heat-flux laser testing using luminescence imaging. 2011.

[62] Remelisa Esteves, Johnathan Hernandez, Khanh Vo, Ryan Hoover, Gregory Freihofer, and Seetha Raghavan. Measurements for stress sensing of composites using tailored piezospectroscopic coatings. *AIP Advances*, 9(5):055201, 2019.

[63] AG Evans, MY He, and JW Hutchinson. Mechanics-based scaling laws for the durability of thermal barrier coatings. *Progress in materials science*, 46(3-4):249–271, 2001.

[64] AG Evans and JW Hutchinson. The mechanics of coating delamination in thermal gradients. *Surface and Coatings Technology*, 201(18):7905–7916, 2007.

[65] Joerg Peter Feist. *Development of phosphor thermometry for gas turbines.* PhD thesis, University of London, 2001.

[66] Jörg P Feist and Andrew L Heyes. Photo-stimulated phosphorescence for thermal condition monitoring and nondestructive evaluation in thermal barrier coatings. *Heat Transfer Engineering*, 30(13):1087–1095, 2009.

[67] JP Feist and AL Heyes. Europium-doped yttria-stabilized zirconia for high-temperature phosphor thermometry. *Proceedings of the Institution of Mechanical Engineers, Part L: Journal of Materials: Design and Applications*, 214(1):7–12, 2000.

[68] JP Feist, AL Heyes, KL Choy, and B Su. Phosphor thermometry for high temperature gas turbine applications. In *ICIASF 99. 18th International Congress on Instrumentation in Aerospace Simulation Facilities. Record (Cat. No. 99CH37025)*, pages 6–1. IEEE, 1999.

[69] JP Feist, AL Heyes, and S Seefelt. Thermographic phosphor thermometry for film cooling studies in gas turbine combustors. *Proceedings of the Institution of Mechanical Engineers, Part A: Journal of Power and Energy*, 217(2):193–200, 2003.

[70] JP Feist, S Karmakar Biswas, CC Pilgrim, PY Sollazzo, and S Berthier. Off-line temperature profiling utilizing phosphorescent thermal history paints and coatings. *Journal of Turbomachinery*, 137(10), 2015.

[71] JP Feist, PY Sollazzo, S Berthier, B Charnley, and J Wells. Precision temperature detection using a phosphorescence sensor coating system on a rolls-royce viper engine. In *ASME Turbo Expo 2012: Turbine Technical Conference and Exposition*, pages 917–926. American Society of Mechanical Engineers, 2012.

[72] Quentin Fouliard. Characterization of rare-earth doped thermal barrier coatings for phosphor thermometry. 2019.

[73] Quentin Fouliard, Ranajay Ghosh, and Seetha Raghavan. Quantifying thermal barrier coating delamination through luminescence modeling. *Surface and Coatings Technology*, 399:126153, 2020.

[74] Quentin Fouliard, Sandip Haldar, Ranajay Ghosh, and Seetha Raghavan. Modeling luminescence behavior for phosphor thermometry applied to doped thermal barrier coating configurations. *Applied Optics*, 58(13):D68–D75, 2019.

[75] Quentin Fouliard, Sandip Haldar, Ranajay Ghosh, and Seetha Raghavan. Modeling luminescence behavior for phosphor thermometry applied to doped thermal barrier coating configurations. *Applied Optics*, 58(13):D68–D75, 2019.

[76] Quentin Fouliard, Johnathan Hernandez, Hossein Ebrahimi, Khanh Vo, Ranajay Ghosh, Seetha Raghavan, Frank Accornero, Mary McCay, Jun-Sang Park, and Jonathan Almer. Synchrotron x-ray diffraction to quantify in-situ strain on rare-earth doped yttria-stabilized zirconia thermal barrier coatings. In *Turbo Expo: Power for Land, Sea, and Air*, volume 84997, page V006T02A006. American Society of Mechanical Engineers, 2021.

[77] Quentin Fouliard, Johnathan Hernandez, Bauke Heeg, Ranajay Ghosh, and Seetha Raghavan. Phosphor thermometry instrumentation for synchronized acquisition of luminescence lifetime decay and intensity on thermal barrier coatings. *Measurement Science and Technology*, 31(5):054007, 2020.

[78] Quentin P Fouliard, Ranajay Ghosh, and Seetha Raghavan. Doped 8% yttria stabilized zirconia for temperature measurements on thermal barrier coatings using phosphor thermometry. In *AIAA Scitech 2020 Forum*, page 0631, 2020.

[79] Quentin P Fouliard, Ranajay Ghosh, and Seetha Raghavan. Delamination of electron-beam physical-vapor deposition thermal barrier coatings using luminescent layers. In *AIAA Scitech 2021 Forum*, page 0432, 2021.

[80] AM Freborg, BL Ferguson, WJ Brindley, and GJ Petrus. Modeling oxidation induced stresses in thermal barrier coatings. *Materials Science and Engineering: A*, 245(2):182–190, 1998.

[81] Gregory Freihofer, Joshua Dustin, Hong Tat, Axel Schülzgen, and Seetha Raghavan. Stress and structural damage sensing piezospectroscopic coatings validated with digital image correlation. *Aip Advances*, 5(3):037139, 2015.

[82] Gregory Freihofer, Daniela Fugon-Dessources, Emrecan Ergin, Amy Van Newkirk, Ankur Gupta, Sudipta Seal, Axel Schulzgen, and Seetha Raghavan. Piezospectroscopic measurements capturing the evolution of plasma spray-coating stresses with substrate loads. *ACS applied materials & interfaces*, 6(3):1366–1369, 2014.

[83] Gregory Freihofer, Axel Schülzgen, and Seetha Raghavan. Damage mapping with a degrading elastic modulus using piezospectroscopic coatings. *NDT & E International*, 75:65–71, 2015.

[84] N Fuhrmann, J Brübach, and A Dreizler. Phosphor thermometry: a comparison of the luminescence lifetime and the intensity ratio approach. *Proceedings of the Combustion Institute*, 34(2):3611–3618, 2013.

[85] Mathias C Galetz. Coatings for superalloys. In *Superalloys*, pages 277–298. InTech, 2015.

[86] Maurice Gell, Swetha Sridharan, Mei Wen, and Eric H Jordan. Photoluminescence piezospectroscopy: A multi-purpose quality control and ndi technique for thermal barrier coatings. *International Journal of Applied Ceramic Technology*, 1(4):316–329, 2004.

[87] Maurice Gell, Jiwen Wang, Rishi Kumar, Jeffery Roth, Chen Jiang, and Eric H Jordan. Higher temperature thermal barrier coatings with the combined use of yttrium aluminum garnet and the solution precursor plasma spray process. *Journal of Thermal Spray Technology*, pages 1–13, 2018.

[88] MM Gentleman and DR Clarke. Concepts for luminescence sensing of thermal barrier coatings. *Surface and coatings technology*, 188:93–100, 2004.

[89] MM Gentleman, JI Eldridge, DM Zhu, KS Murphy, and DR Clarke. Non-contact sensing of TBC/BC interface temperature in a thermal gradient. *Surface and Coatings Technology*, 201(7):3937–3941, 2006.

[90] Molly Gentleman and David Clarke. Embedded optical sensors for thermal barrier coatings. *Technical Report 2004-12-16*, 2004.

[91] Molly M. Gentleman, Vanni Lughi, John A. Nychka, and David R. Clarke. Non-contact methods for measuring thermal barrier coating temperatures. *International Journal of Applied Ceramic Technology*, (2):105, 2006.

[92] Anindya Ghoshal, Muthuvel Murugan, Michael J Walock, Andy Nieto, Blake D Barnett, Marc S Pepi, Jeffrey J Swab, Dongming Zhu, Kevin A Kerner, Christopher R Rowe, et al. Molten particulate impact on tailored thermal barrier coatings for gas turbine engine. *Journal of Engineering for Gas Turbines and Power*, 140(2), 2018.

[93] A Yañez Gonzalez, CC Pilgrim, PY Sollazzo, AL Heyes, JP Feist, JR Nicholls, and F Beyrau. Temperature sensing inside thermal barrier coatings using phosphor thermometry. 2014.

[94] L González-Fernández, L Del Campo, RB Pérez-Sáez, and MJ Tello. Normal spectral emittance of inconel 718 aeronautical alloy coated with yttria stabilized zirconia films. *Journal of Alloys and Compounds*, 513:101–106, 2012.

[95] Brian Good. Kinetic monte carlo simulation of oxygen and cation diffusion in yttria-stabilized zirconia. 2011.

[96] Santosh K Gupta, C Reghukumar, K Sudarshan, PS Ghosh, Nimai Pathak, and RM Kadam. Orange-red emitting gd2zr2o7: Sm3+: Structure-property correlation, optical properties and defect spectroscopy. *Journal of Physics and Chemistry of Solids*, 116:360–366, 2018.

[97] Sandip Haldar, Peter Warren, Quentin Fouliard, David Moreno, Mary McCay, Jun Sang Park, Peter Kenesei, Jonathan Almer, Ranajay Ghosh, and Seetha Raghavan. Synchrotron xrd measurements of thermal barrier coating configurations with rare earth elements for phosphor thermometry. In *Turbo Expo: Power for Land, Sea, and Air*, volume 58677, page V006T24A014. American Society of Mechanical Engineers, 2019.

[98] AP Hammersley et al. Fit2d: an introduction and overview. *European synchrotron radiation facility internal report ESRF97HA02T*, 68:58, 1997.

[99] I Hanhan, E Durnberg, G Freihofer, P Akin, and S Raghavan. Portable piezospectroscopy system: non-contact in-situ stress sensing through high resolution photoluminescent mapping. *Journal of Instrumentation*, 9(11):P11005, 2014.

[100] Rachael Ann Hansel. *Phosphor thermometry using rare-earth doped materials*. Vanderbilt University, 2010.

[101] CL Hardin, Y Kodera, SA Basun, DR Evans, and JE Garay. Transparent, luminescent terbium doped zirconia: development of optical-structural ceramics with integrated temperature measurement functionalities. *Optical Materials Express*, 3(6):893–903, 2013.

[102] A Hashemi, A Vetter, G Jovicic, M Batentschuk, and CJ Brabec. Temperature measurements using yag: Dy and yag: Sm under diode laser excitation (405 nm). *Measurement Science and Technology*, 26(7):075202, 2015.

[103] Viktor Hauk. *Structural and residual stress analysis by nondestructive methods: Evaluation-Application-Assessment*. Elsevier, 1997.

[104] J Allen Haynes, MK Ferber, and WD Porter. Thermal cycling behavior of plasma-sprayed thermal barrier coatings with various mcralx bond coats. *Journal of Thermal Spray Technology*, 9(1):38–48, 2000.

[105] Bob Baoping He. Introduction to two-dimensional x-ray diffraction. *Powder diffraction*, 18(2):71–85, 2003.

[106] B Heeg and TP Jenkins. Precision and accuracy of luminescence lifetime-based phosphor thermometry: A case study of eu (iii): Ysz. In *AIP Conference Proceedings*, volume 1552, pages 885–890. AIP, 2013.

[107] Bauke Heeg, Vladimir K Tolpygo, and David R Clarke. Damage evolution in thermal barrier coatings with thermal cycling. *Journal of the American Ceramic Society*, 94(s1), 2011.

[108] Ellen Hertle, Liudmyla Chepyga, Miroslaw Batentschuk, Stefan Will, and Lars Zigan. Temperature-dependent luminescence characteristics of dy 3+ doped in various crystalline hosts. *Journal of Luminescence*, 204, 07 2018.

[109] Ellen Hertle, Liudmyla Chepyga, Miroslaw Batentschuk, and Lars Zigan. Influence of codoping on the luminescence properties of yag: Dy for high temperature phosphor thermometry. *Journal of Luminescence*, 182:200–207, 2017.

[110] AL Heyes. On the design of phosphors for high-temperature thermometry. *Journal of Luminescence*, 129(12):2004–2009, 2009.

[111] AL Heyes, JP Feist, X Chen, Z Mutasim, and JR Nicholls. Optical nondestructive condition monitoring of thermal barrier coatings. *Journal of Engineering for Gas Turbines and Power*, 130(6):061301, 2008.

[112] AL Heyes, A Rabhiou, JP Feist, and A Kempf. Thermal history sensing with thermographic phosphors. In *AIP Conference Proceedings*, volume 1552, pages 891–896. AIP, 2013.

[113] Mohsen Jahanmiri. Pressure sensitive paints: the basics & applications. Technical report, Chalmers University of Technology, 2011.

[114] Suwatwong Janchaysang, Sarun Sumriddetchkajorn, and Prathan Buranasiri. Tunable filter-based multispectral imaging for detection of blood stains on construction material substrates. part 1. developing blood stain discrimination criteria. *Applied Optics*, 51(29):6984–6996, 2012.

[115] Peter D Johnson and Ferd E Williams. The interpretation of the dependence of luminescent efficiency on activator concentration. *The Journal of Chemical Physics*, 18(11):1477–1483, 1950.

[116] Peter D Johnson and Ferd E Williams. Specific magnetic susceptibilities and related properties of manganese-activated zinc fluoride. *The Journal of Chemical Physics*, 18(3):323–326, 1950.

[117] Anette M Karlsson, JW Hutchinson, and AG Evans. The displacement of the thermally grown oxide in thermal barrier systems upon temperature cycling. *Materials Science and Engineering: A*, 351(1-2):244–257, 2003.

[118] Matthew J Kelly, Douglas E Wolfe, Jogender Singh, Jeff Eldridge, Dong-Ming Zhu, and Robert Miller. Thermal barrier coatings design with increased reflectivity and

lower thermal conductivity for high-temperature turbine applications. *International journal of applied ceramic technology*, 3(2):81–93, 2006.

[119] Clive Kerr and Paul Ivey. An overview of the measurement errors associated with gas turbine aeroengine pyrometer systems. *Measurement science and technology*, 13(6):873, 2002.

[120] AH Khalid and K Kontis. Quantum efficiencies, absolute intensities and signal-to-blackbody ratios of high-temperature laser-induced thermographic phosphors. *Luminescence*, 26(6):640–649, 2011.

[121] AH Khalid, K Kontis, and HZ Behtash. Phosphor thermometry in gas turbines: consideration factors. *Proceedings of the Institution of Mechanical Engineers, Part G: Journal of Aerospace Engineering*, 224(7):745–755, 2010.

[122] Ashiq Hussain Khalid. *Development of phosphor thermometry systems for use in development gas turbine engines*. PhD thesis, University of Manchester, 2011.

[123] Ashiq Hussain Khalid and Konstantinos Kontis. Thermographic phosphors for high temperature measurements: principles, current state of the art and recent applications. *Sensors*, 8(9):5673–5744, 2008.

[124] A Nusair Khan, J Lu, and H Liao. Effect of residual stresses on air plasma sprayed thermal barrier coatings. *Surface and Coatings Technology*, 168(2-3):291–299, 2003.

[125] Christoph Knappe. *Phosphor Thermometry on Surfaces-A Study of its Methodology and its Practical Applications*. 2013.

[126] Kevin Knipe, Albert C Manero, Stephen Sofronsky, John Okasinski, Jonathan Almer, Janine Wischek, Carla Meid, Anette Karlsson, Marion Bartsch, and Seetha Raghavan. Synchrotron x-ray diffraction measurements mapping internal strains of thermal barrier coatings during thermal gradient mechanical fatigue loading. *Journal of Engineering for Gas Turbines and Power*, 137(8):082506, 2015.

[127] Kevin Knipe, Albert Manero II, Sanna F Siddiqui, Carla Meid, Janine Wischek, John Okasinski, Jonathan Almer, Anette M Karlsson, Marion Bartsch, and Seetha Raghavan. Strain response of thermal barrier coatings captured under extreme engine environments through synchrotron X-ray diffraction. *Nature Communications*, 5:4559, 2014.

[128] Ki-Young Ko, Young Kwang Lee, Hoo Keun Park, Yoon-Chang Kim, and Young Rag Do. The variation of the enhanced photoluminescence efficiency of y 2 o 3: Eu 3+ films with the thickness to the photonic crystal layer. *Optics express*, 16(8):5689–5696, 2008.

[129] Philip Kosky, Robert T Balmer, William D Keat, and George Wise. *Exploring engineering: an introduction to engineering and design*. Academic Press, 2015.

[130] Ali Ghaseminezhad Koushali, Mahmood Sameezadeh, Majid Vaseghi, and Pedram Safarpour. Analytical and numerical investigations of the crack behavior in thermal barrier coatings under the trip thermal load. *Surface and Coatings Technology*, 337:90–96, 2018.

[131] Jennifer DT Kruschwitz and Roy S Berns. First-order goniospectrophotometric spectral modeling of isotropic and anisotropic colorant mixtures. *Applied Optics*, 53(4):A131–A141, 2014.

[132] Paul Kubelka. New contributions to the optics of intensely light-scattering materials. part i. *JOSA*, 38(5):448–457, 1948.

[133] Paul Kubelka. New contributions to the optics of intensely light-scattering materials. part ii: Nonhomogeneous layers. *JOSA*, 44(4):330–335, 1954.

[134] Anand Kulkarni, A Vaidya, A Goland, S Sampath, and H Herman. Processing effects on porosity-property correlations in plasma sprayed yttria-stabilized zirconia coatings. *Materials Science and Engineering: A*, 359(1-2):100–111, 2003.

[135] Hideo Kusama, Ojars J Sovers, and Taisuke Yoshioka. Line shift method for phosphor temperature measurements. *Japanese Journal of Applied Physics*, 15(12):2349, 1976.

[136] Myung-Jae Lee, Byung-Chai Lee, Jang-Gyun Lim, and Moon-Ki Kim. Residual stress analysis of the thermal barrier coating system by considering the plasma spraying process. *Journal of Mechanical Science and Technology*, 28(6):2161–2168, 2014.

[137] Woo Y Lee, David P Stinton, Christopher C Berndt, Fazil Erdogan, Yi-Der Lee, and Zaher Mutasim. Concept of functionally graded materials for advanced thermal barrier coating applications. *Journal of the American Ceramic Society*, 79(12):3003–3012, 1996.

[138] YW Lee, JS Chang, Shyamal Das, A Dhar, Mrinmoy Pal, Mukul Chandra Paul, JT Lin, and YW Jhang. Er^{3+}-doped nanoengineered yttria-stabilized zirconia alumino-silicate fiber for efficient cw and mode-locked laser operation. *IEEE Photonics Journal*, 8(4):1–13, 2016.

[139] C Lempereur, R Andral, and JY Prudhomme. Surface temperature measurement on engine components by means of irreversible thermal coatings. *Measurement Science and Technology*, 19(10):105501, 2008.

[140] Chun Li, Xun Zhang, Ying Chen, James Carr, Simon Jacques, Julia Behnsen, Marco Di Michiel, Ping Xiao, and Robert Cernik. Understanding the residual stress distribution through the thickness of atmosphere plasma sprayed (aps) thermal barrier coatings (tbcs) by high energy synchrotron xrd; digital image correlation (dic) and image based modelling. *Acta materialia*, 132:1–12, 2017.

[141] Chunling Li, Xueling Fan, Peng Jiang, and Xiaochao Jin. Delamination-indicating of atmosphere-plasma-sprayed thermal barrier coating system using eu 3+ luminescence mapping. *Materials Letters*, 2018.

[142] Li Li and David R Clarke. Effect of cmas infiltration on radiative transport through an eb-pvd thermal barrier coating. *International journal of applied ceramic technology*, 5(3):278–288, 2008.

[143] Geunsik Lim and Aravinda Kar. Radiative properties of thermal barrier coatings at high temperatures. *Journal of Physics D: Applied Physics*, 42(15):155412, 2009.

[144] Andi M Limarga and David R Clarke. Characterization of electron beam physical vapor-deposited thermal barrier coatings using diffuse optical reflectance. *International Journal of Applied Ceramic Technology*, 6(3):400–409, 2009.

[145] Guido Lipiak, S Bussmann, C Steinwachs, and A Luttenberg. Lifetime extension for siemens gas turbines. In *Power Gen Europe*, 2006.

[146] Jing Liu. Mechanisms of lifetime improvement in thermal barrier coatings with hf and/or y modification of cmsx-4 superalloy substrates. 2007.

[147] Yanfa Liu, Longfei Chang, Ying Hu, Qingzheng Niu, Linfeng Yu, Yanjie Wang, Pin Lu, and Yucheng Wu. Rough interface in IPMC: modeling and its influence analysis. *Smart Materials and Structures*, 27(7):075055, 2018.

[148] Yankuan Liu, Yinghui Liu, Philippe Lours, Thierry Sentenac, Vanessa Vidal, Zhiping Wang, and Kunying Ding. Influence of isothermal aging conditions on aps tbc's interfacial fracture toughness. *Surface and Coatings Technology*, 313:417–424, 2017.

[149] Vesna Lojpur, Sanja Ćulubrk, Mina Medić, and Miroslav Dramicanin. Luminescence thermometry with eu3+ doped gdalo3. *Journal of Luminescence*, 170:467–471, 2016.

[150] AJG Lunt, MY Xie, N Baimpas, SY Zhang, S Kabra, J Kelleher, TK Neo, and AM Korsunsky. Calculations of single crystal elastic constants for yttria partially stabilised zirconia from powder diffraction data. *Journal of Applied Physics*, 116(5):053509, 2014.

[151] Mark Steven Majewski. *Optical Diagnostics of Thermal Barrier Coatings*. University of Connecticut, 2010.

[152] J Manara, M Arduini, and J Hartmann. A novel approach for non-destructive testing of the adhesion of thermal barrier coatings.

[153] J Manara, M Zipf, T Stark, M Arduini, H-P Ebert, A Tutschke, A Hallam, J Hanspal, M Langley, D Hodge, et al. Long wavelength infrared radiation thermometry for non-contact temperature measurements in gas turbines. *Infrared Physics & Technology*, 80:120–130, 2017.

[154] Albert Manero, Kevin Knipe, Janine Wischek, Carla Meid, John Okasinski, Jonathan Almer, Anette Karlsson, Marion Bartsch, and Seetha Raghavan. Capturing the competing influence of thermal and mechanical loads on the strain of turbine blade coatings via high energy x-rays. *Coatings*, 8(9):320, 2018.

[155] Albert Manero, Stephen Sofronsky, Kevin Knipe, Carla Meid, Janine Wischek, John Okasinski, Jonathan Almer, Anette M Karlsson, Seetha Raghavan, and Marion Bartsch. Monitoring local strain in a thermal barrier coating system under thermal mechanical gas turbine operating conditions. *JOM*, 67(7):1528–1539, 2015.

[156] Albert Manero II, Alex Selimov, Quentin Fouliard, Kevin Knipe, Janine Wischek, Carla Meid, Anette M Karlsson, Marion Bartsch, and Seetha Raghavan. Piezospectroscopic evaluation and damage identification for thermal barrier coatings subjected to simulated engine environments. *Surface and Coatings Technology*, 323:30–38, 2017.

[157] Thorsten Manns and Berthold Scholtes. Deccalc - a program for the calculation of diffraction elastic constants from single crystal coefficients. In *Residual Stresses VIII*, volume 681 of *Materials Science Forum*, pages 417–419. Trans Tech Publications, 5 2011.

[158] JR Markham and K Kinsella. Thermal radiative properties and temperature measurement from turbine coatings. *International journal of thermophysics*, 19(2):537–545, 1998.

[159] J Matejicek, S Sampath, PC Brand, and HJ Prask. Quenching, thermal and residual stress in plasma sprayed deposits: Nicraly and ysz coatings. *Acta Materialia*, 47(2):607–617, 1999.

[160] Serge Mazauric, Mathieu Hébert, Lionel Simonot, and Thierry Fournel. Two-flux transfer matrix model for predicting the reflectance and transmittance of duplex halftone prints. *JOSA A*, 31(12):2775–2788, 2014.

[161] Chao Mi, Jianhong Wu, Yanmin Yang, Boning Han, and Jun Wei. Efficient upconversion luminescence from ba 5 gd 8 zn 4 o 21: Yb 3+, er 3+ based on a demonstrated cross-relaxation process. *Scientific reports*, 6:22545, 2016.

[162] Safer Mourad. Improved calibration of optical characteristics of paper by an adapted paper-mtf model. *Journal of Imaging Science and Technology*, 51(4):283–292, 2007.

[163] Michael L Myrick, Michael N Simcock, Megan Baranowski, Heather Brooke, Stephen L Morgan, and Jessica N McCutcheon. The kubelka-munk diffuse reflectance formula revisited. *Applied Spectroscopy Reviews*, 46(2):140–165, 2011.

[164] Fahed Abou Nada, Andreas Lantz, Jenny Larfeldt, Nicolaie Markocsan, Marcus Aldén, and Mattias Richter. Remote temperature sensing on and beneath atmospheric plasma sprayed thermal barrier coatings using thermographic phosphors. *Surface and Coatings Technology*, 302:359–367, 2016.

[165] E Nakazawa, S Shionoya, and WM Yen. Phosphor handbook. *CRC Press, Boca Raton, Boston, London, New York, Washington, DC*, page 102, 1999.

[166] N Nayebpashaee, SH Seyedein, MR Aboutalebi, H Sarpoolaky, and SMM Hadavi. Finite element simulation of residual stress and failure mechanism in plasma sprayed thermal barrier coatings using actual microstructure as the representative volume. *Surface and Coatings Technology*, 291:103–114, 2016.

[167] John R Nicholls, KJ Lawson, A Johnstone, and DS Rickerby. Methods to reduce the thermal conductivity of eb-pvd tbcs. *Surface and Coatings Technology*, 151:383–391, 2002.

[168] John R Nicholls, Richard G Wellman, Remy Steenbakker, and Jörg Feist. Self diagnostic eb-pvd thermal barrier coatings. In *Advances in Science and Technology*, volume 72, pages 65–74. Trans Tech Publ, 2010.

[169] Ismail C Noyan and Jerome B Cohen. *Residual stress: measurement by diffraction and interpretation*. Springer, 2013.

[170] Nitin P Padture, Maurice Gell, and Eric H Jordan. Thermal barrier coatings for gas-turbine engine applications. *Science*, 296(5566):280–284, 2002.

[171] JGJ Peelen and R Metselaar. Light scattering by pores in polycrystalline materials: Transmission properties of alumina. *Journal of Applied Physics*, 45(1):216–220, 1974.

[172] Xiao Peng and David R Clarke. Piezospectroscopic analysis of interface debonding in thermal barrier coatings. *Journal of the American Ceramic Society*, 83(5):1165–1170, 2000.

[173] Johan Petit. *Monocristaux dopés ytterbium et matériaux assemblés pour lasers de fortes puissances*. PhD thesis, Paris 6, 2006.

[174] Frank E Pfefferkorn, Frank P Incropera, and Yung C Shin. Surface temperature measurement of semi-transparent ceramics by long-wavelength pyrometry. In *ASME 2002 International Mechanical Engineering Congress and Exposition*, pages 137–146. American Society of Mechanical Engineers Digital Collection, 2008.

[175] C. C. Pilgrim, P. Y. Sollazzo, S. Berthier, J. P. Feist, S. K. Biswas, and J. R. Nicholls. Thermal barrier sensor coatings - sensing damage and ageing in critical components. In *IET ISA 60th International Instrumentation Symposium 2014*, pages 1–8, June 2014.

[176] CC Pilgrim, JP Feist, and AL Heyes. On the effect of temperature gradients and coating translucence on the accuracy of phosphor thermometry. *Measurement Science and Technology*, 24(10):105201, 2013.

[177] Christopher Pilgrim, Alvaro Yañez Gonzalez, Raffaele Saggese, Robert Krewinkel, Michael Blaswich, Jörg Feist, Ulrich Orth, Michael Rabs, Dirk Frank, and Silvia Araguas Rodriguez. Surface temperature measurements in an industrial gas turbine using thermal history paints. In *12 th European Conference on Turbomachinery Fluid dynamics & Thermodynamics*. EUROPEAN TURBOMACHINERY SOCIETY, 2017.

[178] Christopher Charles Pilgrim. Luminescence for the non-destructive evaluation of thermal barrier coatings. 2014.

[179] Lisa Pin, Christopher Pilgrim, Jörg Feist, Yannick Le Maoult, Florence Ansart, and Philippe Lours. Characterisation of thermal barrier sensor coatings synthesised by sol–gel route. *Sensors and Actuators A: Physical*, 199:289–296, 2013.

[180] Pierre Planques, Vanessa Vidal, Philippe Lours, Vincent Proton, Fabrice Crabos, Julitte Huez, and Bernard Viguier. Mechanical and thermo-physical properties of plasma-sprayed thermal barrier coatings: a literature survey. *Oxidation of Metals*, 88(1-2):133–143, 2017.

[181] Liu Qu, Kwang-Leong Choy, and Richard Wheatley. Theoretical and experimental studies of doping effects on thermodynamic properties of (dy, y)-zro2. *Acta Materialia*, 114:7–14, 2016.

[182] Mihailo D Rabasović, Branka D Murić, Vladan Čelebonović, Miodrag Mitrić, Branislav M Jelenković, and Marko G Nikolić. Luminescence thermometry via the two-dopant intensity ratio of y2o3: Er3+, eu3+. *Journal of Physics D: Applied Physics*, 49(48):485104, 2016.

[183] A Rabhiou, A Kempf, and A Heyes. Examination of eu-doped thermographic phosphors for surface temperature measurements. In *European Combustion Meeting, Vienna, Austria*. Citeseer, 2009.

[184] AGEA Rabiei and AG Evans. Failure mechanisms associated with the thermally grown oxide in plasma-sprayed thermal barrier coatings. *Acta materialia*, 48(15):3963–3976, 2000.

[185] M Rezvani Rad, GH Farrahi, M Azadi, and M Ghodrati. Effects of preheating temperature and cooling rate on two-step residual stress in thermal barrier coatings considering real roughness and porosity effect. *Ceramics International*, 40(10):15925–15940, 2014.

[186] R Rajendran, Vijay Petley, and Birgit Rehmer. Dynamic elastic properties of aeroengine metallic isotropic materials. *Proceedings of the Institution of Mechanical Engineers, Part L: Journal of Materials: Design and Applications*, 227(3):243–249, 2013.

[187] Prabhu Ramanujam. *Synthesis and processing of nanocrystalline YAG (Yttrium Aluminium Garnet) ceramics*. PhD thesis, © Prabhu Ramanujam, 2014.

[188] DD Ramteke, A Balakrishna, Vijay Kumar, and HC Swart. Luminescence dynamics and investigation of judd-ofelt intensity parameters of Sm^{3+} ion containing glasses. *Optical Materials*, 64:171–178, 2017.

[189] M Ranjbar-Far, Joseph Absi, Gilles Mariaux, and Salman Shahidi. Effect of residual stresses and prediction of possible failure mechanisms on thermal barrier coating

system by finite element method. *Journal of thermal spray technology*, 19(5):1054–1061, 2010.

[190] H-J Rätzer-Scheibe, U Schulz, and T Krell. The effect of coating thickness on the thermal conductivity of eb-pvd pysz thermal barrier coatings. *Surface and Coatings Technology*, 200(18-19):5636–5644, 2006.

[191] Majid Rezazadeh Reyhani, Mohammad Alizadeh, Alireza Fathi, and Hiwa Khaledi. Turbine blade temperature calculation and life estimation-a sensitivity analysis. *Propulsion and power Research*, 2(2):148–161, 2013.

[192] J Rösler, M Bäker, and K Aufzug. A parametric study of the stress state of thermal barrier coatings: Part i: creep relaxation. *Acta materialia*, 52(16):4809–4817, 2004.

[193] J Rösler, M Bäker, and M Volgmann. Stress state and failure mechanisms of thermal barrier coatings: role of creep in thermally grown oxide. *Acta Materialia*, 49(18):3659–3670, 2001.

[194] Lin Rossmann, Matthew Northam, Brooke Sarley, Liudmila Chernova, Vaishak Viswanathan, Bryan Harder, and Seetha Raghavan. Investigation of tgo stress in thermally cycled plasma-spray physical vapor deposition and electron-beam physical vapor deposition thermal barrier coatings via photoluminescence spectroscopy. *Surface and Coatings Technology*, page 125047, 2019.

[195] J Ruud, YC Lau, and V Kwasniewski. Increased fuel efficiency and decreased emissions through tbcs. *Published in Performance of the Third*, 50:950–4, 2003.

[196] Christopher Sandoval and Arnold D Kim. Extending generalized Kubelka–Munk to three-dimensional radiative transfer. *Applied Optics*, 54(23):7045–7053, 2015.

[197] Caroline A Schneider, Wayne S Rasband, and Kevin W Eliceiri. Nih image to imagej: 25 years of image analysis. *Nature methods*, 9(7):671–675, 2012.

[198] U Schulz and M Schmücker. Microstructure of zro2 thermal barrier coatings applied by eb-pvd. *Materials Science and Engineering: A*, 276(1-2):1–8, 2000.

[199] Uwe Schulz, Bilge Saruhan, Klaus Fritscher, and Christoph Leyens. Review on advanced eb-pvd ceramic topcoats for tbc applications. *International journal of applied ceramic technology*, 1(4):302–315, 2004.

[200] H.C. Seat and J.H. Sharp. Dedicated temperature sensing with>tex<c>/tex<-axis oriented single-crystal ruby>tex<($rmcr^3+ : rmal_2rmo_3$)>/tex<fibers: Temperature and strain dependences of r-line fluorescence. *Instrumentation and Measurement, IEEE Transactions on*, 53:140 – 154, 03 2004.

[201] Max Seyfried and Leonid Fukshansky. Light gradients in plant tissue. *Applied Optics*, 22(9):1402–1408, 1983.

[202] Y Shen, MD Chambers, and DR Clarke. Effects of dopants and excitation wavelength on the temperature sensing of Ln^{3+}-doped 7YSZ. *Surface and Coatings Technology*, 203(5-7):456–460, 2008.

[203] Yang Shen and David R Clarke. Effects of reducing atmosphere on the luminescence of eu3+-doped yttria-stabilized zirconia sensor layers in thermal barrier coatings. *Journal of the American Ceramic Society*, 92(1):125–129, 2009.

[204] Yang Shen, Xing Wang, Hongcai He, Yuanhua Lin, and Ce-Wen Nan. Effects of sm3+ doping on the temperature-dependent fluorescence intensity ratio of er3+, sm3+-co

doped-yttria stabilized zirconia. *Journal of Alloys and Compounds*, 536:161–165, 2012.

[205] Sanna F Siddiqui, Kevin Knipe, Albert Manero, Carla Meid, Janine Wischek, John Okasinski, Jonathan Almer, Anette M Karlsson, Marion Bartsch, and Seetha Raghavan. Synchrotron x-ray measurement techniques for thermal barrier coated cylindrical samples under thermal gradients. *Review of Scientific Instruments*, 84(8):083904, 2013.

[206] R. Siegel and J. R. Howell. *Thermal Radiation Heat Transfer, 4th Edition*. Taylor & Francis, New York, 2002.

[207] Riti Singh and FIMechE CEng. Civil aero gas turbines: Technology & strategy. *Aero India*, 2003.

[208] P Skalka, K Slámečka, J Pokluda, and L Čelko. Finite element simulation of stresses in a plasma-sprayed thermal barrier coating with a crack at the tgo/bond-coat interface. *Surface and Coatings Technology*, 337:321–334, 2018.

[209] SJ Skinner, JP Feist, IJE Brooks, S Seefeldt, and AL Heyes. Yag: Ysz composites as potential thermographic phosphors for high temperature sensor applications. *Sensors and Actuators B: Chemical*, 136(1):52–59, 2009.

[210] Ramazan Sobhanverdi and Alireza Akbari. Porosity and microstructural features of plasma sprayed yttria stabilized zirconia thermal barrier coatings. *Ceramics International*, 41(10):14517–14528, 2015.

[211] CM Spuckler and R Siegel. Refractive index and scattering effects on radiative behavior of a semitransparent layer. *Journal of Thermophysics and Heat transfer*, 7(2):302–310, 1993.

[212] Stephan Stecura. Optimization of the nicral-y/zro-y2o3 thermal barrier system. Technical report, National Aeronautics and Space Administration, 1985.

[213] RÃŠmy JL Steenbakker, JÃļrg P Feist, Richard G Wellman, and John R Nicholls. Sensor thermal barrier coatings: Remote in situ condition monitoring of eb-pvd coatings at elevated temperatures. *Journal of Engineering for Gas Turbines and Power*, 131(4):041301, 2009.

[214] Remy Steenbakker. Phosphor thermometry in an eb-pvd tbc. 2008.

[215] Amanda Stevenson, Ashley Jones, and Seetha Raghavan. Stress-sensing nanomaterial calibrated with photostimulated luminescence emission. *Nano letters*, 11(8):3274–3278, 2011.

[216] A Stuke, H Kassner, J-L Marqués, R Vassen, D Stöver, and R Carius. Suspension and air plasma-sprayed ceramic thermal barrier coatings with high infrared reflectance. *International Journal of Applied Ceramic Technology*, 9(3):561–574, 2012.

[217] YJ Su, RW Trice, KT Faber, H Wang, and WD Porter. Thermal conductivity, phase stability, and oxidation resistance of y 3 al 5 o 12 (yag)/y 2 o 3–zro 2 (ysz) thermal-barrier coatings. *Oxidation of metals*, 61(3-4):253–271, 2004.

[218] JG Sun. Nondestructive evaluation of thermal barrier coatings by optical and thermal imaging methods. *Mechanical Properties and Performance of Engineering Ceramics and Composites VII*, pages 27–34, 2012.

[219] Yang Tan, Jon P Longtin, Sanjay Sampath, and Dongming Zhu. Temperature-gradient effects in thermal barrier coatings: An investigation through modeling, high

heat flux test, and embedded sensor. *Journal of the American Ceramic Society*, 93(10):3418–3426, 2010.

[220] V Teixeira, M Andritschky, W Fischer, HP Buchkremer, and D Stöver. Effects of deposition temperature and thermal cycling on residual stress state in zirconia-based thermal barrier coatings. *Surface and Coatings Technology*, 120:103–111, 1999.

[221] Juddha Thapa, Bo Liu, Steven D Woodruff, Benjamin T Chorpening, and Michael P Buric. Raman scattering in single-crystal sapphire at elevated temperatures. *Applied optics*, 56(31):8598–8606, 2017.

[222] J Thornton, S Slater, and J Almer. The measurement of residual strains within thermal barrier coatings using high-energy x-ray diffraction. *Journal of the American Ceramic Society*, 88(10):2817–2825, 2005.

[223] Lawrence Tinsley, Christine Chalk, John Nicholls, Jörn Mehnen, and Rajkumar Roy. A study of pulsed thermography for life assessment of thin eb-pvd tbcs undergoing oxidation ageing. *NDT & E International*, 92:67–74, 2017.

[224] SA Tsipas. Effect of dopants on the phase stability of zirconia-based plasma sprayed thermal barrier coatings. *Journal of the European Ceramic Society*, 30(1):61–72, 2010.

[225] Frederick K von Willisen et al. Frustrated total internal reflection and application of its principle to laser cavity design. *Applied Optics*, 3(6):719–726, 1964.

[226] Zoltán Vörös and Rainer Johnsen. A simple demonstration of frustrated total internal reflection. *American journal of physics*, 76(8):746–749, 2008.

[227] L Wang, XH Zhong, YX Zhao, SY Tao, W Zhang, Y Wang, and XG Sun. Design and optimization of coating structure for the thermal barrier coatings fabricated by atmospheric plasma spraying via finite element method. *Journal of Asian Ceramic Societies*, 2(2):102–116, 2014.

[228] Li Wang, Jeffrey I Eldridge, and SM Guo. Comparison of different models for the determination of the absorption and scattering coefficients of thermal barrier coatings. *Acta Materialia*, 64:402–410, 2014.

[229] Peter Warren, Sandip Haldar, Seetha Raghavan, and Ranajay Ghosh. Modeling thermally grown oxides in thermal barrier coatings using koch fractal. In *Turbo Expo: Power for Land, Sea, and Air*, volume 58677, page V006T24A019. American Society of Mechanical Engineers, 2019.

[230] Mei Wen, Eric H Jordan, and Maurice Gell. Analysis of localized damage in eb-pvd/(ni, pt) al thermal barrier coatings. *Surface and Coatings Technology*, 200(18-19):5193–5202, 2006.

[231] Mei Wen, Eric H Jordan, and Maurice Gell. Remaining life prediction of thermal barrier coatings based on photoluminescence piezospectroscopy measurements. 2006.

[232] CM Weyant, J Almer, and KT Faber. Through-thickness determination of phase composition and residual stresses in thermal barrier coatings using high-energy x-rays. *Acta materialia*, 58(3):943–951, 2010.

[233] Sujanto Widjaja, Andi M Limarga, and Tick Hon Yip. Modeling of residual stresses in a plasma-sprayed zirconia/alumina functionally graded-thermal barrier coating. *Thin Solid Films*, 434(1-2):216–227, 2003.

[234] Dustin Witkowski and David A Rothamer. A methodology for identifying thermographic phosphors suitable for high-temperature gas thermometry: application to ce3+ and pr3+ doped oxide hosts. *Applied Physics B*, 123(8):226, 2017.

[235] Douglas E Wolfe, Jogender Singh, Robert A Miller, Jeff I Eldridge, and Dong-Ming Zhu. Tailored microstructure of eb-pvd 8ysz thermal barrier coatings with low thermal conductivity and high thermal reflectivity for turbine applications. *Surface and Coatings Technology*, 190(1):132–149, 2005.

[236] Heping Xie and Jin-an Wang. Direct fractal measurement of fracture surfaces. *International Journal of Solids and Structures*, 36(20):3073–3084, 1999.

[237] NM Yanar, M Helminiak, GH Meier, and FS Pettit. Comparison of the failures during cyclic oxidation of yttria-stabilized (7 to 8 weight percent) zirconia thermal barrier coatings fabricated via electron beam physical vapor deposition and air plasma spray. *Metallurgical and Materials Transactions A*, 42(4):905–921, 2011.

[238] A Yañez Gonzalez, CC Pilgrim, JP Feist, PY Sollazzo, F Beyrau, and AL Heyes. Online temperature measurement inside a thermal barrier sensor coating during engine operation. *Journal of Turbomachinery*, 137(10), 2015.

[239] Alvaro Yañez Gonzalez. Phosphorescent thermal history sensors for extreme environments. 2015.

[240] G Yang and CY Zhao. A comparative experimental study on radiative properties of eb-pvd and air plasma sprayed thermal barrier coatings. *Journal of Heat Transfer*, 137(9):091024, 2015.

[241] G Yang and CY Zhao. Infrared radiative properties of eb-pvd thermal barrier coatings. *International Journal of Heat and Mass Transfer*, 94:199–210, 2016.

[242] Lixia Yang, Di Peng, Chunshan Zhao, Chen Xing, Fangwei Guo, Zhiqi Yao, Yingzheng Liu, Xiaofeng Zhao, and Ping Xiao. Evaluation of the in-depth temperature sensing performance of eu-and dy-doped ysz in air plasma sprayed thermal barrier coatings. *Surface and Coatings Technology*, 316:210–218, 2017.

[243] Lixia Yang, Fan Yang, Ying Long, Yang Zhao, Xiang Xiong, Xiaofeng Zhao, and Ping Xiao. Evolution of residual stress in air plasma sprayed yttria stabilised zirconia thermal barrier coatings after isothermal treatment. *Surface and Coatings Technology*, 251:98–105, 2014.

[244] HUI Yu, ZHAO Sumei, XU Jiaying, ZHU Ling, ZHOU Xin, ZOU Binglin, WANG Ying, and CAO Xueqiang. Doping concentration of eu3+ as a fluorescence probe for phase transformation of zirconia. *Journal of Rare Earths*, 33(7):717–725, 2015.

[245] Dmitry Yudovsky and Anthony J Durkin. Hybrid diffusion and two-flux approximation for multilayered tissue light propagation modeling. *Applied Optics*, 50(21):4237–4245, 2011.

[246] XC Zhang, BS Xu, HD Wang, and YX Wu. An analytical model for predicting thermal residual stresses in multilayer coating systems. *Thin Solid Films*, 488(1-2):274–282, 2005.

[247] Yanli Zhang, Daniel Emil Mack, Georg Mauer, and Robert Vaßen. Laser cladding of embedded sensors for thermal barrier coating applications. *Coatings*, 8(5):176, 2018.

[248] Shi-bin Zhao, Cun-lin Zhang, Nai-ming Wu, and Hua-ming Wang. Quality evaluation

for air plasma spray thermal barrier coatings with pulsed thermography. *Progress in Natural Science: Materials International*, 21(4):301–306, 2011.

[249] Chungen Zhou, Na Wang, and Huibin Xu. Comparison of thermal cycling behavior of plasma-sprayed nanostructured and traditional thermal barrier coatings. *Materials Science and Engineering: A*, 452:569–574, 2007.